Dirac Landau levels and magnetization on curved surfaces

Dissertation
zur Erlangung des Doktorgrades
der Naturwissenschaften (Dr. rer. nat.)
der Fakultät für Physik
der Universität Regensburg

vorgelegt von

Maximilian Fürst

aus

Grafling

Juni 2026

Promotionsgesuch eingereicht am: 27.05.2026

Die Arbeit wurde angeleitet von: Prof. Dr. Klaus Richter

Prüfungsausschuss:

Vorsitzender:	Prof. Dr. Jascha Repp
Erstgutachter:	Prof. Dr. Klaus Richter
Zweitgutachter:	dr hab. Magdalena Margańska-Łyżniak, prof. uczelni
Weiterer Prüfer:	Prof. Dr. Tilo Wettig

Promotionskolloquium fand statt am: 27.07.2026

Für meine Mutter.

Abstract

Novel classes of materials, like graphene and three-dimensional topological insulators host massless quasiparticles with Dirac-like dispersion which live in two dimensions. In this thesis, we deal with the consequences of confining them on a curved surface of revolution and applying a magnetic field, where we especially focus on the case of the experimentally most relevant case of a homogeneous magnetic field pointing in symmetry direction. We thoroughly study the symmetries of this system and find general properties of the Dirac Landau levels using supersymmetric quantum mechanics. As a first example, we consider the pseudosphere. We find asymptotic expressions for the Dirac Landau spectrum in the limit of strong magnetic fields, which decomposes into two different branches, one of them with a usual $B^{1/2}$ scaling of the Landau energies with magnetic field and one with an unconventional $B^{1/4}$ scaling. We further generalize this result by proofing a conjecture about this scaling law for a general class of surfaces, which includes prominent surfaces like the pseudosphere or the cone. We proof that for all surfaces in this class there are two distinctive branches of Landau levels. On the one hand, there is one where Landau energies always scale with the square root, independent of the particular geometry. On the other hand, there is a branch which is sensitive to the exact shape of the surface. The geometric parameter which characterizes the surface appears in the scaling exponent. We also examine the opposite limit, the weak field regime, and find the Zeeman effect, as well as a geometric correction term to the energy in case of non-flat surfaces. In the second part of the thesis, we numerically calculate the magnetic susceptibility for three surfaces in a homogeneous magnetic field in symmetry direction, each with constant Gaussian curvature, the pseudosphere, the cone and the (half) sphere. We find that even though all of them show distinctive signatures in the susceptibility, the overall appearance is very similar, with the important exception of the de Haas-van Alphen oscillations. We finally compute these oscillations analytically for the most interesting case of the pseudosphere.

List of used acronyms:

1D – one-dimensional
2D – two-dimensional
2DEG – two-dimensional electron gas
3D – three-dimensional
3DTI – three-dimensional topological insulators
CS – chiral symmetry
DCHE – Doubly-Confluent Heun Equation
dHvA – de Haas-van Alphen
DOS – density of states
IQHE – integer quantum Hall effect
IRAM – Implicitly Restarted Arnoldi Method
PHS – particle-hole symmetry
QHE – quantum Hall effect
ROC – region of convergence
SdH – Shubnikov-de Haas
SOC – Spin-orbit coupling
SUSY – supersymmetric quantum mechanics
SWKB – supersymmetric WKB
TRFIS – time-reversal field-inversion symmetry
TRS – time-reversal symmetry
UV – ultra violet
WKB – Wentzel-Kramers-Brillouin

Contents

1. Introduction

While most crystalline solids host quasiparticles which effectively behave as Schrödinger electrons with an effective mass, novel classes of materials like graphene [1, 2] or three-dimensional topological insulators (3DTIs) [3–6] can possess massless Dirac-like quasiparticles which show a dispersion relation where the energy is a linear function of momentum, which is in stark contrast to the aforementioned case, where this relation is quadratic in momentum. This has striking consequences, as phenomena which are normally only encountered in ultra-relativistic high-energy regimes can now be observed in a condensed matter system.

A very fundamental question in condensed matter physics is what happens, when an electron gas is subject to a homogeneous magnetic field pointing in a certain direction. This is the famous Landau problem which, for a two dimensional electron gas (2DEG), can be shown to be mathematically equivalent to the solution of the harmonic oscillator problem, yielding highly degenerate Landau levels which are equidistant in energy and scale linearly in the field strength B [7]. While this is true for conventional Schrödinger electrons, it turns out not to be the case for Dirac electrons, which rather show an energy which scales with the square root of the main quantum number n and magnetic field B [8–10]. Physical effects which can be related to the orbital Landau level structure, like the integer quantum Hall effect (IQHE), the Shubnikov-de Haas (SdH) effect, as well as the de Haas-van Alphen (dHvA) effect exist for Schrödinger and Dirac electrons but differ drastically due to the different Landau level structure [11–13].

When confining a particle to a certain submanifold of ambient space, it has consequences for its equations of motion, as well as for corresponding observables. This can for instance be seen in classical mechanics where a particle, subject to a gravitational field and moving along a brachistochrone curve behaves differently compared to one moving along a straight line, even though the starting and ending points coincide in space. We can transfer this idea to the Landau level problem and ask what happens when we confine the charge carriers to a curved surface, rather than a flat plane.

Considering this idea might seem to be straightforward in theory, but is very challenging when looking at it from an experimental perspective. While confining charged particles to certain regions in space is a long established procedure, it is a completely different story when this region is curved, especially at the quantum level. Here, these traditional methods are impractical. A possible way out of this is to tackle the issue from a different perspective. Instead of forcing a particle to move on a particular surface, we can use quasiparticles which are intrinsically located on this surface. Surface states of adequately shaped 3DTI nanowires seem to be like a paragon of virtue for this. As they behave like massless Dirac particles [3–6], we have to consider the effect of curved geometry on Dirac Landau levels. Recent experiments studying magnetotransport on shaped 3DTI nanowires [14, 15] further motivate this research field.

The history of quantum theory on curved spacetime dates back to as early as 1957. DeWitt was one of the first to point out possible difficulties when trying to formulate the Schrödinger equation in curved spaces and discovered the appearance of an additional term in the Hamiltonian, which is proportional to the scalar curvature [16]. This can be seen as the common starting point of two different research directions. On the one hand, it was tried to understand what happens, when quantum fields live in curved spacetime [17], which is effectively the birth of semiclassical gravity with the well-known predictions of Hawking [18] and Unruh [19] radiations. On the other hand, people examined what happens to quantum particles which are placed in flat spacetime but constrained to a certain submanifold, often a curved surface. A highlight of this development was the discovery of the *da Costa potential*, which exactly specified the additional term in the Hamiltonian, partly already found by deWitt, for a particle constrained to a curved surface [20]. It is important to highlight that he required the confinement to be due to a very narrow potential well, sandwiching the curved surface. The idea of this *thin-layer potential* goes back to Jensen and Koppe [21]. Until this point, it was assumed that the particle is not subject to an external field. In 2008, Ferrari and Cuoghi showed that the geometric potential is not only robust when electromagnetic fields are applied but also enters the Hamiltonian independently of it, producing no coupling terms between geometry and gauge field [22].

While this historic development prepared the ground for studying quantum mechanics on curved surfaces, it is not the appropriate formalism when describing Dirac particles, especially when they emerge from 3DTIs. First of all, Dirac particles have an equation of motion which substantially differs from the Schrödinger equation and second it is the very nature of the confinement which differs to the da Costa approach. Rather than being bound to the surface by a potential well, surface states in 3DTIs appear for topological reasons and decay into the bulk exponentially [4, 23]. The aforementioned *thin-layer potential* is therefore not an accurate description of the physical situation.

The system of a shaped 3DTI, exhibiting Dirac-like surface states on a curved surface, is exactly what was considered by Takane and Imura in 2013 [24]. Starting from an effective low-energy model of 3DTIs of the Bi_2Se_3 class [23, 25], they derived a continuum surface Hamiltonian without assuming specific local coordinates. The result is therefore very general and proves that these states are indeed described by a Dirac-like equation with the well-known *Spin-1/2 Berry phase* [24, 26, 27], *spin connection* [24, 27, 28], as well as a renormalization term stemming from the parabolic part of the band structure. While the first two mentioned modifications are crucial and qualitatively alter the outcomes, we neglect the renormalization term in this thesis. This can be justified as Spin-orbit coupling (SOC) is particularly strong in 3DTIs [23], making the renormalization term a secondary contribution. Additionally, we only consider the orbital coupling of the magnetic field and neglect the Zeeman coupling. This can be justified for a wide range of magnetic fields, as argued in [29].

While the matter is settled in this regard, the story is a bit different when it comes to analytically finding the eigenenergies of the Landau problem on curved surfaces. The mathematical research field of Spin geometry partially tackles this issue but mainly focuses on general theorems, rather than providing a concrete spectrum for a particular geometry. The exception from this is the case of surfaces with constant Gaussian curvature which are subject to a magnetic field which is overall perpendicular to the respective surface and constant in strength (throughout this thesis we just call this configuration an overall perpendicular magnetic field for convenience). For this case, a general spectral formula exists for Schrödinger and Dirac particles [30].

When it comes to the physicist community, most research efforts considering a particular surface also focus on this overall perpendicular field. Studies include the treatment of this problem on the sphere [31–34], the hyperbolic plane [35–42] and on the Poincare disc [36, 43] for Schrödinger electrons, as well as on the sphere [44–46], the hyperbolic plane [47, 48] and the hyperboloid [49, 50] for Dirac electrons.

Dirac Landau levels on the pseudosphere have been treated in [51] for a variety of electromagnetic field configurations, but excluding the cases of a purely overall perpendicular or a homogeneous magnetic field pointing in direction of the symmetry axis.

After publishing our results for the pseudosphere (see [27]), people studied general properties of Dirac Landau levels on this surface for a large class of magnetic field configurations [52].

The Landau problem on curved surfaces with an overall perpendicular magnetic field is easier to treat compared to a field configuration where the magnitude of the field component perpendicular to the surface varies in space. However, such perpendicular field configurations are almost impossible to realize in a real experiment. The easiest, experimentally feasible field configuration is of course an overall homogeneous magnetic field, pointing in a certain direction. While the magnetotransport problem for Dirac electrons, in particular realized as surface states of shaped 3DTI nanowires, has already been addressed in previous works [53–58], mainly numerically, the analytical solution of the Dirac Landau level problem for curved surfaces subject to a homogeneous magnetic field mainly remains an open problem. For this reason, the first part of this thesis focuses on the calculation of energies of these levels for certain geometries, trying to make one step ahead towards bridging the gap between theoretical models and experimentally feasible systems. In order to have a realistic chance to obtain analytical solutions, we will restrict to surfaces of revolution, which have azimuthal symmetry and are henceforth separable. While we develop our formalism without assuming a specific magnetic field configuration, we focus on the experimentally most relevant case of a homogeneous magnetic field pointing in direction of the symmetry axis of the surface of revolution, called a coaxial field in the following. A single exception to this is the surface being a pseudosphere for which we also consider an overall perpendicular magnetic field.

Although the Landau level spectrum is the key property which arises when placing electrons in a magnetic field, strictly speaking it is not directly observable in experiments but rather its imprints on certain observables of the system can be measured. One of the most prominent examples is to attach leads to the device under investigation and measure the magnetotransport properties. A second channel is offered by studying the magnetic susceptibility χ itself. While its properties for flat Dirac systems are well-examined [11, 59–73], especially in the context of graphene, the case of curved geometries is not covered adequately by current research, especially for the coaxial field configuration. For this reason, it becomes the second main scope of this thesis.

In Chapter 2, we will start our journey with revising essential foundations for the rest of the thesis. This includes a brief introduction in supersymmetric quantum mechanics (SUSY), the presentation of the Dirac Landau level problem on a flat plane, as well as basic techniques to numerically solve the Dirac equation. A necessary ingredient to a full understanding is differential geometry of (Semi-)Riemannian manifolds. Since this field is too large and too deep to be covered here in the necessary extent, we refer the reader to [28].

We will set the stage for the main part of the thesis in Chapter 3, where we formulate the Dirac equation on surfaces of revolution in presence of a magnetic field and systematically study its symmetries. We further present a version of the *Schrödinger-Lichnerovicz theorem* [74, 75] which links the Dirac operator and the Laplacian to each other. We adapt it to our specific problem and present an algebraic relation between the Schrödinger and Dirac Landau level spectra for the case of a surface of revolution with constant Gaussian curvature subject to an overall perpendicular field. This is a well-known result of Spin geometry [30].

Chapter 4 is devoted to analytically finding Landau levels for certain geometries. At the very beginning, we use the SUSY formalism to make a general statement about the form of the wavefunctions, in particular about the number of nodes of each spinor component, which holds for all surfaces of revolution and both field configurations, the overall perpendicular, as well as the coaxial one. As a first concrete example we calculate Dirac Landau levels for the pseudosphere, which is a surface with constant negative Gaussian curvature, in an overall perpendicular magnetic field. This problem has already been addressed in the author's Master thesis [76]. We extend the results from there by rederiving the spectrum with two alternative approaches, an analytical one and a purely algebraic one, which is based on SUSY. All results for the eigenenergies coincide and agree with the general formula given in [30]. We further provide closed expressions for the wavefunctions. After this, we continue with the treatment of the experimentally more relevant case of a coaxial magnetic field. We analytically find the approximate spectrum in the regime of strong magnetic fields which, to the best of our knowledge, is a novel result. Surprisingly, some levels show an energy scaling with $B^{1/4}$, clearly differing from the conventional $B^{1/2}$ scaling of flat Dirac systems. Finally, we confirm our results numerically and also take a look at the corresponding wavefunctions.

In the second part of this chapter, we consider a general class of surfaces described in [77] with a geometric form parameter $\gamma \in \mathbb{N}$ which determines how the radial profile changes as a function of arclength. Special cases of these surfaces are the pseudosphere ($\gamma = 1$) or the cone ($\gamma = 0$). A conjecture about the scaling of Dirac Landau level energies as a function of B, where the exponent is a function of γ, is also proposed in [77]. In this thesis, we generalize this class even more by allowing $\gamma \in \mathbb{R}$. This makes a continuous transformation between e.g. the pseudosphere and the cone possible. The highlight of this chapter is a proof of the aforementioned spectral scaling conjecture. As in the special case of the pseudosphere, we proof the existence of two distinctive branches of Landau levels, one where energies always scale with the square root of the magnetic field, independent of the particular geometry, and one which is sensitive to the exact shape of the surface, with the form parameter γ appearing in the scaling exponent. Whenever possible, we give exact analytical solutions. In case this is not possible, we resort to a semiclassical treatment of the problem. Here, the semiclassical WKB method (SWKB) [78] plays a vital role. We numerically confirm our findings and further examine the corresponding wavefunctions.

The scope of Chapter 5 is the magnetization for Dirac electrons subject to a coaxial magnetic field on three different surfaces of constant Gaussian curvature, namely the pseudosphere, the cone and the (half) sphere. Our goal is to calculate the susceptibility which turns out to be highly non-trivial in general. We therefore start with a fully numerical treatment of the problem. As our main interest is the influence of curved space on physical observables, we do not dwell too much on elaborating features which also appear in flat space but focus on those exclusive to the respective surface. The dHvA effect turns out to be highly distinctive for the three surfaces. We therefore complement our numerical findings with an analytical calculation of it for the pseudosphere where it shows the most unconventional signatures.

Additionally, we recover the Zeeman splitting in the regime of weak magnetic fields and interestingly also find a geometric energy correction term.

A practical method for computing the grand canonical potential using the bilateral Laplace transform is also introduced.

Finally, we summarize our key findings in Chapter 6, concluding this thesis and giving an outlook to what may be examined further in the future.

2. Basic methods

This introductory chapter is meant to summarize basic methods used in this thesis, with the only exception of differential geometry, which is too much matter to be covered here in all the necessary depth. We refer to [28] for an introduction to this field taylored to our needs.

In the first part of this chapter, we give a short overview over SUSY in quantum mechanics [78]. Then, we revise the Dirac Landau level problem on a flat plane in polar coordinates. We find the well-known *Spin-1/2 Berry phase* [24, 26, 27] as well as the *spin connection term* [24, 27, 28] even in flat space. This helps us to understand its meaning at a later stage of the work. We conclude this chapter with the issue of numerically solving the Dirac equation on a lattice and present the method used in this thesis.

2.1. Supersymmetry in quantum mechanics

The idea of supersymmetry was first formulated in the context of relativistic quantum field theories [79, 80]. The version we will use in this thesis is derived from this but was transferred to the habitat of quantum mechanics, mainly by Witten [81, 82].

Our brief introduction mainly follows [78]. In the following, we present SUSY for the case of non-relativistic quantum mechanics, i.e. for a Schrödinger Hamiltonian with the respective prefactors. Obviously, the framework can also be used for a Schrödinger-like equation, with the prefactors being adjusted accordingly.

Suppose the Hamiltonian

$$\hat{H}_1 = -\frac{\hbar^2}{2m}\frac{d^2}{dx^2} + V_1(x)\,, \tag{2.1}$$

to be given with potential $V_1(x)$. Let us assume, that we can find a decomposition, such that $\hat{H}_1 = \hat{A}^\dagger \hat{A}$, with $\hat{A} = \frac{\hbar}{\sqrt{2m}}\frac{d}{dx} + W(x)$ and its adjoint $\hat{A}^\dagger = -\frac{\hbar}{\sqrt{2m}}\frac{d}{dx} + W(x)$. We call $W(x)$ the *superpotential* of $\hat{H}_1$. Comparing the two expressions for the Hamiltonian yields the identification [78]

$$V_1(x) = W^2(x) - \frac{\hbar}{\sqrt{2m}}\frac{dW(x)}{dx}\,. \tag{2.2}$$

Let us now define $\hat{H}_2 = \hat{A}\hat{A}^\dagger$, where the potential is obviously given by [78]

$$V_2(x) = W^2(x) + \frac{\hbar}{\sqrt{2m}}\frac{dW(x)}{dx}\,. \tag{2.3}$$

We call $\hat{H}_1$ and $\hat{H}_2$ *supersymmetric partner Hamiltonians*, as well as $V_1(x)$ and $V_2(x)$ *supersymmetric partner potentials*. As both Hamiltonians are intimately linked to each other, strong relations between them hold. We list the most important of them [78]:

- Without loss of generality, we assume the lowest energy eigenstate of both Hamiltonians to have zero energy.
- Let $\psi(x)$ be an eigenstate of $\hat{H}_1$ with energy E. Then $\hat{A}\psi(x)$ is an eigenstate of $\hat{H}_2$ with the same energy.
- Vice versa, let $\psi(x)$ be an eigenstate of $\hat{H}_2$ with energy E. Then $\hat{A}^\dagger\psi(x)$ is an eigenstate of $\hat{H}_1$ with the same energy.
- Every energy eigenstate of one Hamiltonian has a partner eigenstate in the Hilbert space of the other Hamiltonian with the same energy, except perhaps for the ground state of one Hamiltonian.
- If both Hamiltonians have the same ground state, we say that SUSY is *broken*.
- If one Hamiltonian has a ground state which is not an eigenstate of the other Hamiltonian, we say that SUSY is *unbroken*. The ground state of this one Hamiltonian does not have a partner state.
- The eigenvalue problem of both Hamiltonians is of Sturm-Liouville type. The ground state solution of each Hamiltonian is therefore nodeless. The n-th eigenstate has $(n-1)$ nodes [83].
- Consequently, if SUSY is broken, the respective partner eigenstates of the two Hamiltonians belonging to the same energy have the same number of nodes.
- If SUSY is unbroken, the respective partner eigenstates of the two Hamiltonians belonging to the same energy differ in number of nodes by one. The state belonging to the Hamiltonian with the partnerless ground state has one node more than the state belonging to the other Hamiltonian.

While these properties always hold, even the whole energy spectrum of the Hamiltonians can be gained, if the SUSY partner potentials are shape invariant and SUSY is unbroken. This is the case if they fulfill [78]

$$V_2(a_1, x) = V_1(a_2, x) + R(a_1)\,, \tag{2.4}$$

where a_1 denotes a family of parameters and $a_2 = f(a_1)$ and $R(a_1)$ are functions of a_1. It can be shown, that the n-th eigenstate (starting from $n = 0$) of the Hamiltonian with the partnerless ground state is given by [78]

$$E_n(a_1) = \sum_{k=1}^{n} R(a_k)\,, \tag{2.5}$$

if $n > 0$ and $E_0(a_1) = 0$. As shape invariance is a very strong property, we often have to use different methods for obtaining the spectrum. If solving the Schrödinger equation analytically is not possible, we can resort to semiclassical methods, in particular the WKB approximation. It turns out that a specific version of it exists for SUSY systems, called *supersymmetric WKB (SWKB)*. The action we have to quantize is given by [78]

$$S(E) = 2 \int_{x_-}^{x_+} dx \sqrt{E - W^2(x)}\,, \tag{2.6}$$

where x_- and x_+ are the classical turning points when $E = W^2(x)$ and $x_- < x_+$. The quantization condition now depends on whether SUSY is unbroken or broken. In the first case, it reads $S(E_n) = 2\pi n\hbar$, where n starts from zero for the Hamiltonian with the partnerless ground state and from one for the other Hamiltonian [78]. When SUSY is broken, the condition is given by $S(E_n) = 2\pi\hbar(n + 1/2)$ for both Hamiltonians, starting from $n = 0$ [78].

2.2. Dirac Landau levels on a flat plane

We want to take a look at the Dirac Landau level problem on a flat plane in order to be prepared for the more complicated case on curved surfaces. Contrary to the most direct way of formulating the problem in Landau gauge, we use a symmetric gauge and polar coordinates. This makes the problem much more complicated but has the advantage that we can use the almost same coordinates for curved surfaces. As the issue of finding Dirac Landau level energies has exhaustively been treated in literature [8–10], it is not our goal to give a full, detailed solution of the problem, but to discuss peculiarities which appear when formulating the Dirac equation in curved coordinates (like polar ones), as well as to present the Dirac Landau level spectrum for the flat plane.

The Dirac Hamiltonian reads

$$\hat{H} = \hbar v_F \left(-i\partial_x\sigma_x - i\partial_y\sigma_y\right)\,, \tag{2.7}$$

where σ_x and σ_y are Pauli matrices and v_F is a model parameter which is conveniently called Fermi velocity. For emergent Dirac quasiparticles in condensed matter systems, it is usually fitted with first principle band structure models.

We want to work in the symmetric gauge, where the vector potential reads $\vec{A} = B/2\,(-y\vec{e}_x + x\vec{e}_y)$, with the two cartesian unit vectors $\vec{e}_x$ and $\vec{e}_y$. Using the minimal coupling rule, we arrive at (for convenience, we recycle the symbol $\hat{H}$ which we have already used for the uncoupled Hamiltonian)

$$\hat{H} = \hbar v_F \left[-i\left(\partial_x - i\frac{eB}{\hbar}\frac{y}{2}\right)\sigma_x - i\left(\partial_y + i\frac{eB}{\hbar}\frac{x}{2}\right)\sigma_y\right]\,, \tag{2.8}$$

with elementary charge e. We assumed a charge of $-e$ here since we are dealing with electrons. This convention is used throughout the thesis. We switch to polar coordinates

(r, ϕ), yielding

$$\begin{aligned} \hat{H} &= +\hbar v_F \left(-i\cos(\phi)\partial_r + i\frac{1}{r}\sin(\phi)\partial_\phi - \frac{eB}{2\hbar} r\sin(\phi) \right) \sigma_x \\ &\quad +\hbar v_F \left(-i\sin(\phi)\partial_r - i\frac{1}{r}\cos(\phi)\partial_\phi + \frac{eB}{2\hbar} r\cos(\phi) \right) \sigma_y \\ &= +\hbar v_F \begin{pmatrix} 0 & \exp(-i\phi) \\ \exp(i\phi) & 0 \end{pmatrix} (-i\partial_r) \\ &\quad +\hbar v_F \begin{pmatrix} 0 & -i\exp(-i\phi) \\ i\exp(i\phi) & 0 \end{pmatrix} \left(-i\frac{1}{r}\partial_\phi + \frac{eB}{2\hbar} r \right) . \end{aligned} \tag{2.9}$$

This form is uncomfortable, as the entries of the matrices are functions of ϕ. We can remove this by changing the spinor basis with the unitary transformation

$$\hat{U} = \begin{pmatrix} \exp\left(\frac{i}{2}\phi\right) & 0 \\ 0 & \exp\left(-\frac{i}{2}\phi\right) \end{pmatrix} . \tag{2.10}$$

The spinor wavefunction ψ now transforms as $\tilde{\psi} = \hat{U}\psi$, whereas the Hamiltonian transforms as

$$\begin{aligned} \hat{\tilde{H}} &= \hat{U}\hat{H}\hat{U}^\dagger \\ &= \hbar v_F \left[-i\left(\partial_r + \frac{1}{2r}\right)\sigma_x + \left(-i\frac{1}{r}\partial_\phi + \frac{eB}{2\hbar} r \right)\sigma_y \right] . \end{aligned} \tag{2.11}$$

We can see, that this transformation completely eliminates the rotating matrices, leaving only conventional Pauli matrices. Note, that since the derivative with respect to ϕ also acts on $\hat{U}$, we obtained an additional term. This is the famous *spin connection* [24, 27, 28], which naturally arises here without any further assumptions from bare calculation. Another interesting consequence may be observed when looking at boundary conditions. ψ has to be single-valued, which means that $\psi(r, 0) = \psi(r, 2\pi)$, or in other words, it has to fulfill periodic boundary conditions in ϕ. Obviously, $\tilde{\psi}(r, 0) = \psi(r, 0)$ but $\tilde{\psi}(r, 2\pi) = -\psi(r, 2\pi)$, implying that $\tilde{\psi}$ has to fulfill antiperiodic boundary conditions $\tilde{\psi}(r, 0) = -\tilde{\psi}(r, 2\pi)$. This effect can be seen as the consequence of the *Spin-1/2 Berry phase* [24, 26, 27].

In principle, we can find the spectrum of this Hamiltonian. However, we will develop a formalism at a later stage of the work, which can be used for the calculation of Dirac Landau levels in a coaxial magnetic field for arbitrary surfaces of revolution. Therefore, to avoid redundancy, we take a shortcut and only state the results here. The eigenenergies read [8–10]

$$E_n = \mathrm{sgn}(n) v_F \sqrt{2|n|\hbar e B} \, , \tag{2.12}$$

where $n \in \mathbb{Z}$ is the main quantum number. We see, that the eigenenergies scale with the square root of the modulus of the main quantum number n, as well as the square root of the magnetic field B. In the symmetric gauge, the wavefunctions can be expressed in terms of *Laguerre polynomials* [8, 10]. Since the eigenfunctions can be built using their Schrödinger counterparts [10], the degeneracy of all levels is equal to the number of flux quanta, as in case of the non-relativistic Landau levels [84].

2.3. Numerical solution of the Dirac equation

Many problems in this topic are not exactly solvable in a fully analytical fashion. For this reason, but also to validate analytical findings, we have to use numerical techniques to solve the Dirac equation. Let us assume to have an ordinary differential equation with variable x. A very common method to numerically solve it is to discretize x, or in other words to sample the space equidistantly. This gives us a collection of points $x_n = n\Delta x, n \in \mathbb{Z}$. Functions of x are then represented by their values at these discrete points. A derivative with respect to x can be approximated using the symmetric difference

$$\left.\frac{df(x)}{dx}\right|_{x_n} \approx \frac{f(x_{n+1}) - f(x_{n-1})}{2\Delta x}\,. \tag{2.13}$$

This scheme can be generalized to derivatives of higher order. The problem of solving the differential equation has now effectively been converted into the problem of finding the kernel of a (sparse) matrix. While this procedure works very well for the Schrödinger equation, it turns out to cause great issues when trying to solve the massless Dirac equation with it. Assuming to have a vanishing potential, spurious solutions arise, a phenomenon which is commonly known as *Fermion doubling* [85]. As long as the Dirac equation is free, physical solutions can often be distinguished from their spurious doublers. However, as soon as a potential takes effect, the solutions couple, giving results which are not physically interpretable anymore [55].

We can see the issue by solving this simple model explicitly. Let us assume the Dirac equation in one dimension, given by

$$\hat{H} = -i\hbar v_F \partial_x \sigma_x\,. \tag{2.14}$$

Applying the symmetric discretization scheme converts this into a tight-binding Hamiltonian

$$\hat{H}_{TB} = -i\frac{\hbar v_F}{2\Delta x}\sum_n \sum_{s,s'} \left(\hat{\psi}^\dagger_{ns'}\sigma_x\hat{\psi}_{(n+1)s} - \hat{\psi}^\dagger_{(n+1)s'}\sigma_x\hat{\psi}_{ns}\right)\,, \tag{2.15}$$

where we introduced fermionic operators, $\hat{\psi}^\dagger_{ns}$ and $\hat{\psi}_{ns}$ in the discretized spatial basis, creating and annihilating a particle with spin $s \in \{\uparrow,\downarrow\}$ in the usual basis at lattice point n. Applying $\hat{H}_{TB}$ onto the Bloch basis $\hat{\psi}^\dagger_{ks} = \sqrt{\frac{\Delta x}{2\pi}}\sum_n \exp(ikn\Delta x)\hat{\psi}^\dagger_{ns}$ yields

$$\begin{aligned}
\hat{H}_{TB} &= -i\frac{\hbar v_F}{2\Delta x}\int_{-\frac{\pi}{\Delta x}}^{\frac{\pi}{\Delta x}} dk\,\left[\exp(ik\Delta x) - \exp(-ik\Delta x)\right]\sum_{s,s'}\hat{\psi}^\dagger_{ks'}\sigma_x\hat{\psi}_{ks} \\
&= \frac{\hbar v_F}{\Delta x}\int_{-\frac{\pi}{\Delta x}}^{\frac{\pi}{\Delta x}} dk\,\sin(k\Delta x)\sum_{s,s'}\hat{\psi}^\dagger_{ks'}\sigma_x\hat{\psi}_{ks}\,.
\end{aligned} \tag{2.16}$$

The remaining, non-diagonal spin part, σ_x, is easily seen to have eigenvalues of ± 1. This leads to a symmetric spectrum with respect to zero energy. We can conclude, that the dispersion for a fixed k reads

$$E_{TB} = \pm\frac{\hbar v_F}{\Delta x}\sin(k\Delta x)\,. \tag{2.17}$$

For a small k, this can be approximated by $E_{TB} = \pm\hbar v_F k$, which perfectly agrees with the continuum model. However, upon rising momentum, the dispersion deviates more and more from the expected behavior and ultimately even creates a second, spurious Dirac cone at the boundaries of the first Brillouin zone of our numerical lattice (at $k = \pm\pi/\Delta x$). The main issue with this is not, that the approximation becomes inaccurate for high k, but that it produces spurious solutions which have the same energy as the well-approximated states close to $k = 0$, making them virtually indistinguishable.

The problem of *Fermion doubling* has been an issue, especially in particle physics, since the introduction of lattice gauge theories [86, 87]. The deeper reasons for this case, where (3+1) dimensions are considered, are elucidated by the *Nielsen-Ninomiya theorem* [88]. It states that the issue is unavoidable unless one of its requirements, like locality or chiral symmetry of the discretized Hamiltonian, is sacrificed [85].

Similar principles also hold in different dimensions [85]. Since we wish to preserve all fundamental symmetries in this thesis and we do not deal with translationally invariant systems (like leads in case of transport), it is most convenient to give up locality. The price we have to pay is that a non-local, discretized Hamiltonian might lead to higher computational costs. A suitable realization is to replace the symmetric difference approximation of the derivative by the *tangent fermion discretization scheme*, which goes back to Stacey [85, 89]:

$$\left.\frac{df(x)}{dx}\right|_{x_n} \approx \frac{2}{\Delta x}\sum_{m=1}^{\infty}(-1)^m \left[f(x_{n-m}) - f(x_{n+m})\right] . \tag{2.18}$$

In a real numerical calculation, we would have a finite number of lattice points, so the sum in this formula going to infinity becomes problematic in general. However, in our particular case, it turns out to be not a big issue. We only use numerical methods to solve the Dirac equation in presence of a steep potential well, so that the wavefunction decays quickly outside a certain, finite region. It is a good approximation to assume that it totally vanishes there. We consequently have infinitely many zero terms, effectively truncating the sum.

Throughout this thesis, we use the *tangent fermion discretization scheme* to convert the continuous Dirac equation into a discrete matrix representation and find its eigenvalues with the library *ARPACK*, which uses the *Implicitly Restarted Arnoldi Method (IRAM)*. The code for this procedure was written by the author of this thesis in C++.

3. Quantum mechanics on curved surfaces

This chapter introduces the formalism to describe quantum mechanics on curved surfaces of revolution. Notation and differential geometric definitions are adapted from [28]. We start with a basic description of them as Riemannian manifolds and talk about the problems, which might arise when trying to incorporate a magnetic field in three spatial dimensions into a purely two-dimensional (2D) Dirac or Schrödinger equation. We present the general forms of Dirac and Schrödinger Hamiltonians for a particle confined on a surface of revolution and subject to a magnetic field. We use the well-known *Schrödinger-Lichnerowicz theorem* to verify that for surfaces with constant Gaussian curvature and in an overall perpendicular magnetic field, the spectra of Dirac and Schrödinger electrons are related by a simple algebraic equation. We conclude with a thorough study of discrete and continuous symmetries of the Dirac Hamiltonian on surfaces of revolution.

3.1. Basic differential geometric quantities

In the following, we consider a surface of revolution Σ, embedded in flat Minkowski space. Since time does not couple to any spatial components in our case, it is enough to restrict our differential geometric analysis to a two-dimensional, purely spatial submanifold. Σ can then be characterized by its radial profile $r(z)$. We parametrize it by the azimuthal angle ϕ around the symmetry axis, as well as a radial coordinate. We choose the arclength l which is the length traveled from a starting point when walking along the surface at a fixed azimuthal angle. It can be related to the radius by

$$l(r) = l_0 + \int_{r_0}^{r} d\tilde{r}\,\sqrt{1+\left(\frac{dz(\tilde{r})}{d\tilde{r}}\right)^2}\,, \tag{3.1}$$

where r_0 and l_0 are radius and arclength of the starting point. r, z and l can mutually be expressed by each other, when bijectivity of $r(z)$ and $l(r)$ is assumed. The parametrization of Σ reads

$$\Sigma : [0,L]\times[0,2\pi] \to \mathbb{R}^3, (l,\phi) \mapsto \begin{pmatrix} r(l)\cos\phi \\ r(l)\sin\phi \\ z(l) \end{pmatrix}\,, \tag{3.2}$$

where L is the overall arclength. From this, it is easy to write down the tangent vectors in ambient three-dimensional (3D) space,

$$\vec{\partial}_l^{3D} = \frac{\partial\Sigma}{\partial l} = \begin{pmatrix} r'(l)\cos\phi \\ r'(l)\sin\phi \\ z'(l) \end{pmatrix}\,, \quad \vec{\partial}_\phi^{3D} = \frac{\partial\Sigma}{\partial\phi} = \begin{pmatrix} -r(l)\sin\phi \\ r(l)\cos\phi \\ 0 \end{pmatrix}\,, \tag{3.3}$$

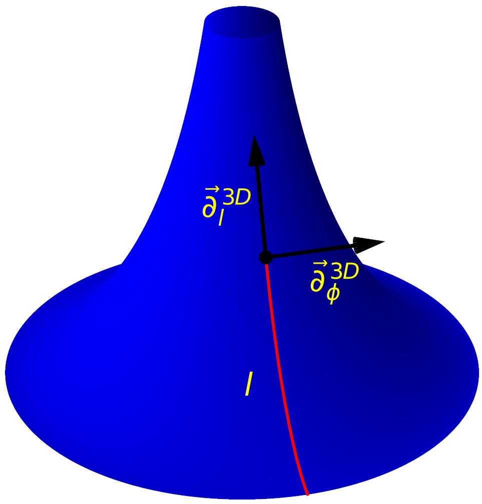

Figure 3.1: Illustration of an exemplary surface of revolution with the tangent vectors $\vec{\partial}_l^{3D}$ and $\vec{\partial}_\phi^{3D}$ at a random point as well as the arclength l.

where $'$ denotes the derivative with respect to l. We use the superscript "3D" here in order to distinguish these quantities from the tangent vectors $\vec{\partial}_l$ and $\vec{\partial}_\phi$ of the manifold itself. The latter have dual 1-forms denoted by dx^l and dx^ϕ. Fig. 3.1 illustrates our choice of radial coordinate as well as the tangent vectors.

The induced metric tensor can easily be obtained by calculating the ambient scalar product of these vectors, yielding

$$\boldsymbol{g} = dx^l \otimes dx^l + r^2(l)\, dx^\phi \otimes dx^\phi = g_{\mu\nu}\, dx^\mu \otimes dx^\nu \,. \tag{3.4}$$

where we used Einstein's sum convention over greek indices. The order $\left\{\vec{\partial}_l, \vec{\partial}_\phi\right\}$ is defined to have positive orientation and the indices 1 and 2. This complies with the definition of the spatial volume form,

$$\boldsymbol{\omega} = \sqrt{|\det \boldsymbol{g}|}\, dx^l \wedge dx^\phi = r(l)\, dx^l \wedge dx^\phi \,. \tag{3.5}$$

In addition to this, it is necessary to introduce an orthonormal frame. We denote the tangent vectors of this as $\{\vec{e}_1, \vec{e}_2\}$, their corresponding covectors as $\left\{de^1, de^2\right\}$ and use latin indices when summing in order to distinguish them from the local coordinate quantities. The defining property of this frame is, that it brings the metric tensor into Sylvester normal form

$$\boldsymbol{\eta} = de^1 \otimes de^1 + de^2 \otimes de^2 = \eta_{ab}\, de^a \otimes de^b \,. \tag{3.6}$$

The vielbein field is then defined such that it relates the components of the two tensors as

$$g_{\mu\nu} = e^a_\mu e^b_\nu\, \eta_{ab} \,. \tag{3.7}$$

However, note that the vielbein field is not a tensor because both indices transform differently. The non-zero elements are easily found to be $e_l^1 = 1$ and $e_\phi^2 = r(l)$.

Another quantity which is necessary to calculate the Schrödinger Hamiltonian is the Hodge star operator $*$. It acts on a basis of the algebra of differential forms $\Omega(\Sigma)$ as

$$*1 = \boldsymbol{\omega},\ *dx^l = r(l)\, dx^\phi,\ *dx^\phi = -\frac{1}{r(l)} dx^l,\ *\boldsymbol{\omega} = 1\,. \tag{3.8}$$

When dealing with conserved currents, it is useful to know how the divergence operator looks in our curvilinear coordinates. Assuming a vector field $\vec{X}$ on Σ, it is defined by [28]

$$\begin{aligned}
\mathrm{div}\vec{X} &= *d*\left(X^\flat\right) \\
&= *d*\left(X^1\vec{e}_1 + X^2\vec{e}_2\right)^\flat \\
&= *d*\left(X^1 de^1 + X^2 de^2\right) \\
&= *d*\left(X^1 dx^l + r(l) X^2 dx^\phi\right) \\
&= *d\left(r(l) X^1 dx^\phi - X^2 dx^l\right) \\
&= *\left(\left(\partial_l\left(r(l)X^1\right)\right) dx^l \wedge dx^\phi - \left(\partial_\phi X^2\right) dx^\phi \wedge dx^l\right) \\
&= \frac{1}{r(l)}\partial_l\left(r(l)X^1\right) + \frac{1}{r(l)}\partial_\phi X^2\,.
\end{aligned} \tag{3.9}$$

Since we work with Spin-1/2 particles in two dimensions, we need a representation ρ of the Clifford algebra $C(2,0)$, with basis $\gamma^a = \rho(de^a)$ fulfilling

$$\left\{\gamma^a, \gamma^b\right\} = 2\eta^{ab}\mathbb{1}\,. \tag{3.10}$$

We choose the Pauli matrices $\gamma^1 = \sigma_x$ and $\gamma^2 = \sigma_y$.

3.2. Magnetic field and covariant derivative

We also want to include a magnetic field into our model. However, in two dimensions, electromagnetism is different compared to full Minkowski space. When restricting to purely magnetic fields (in the inertial lab frame), it turns out that only one direction is possible, the one perpendicular to the surface. The mathematical reason for this is, that only one linearly independent 2-form is available in two dimensions, namely the volume form $\boldsymbol{\omega}$, which corresponds to one magnetic field direction [28].

A more physically intuitive explanation can be given by considering a classical charged particle confined on a 2D manifold. When applying a tangential magnetic field, the Lorentz force directs in the normal direction and therefore has no effect because it cannot move in this way.

In full analogy to conventional Minkowski space, the field strength 2-form of a magnetic field, which is parallel to the outer surface normal, is given by $\boldsymbol{F} = -B_\perp(l)\,\boldsymbol{\omega}$ [28] (the minus sign appears because our volume form is oriented inwards, whereas we demand the magnetic field to point outwards for $B_\perp(l) > 0$). Choosing a symmetric gauge, the potential 1-form is given by [28]

$$-B_\perp(l)\, r(l)\, dx^l \wedge dx^\phi = -B_\perp(l)\, \boldsymbol{\omega} = \boldsymbol{F} \stackrel{!}{=} d\boldsymbol{A} = d(A_\phi\, dx^\phi) = \frac{\partial A_\phi(l)}{\partial l} dx^l \wedge dx^\phi \,. \quad (3.11)$$

Comparing coefficients, this directly yields

$$A_\phi(l) = -\int dl\, B_\perp(l)\, r(l)\,, \quad (3.12)$$

where we can choose the integration constant arbitrarily. It is more elucidating to represent this in the (orthonormal) frame field

$$A(l) := A_2(l) = e_2^\mu A_\mu = -\frac{1}{r(l)} \int dl\, B_\perp(l)\, r(l)\,, \quad (3.13)$$

where the units of $A(l)$ are equal to those commonly used in flat Minkowski space.

We want to take a closer look at two special cases which will be important throughout the rest of this thesis. The first one is a constant, overall perpendicular field $B_\perp = B \neq f(l)$. In this case, the equation simplifies to

$$A(l) = -\frac{B}{r(l)} \int dl\, r(l)\,, \quad (3.14)$$

where the integral only depends on the geometry itself. The second case is a field $B_\perp(l)$, such that it equals the projection of a homogeneous magnetic field in symmetry direction $\vec{B} = \begin{pmatrix} 0 & 0 & B \end{pmatrix}^T$ onto the outer surface normal at each point. Fig. 3.2 illustrates the two magnetic field configurations.

To evaluate the case of a coaxial field further, we need to calculate the projection explicitly,

$$B_\perp(l) = B \left(-\frac{\vec{\partial_l}^{\,3D} \times \vec{\partial_\phi}^{\,3D}}{\left\| \vec{\partial_l}^{\,3D} \times \vec{\partial_\phi}^{\,3D} \right\|} \right)_z = -B\, r'(l)\,. \quad (3.15)$$

This gives the vector potential

$$A(l) = \frac{B}{r(l)} \int dl\, r'(l)\, r(l) = \frac{B}{r(l)} \int dr\, r = \frac{B}{2} r(l) = \frac{\Phi(l)}{2\pi r(l)}\,, \quad (3.16)$$

where we set the integration constant to zero and introduced the flux through the cross section (orthogonal to the symmetry axis) $\Phi(l) = \pi B r^2(l)$. We gained this result from our purely 2D theory. The question is now whether this captures the physics of a fully 3D magnetic field, as it appears in reality. Since the flux through the cross section is given by the product of the vector potential in azimuthal direction and its circumference, as one would expect for the symmetric gauge in three dimensions, we can give a positive answer to this. This is remarkable because $A(l)$ has only been derived from the orthogonal

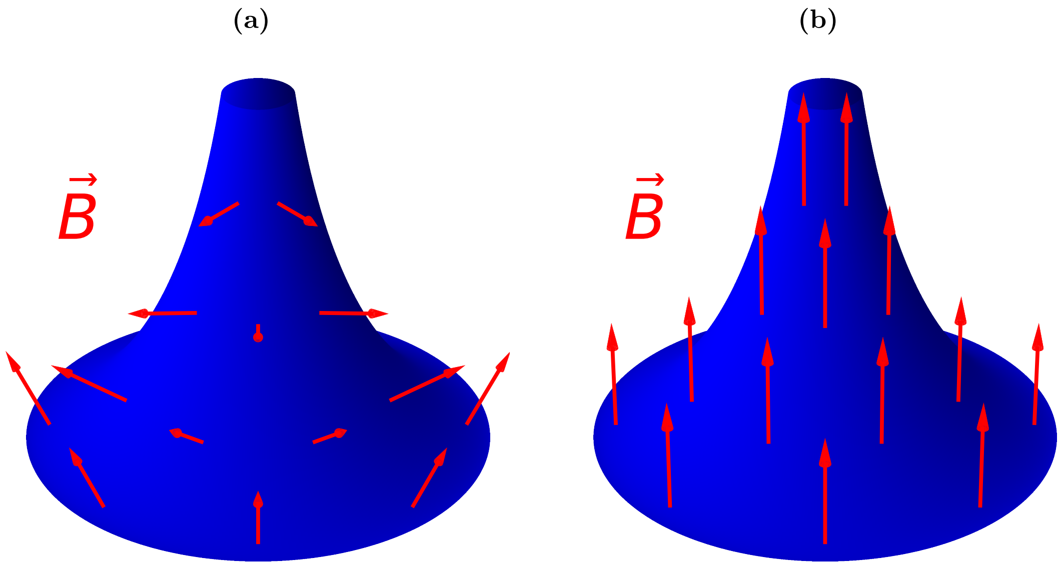

Figure 3.2: Illustration of an exemplary surface of revolution with the two magnetic field configurations treated in this thesis, an overall perpendicular magnetic field ((a)) and a coaxial magnetic field ((b)).

projection of the magnetic field $\vec{B}$ onto the submanifold normal. Note, that it was crucial to set the integration constant to zero. A non-zero constant would add an additional magnetic flux if interpreted as a 3D vector potential.

The gauge field can be coupled to the particle through minimal coupling of the derivative. However, there is a second non-trivial contribution to this since we work with Spin-1/2 fields which transform differently compared to scalar (Spin-0) fields when transported on the surface. The spin connection $\boldsymbol{\omega_{ab}}$ [24, 27, 28] (calculated explicitly in Appendix A.1) takes care of this and together with the gauge field $\boldsymbol{A}$ gives the *exterior covariant derivative* of a spinor field ψ [28],

$$\begin{aligned} D\psi &= d\psi + \frac{1}{8}\boldsymbol{\omega_{ab}}[\gamma^a,\gamma^b] + i\frac{e}{\hbar}\boldsymbol{A} \\ &= (\partial_l\psi)\,dx^l + (\partial_\phi\psi)\,dx^\phi - \frac{i}{2}r'(l)\sigma_z\psi\,dx^\phi + i\frac{e}{\hbar}r(l)A(l)\psi\,dx^\phi \\ &= (\partial_l\psi)\,de^1 + \frac{1}{r(l)}(\partial_\phi\psi)\,de^2 - \frac{i}{2}\frac{r'(l)}{r(l)}\sigma_z\psi\,de^2 + i\frac{e}{\hbar}A(l)\psi\,de^2\,. \end{aligned} \tag{3.17}$$

Remember, that we obtained the spin connection term in Chapter 2 from scratch. The term here has the same origin but was calculated from the general theory of Spin geometry.

To conclude this section, we note that the bare magnetic field B is not the only parameter that can be used to describe the magnetic field strength. We can also express the vector potential as a function of the magnetic length $l_B = \sqrt{\frac{\hbar}{e|B|}}$ or in case of the coaxial field as the ratio of the flux through the cross section at $r(0) := a$, $\Phi := \Phi(0)$, and the magnetic flux quantum $\Phi_0 = h/e$. The magnetic term in the covariant derivative is then given by

$$\frac{e}{\hbar}A(l) = \frac{eB}{2\hbar}r(l) = \frac{\pi eB}{h}r(l) = \operatorname{sgn}(B)\frac{r(l)}{2l_B^2} = \frac{r(l)}{a^2}\frac{\Phi}{\Phi_0} = \frac{r(l)}{a^2}\nu\,, \tag{3.18}$$

where we defined the number of flux quanta $\nu := \Phi/\Phi_0$. Our choice depends on what is most convenient in the respective situation.

3.3. The Dirac Hamiltonian

With all the preparatory work already done, it is easy to write down the final Dirac operator [28],

$$\begin{aligned} D\!\!\!/\psi &= \gamma^a i_{e_a} D\psi \\ &= \sigma_x\partial_l\psi + \sigma_y\frac{1}{r(l)}\partial_\phi\psi - \sigma_y\frac{i}{2}\frac{r'(l)}{r(l)}\sigma_z\psi + \sigma_y i\frac{e}{\hbar}A(l)\psi \\ &= \sigma_x\left(\partial_l + \frac{r'(l)}{2r(l)}\right)\psi + \sigma_y\left(\frac{1}{r(l)}\partial_\phi + i\frac{e}{\hbar}A(l)\right)\psi\,, \end{aligned} \tag{3.19}$$

where we used the exterior covariant derivative D from the previous section, as well as the orthonormal frame field e_a and our choices of gamma matrices γ^a from the very beginning of this chapter. We can define the hermitian Dirac Hamiltonian as

$$\hat{H}_D = -i\hbar v_F D\!\!\!/ = \hbar v_F\left[\sigma_x\left(-i\partial_l - i\frac{r'(l)}{2r(l)}\right) + \sigma_y\left(-i\frac{1}{r(l)}\partial_\phi + \frac{e}{\hbar}A(l)\right)\right]. \tag{3.20}$$

The time-independent Dirac equation then reads

$$\hat{H}_D\psi = E\psi\,, \tag{3.21}$$

with energy E. It turns out that in many cases the eigenenergies of the system have the prefactor $\hbar v_F/a$, where $a = r(0)$. It is therefore convenient to introduce the dimensionless energy $\epsilon := Ea/(\hbar v_F)$, which we will use frequently throughout this thesis.

3.4. The Schrödinger Hamiltonian

We also want to find the Schrödinger Hamiltonian. Using the codifferential $\delta = -*D*$, the Laplacian acting on a spinor ψ reads [28]

$$\Delta\psi = (D-\delta)^2\psi = (D^2 + \delta^2 - \delta D - D\delta)\psi = -\delta D\psi\,, \tag{3.22}$$

where we used that $D^2 = \delta^2 = 0$ and the fact that the codifferential annihilates ψ as a 0-form. Note, that sometimes the Laplacian is defined to be negative definite, whereas we defined it in a way so that it is positive definite. The concrete calculation is straightforward, albeit lengthy,

$$
\begin{aligned}
\Delta\psi &= *D*D\psi \\
&= *D*\left[(\partial_l\psi)\,dx^l + (\partial_\phi\psi)\,dx^\phi\right] \\
&\quad *D*\left[-\frac{i}{2}r'(l)\sigma_z\psi\,dx^\phi + i\frac{e}{\hbar}r(l)A(l)\psi\,dx^\phi\right] \\
&= *D\left[r(l)(\partial_l\psi)\,dx^\phi - \frac{1}{r(l)}(\partial_\phi\psi)\,dx^l\right] \\
&\quad *D\left[\frac{i}{2}\frac{r'(l)}{r(l)}\sigma_z\psi\,dx^l - i\frac{e}{\hbar}A(l)\psi\,dx^l\right] \\
&= *\left[(\partial_l^2\psi) + \frac{r'(l)}{r(l)}(\partial_l\psi) + \frac{1}{r^2(l)}(\partial_\phi^2\psi) - i\frac{r'(l)}{r^2(l)}\sigma_z(\partial_\phi\psi)\right]\boldsymbol{\omega} \\
&\quad *\left[2i\frac{e}{\hbar}\frac{1}{r(l)}A(l)(\partial_\phi\psi) - \frac{1}{4}\frac{r'^2(l)}{r^2(l)}\psi + \frac{e}{\hbar}\frac{r'(l)}{r(l)}A(l)\sigma_z\psi\right]\boldsymbol{\omega} \\
&\quad *\left[-\frac{e^2}{\hbar^2}A^2(l)\psi\right]\boldsymbol{\omega} \\
&= +\left[\partial_l^2 + \frac{r'(l)}{r(l)}\partial_l + \frac{1}{r^2(l)}\partial_\phi^2 - i\frac{r'(l)}{r^2(l)}\sigma_z\partial_\phi + 2i\frac{e}{\hbar}\frac{1}{r(l)}A(l)\partial_\phi\right]\psi \\
&\quad +\left[-\frac{1}{4}\frac{r'^2(l)}{r^2(l)} + \frac{e}{\hbar}\frac{r'(l)}{r(l)}A(l)\sigma_z - \frac{e^2}{\hbar^2}A^2(l)\right]\psi\,.
\end{aligned}
\tag{3.23}
$$

The Schrödinger Hamiltonian can be defined in the usual way as

$$\hat{H}_S = -\frac{\hbar^2}{2m^*}\Delta\,, \tag{3.24}$$

where m^* is the effective mass.

3.5. Schrödinger-Lichnerowicz theorem

Both, the square of the Dirac operator $\not{D}^2$, as well as the Laplacian Δ are second order differential operators originating from the same covariant exterior derivative D. It is an educated guess that these two operators are in no way independent but rather intimately linked to each other. This is indeed the case. The relation between them in the absence of a gauge field is given by the *Schrödinger-Lichnerowicz theorem* [74, 75]. In case a gauge field is present, a generalization of it, the *Schrödinger-Lichnerowicz theorem for twisted Dirac operators* [90] holds. For the sake of simplicity, we will not give it in the most general form but taylored to our developed formalism,

$$\not{D}^2 = \Delta - \frac{R}{4} + \frac{i}{4}\frac{e}{\hbar}F_{ab}[\gamma^a,\gamma^b]\,, \tag{3.25}$$

where R is the scalar curvature (Ricci scalar) and F_{ab} are the components of the field strength tensor in orthonormal coordinates. Note, that compared to the standard definition in differential geometry, the signs of the two correction terms are reversed since we use a positive signature of the Clifford algebra, as well as a positive definiteness of the Laplacian. In case of surfaces, it is more convenient to use the Gaussian curvature K, rather than R. They are related by $R = 2K$ [28]. Inserting the field strength tensor as well as our choices of gamma matrices, we arrive at

$$\not{D}^2 = \Delta - \frac{K}{2} + \frac{e}{\hbar} B_\perp(l)\sigma_z \,. \tag{3.26}$$

We can easily conclude that for surfaces with constant Gaussian curvature and subject to an overall perpendicular magnetic field, the spectra of the Dirac and Schrödinger Hamiltonians can be related to each other algebraically since the difference between the squared Dirac operator and the Laplacian is just a constant.

3.6. Symmetries of the Dirac Hamiltonian

Symmetries are a powerful tool in almost all branches of physics. While continuous ones, on the one hand, lead to conserved quantities according to Noether's theorem [91], discrete ones, on the other hand, can simplify things enormously and reveal properties of the system under investigation without even calculating specific quantities. In this paragraph, we want to see which symmetries the Dirac Hamiltonian possesses and how they influence our discussion of Dirac Landau levels on curved surfaces.

We start with discrete symmetries and recall that the Dirac Hamiltonian is given by (Eq. (3.20))

$$\hat{H}_D = \hbar v_F \left[\sigma_x \left(-i\partial_l - i\frac{r'(l)}{2r(l)} \right) + \sigma_y \left(-i\frac{1}{r(l)}\partial_\phi + \frac{e}{\hbar}A(l) \right) \right] . \tag{3.27}$$

Based on [92], we can easily check from this whether the three fundamental discrete symmetries hold:

- *Chiral symmetry (CS)* is given if there is a unitary operator $\hat{U}_C$ such that $\hat{U}_C \hat{H}_D \hat{U}_C^\dagger = -\hat{H}_D$ holds. Obviously, σ_z anticommutes with the Hamiltonian so that $\hat{U}_C = \sigma_z$ fulfills this property. This means that the spectrum is symmetric with respect to $E = 0$ because if there is an eigenstate $|\psi\rangle$ with $\hat{H}_D|\psi\rangle = E|\psi\rangle$ then obviously $\hat{H}_D \hat{U}_C|\psi\rangle = -E\hat{U}_C|\psi\rangle$.

- *Time-reversal symmetry (TRS)* is given if there is a unitary operator $\hat{U}_T$ such that $\hat{U}_T \hat{H}_D^* \hat{U}_T^\dagger = \hat{H}_D$ holds. Such an operator does not exist, as long as $A(l) \neq 0$. However, without magnetic field, $A(l) = 0$ and we need an operator that anticommutes with σ_x and commutes with σ_y. It is easy to see, that $\hat{U}_T = \sigma_y$. A consequence of this symmetry is the existence of *Kramers pairs* when there is no magnetic field present. Given $|\psi\rangle$ such that $\hat{H}_D|\psi\rangle = E|\psi\rangle$ holds, then a short calculation yields that also $\hat{H}_D\hat{U}_T\mathscr{C}|\psi\rangle = E\hat{H}_D\hat{U}_T\mathscr{C}|\psi\rangle$, where $\mathscr{C}$ is the complex-conjugation operator. This means that every energy eigenvalue is (at least) double degenerate.

- *Particle-hole symmetry (PHS)* is given if there is a unitary operator $\hat{U}_P$ such that $\hat{U}_P\hat{H}_D^*\hat{U}_P^\dagger = -\hat{H}_D$ holds. This is not independent of the previous ones. There is no way that only two of the three symmetries discussed are present, either one, three or none exist [92]. Henceforth, since CS is always present, PHS will only hold whenever TRS holds, with vanishing magnetic field. In this case, the operator is easily found to be $\hat{U}_P = \sigma_x$.

To summarize this, CS always holds, implying symmetric spectrum with respect to $E = 0$, whereas TRS and PHS only hold in absence of a magnetic field. In this case, the eigenstates come in degenerate *Kramers pairs.*

A more general symmetry than TRS can be found if we allow another transformation simultaneously to time-reversal, the inversion of the magnetic field. We denote this by using different symbols for the Hamiltonians, $\hat{H}_D(B)$ for the original field configuration, and $\hat{H}_D(-B)$ for the inverted field configuration. Let us now assume that there is a unitary operator $\hat{U}_{TB}$, such that $\hat{U}_{TB}\hat{H}_D^*(B)\hat{U}_{TB}^\dagger = \hat{H}_D(-B)$. One can easily verify that $\hat{U}_{TB} = \sigma_y$ meets this. Now let $\hat{H}_D(B)|\psi\rangle = E|\psi\rangle$ hold, then it follows that

$$\begin{aligned} \hat{H}_D(-B)\hat{U}_{TB}\mathscr{C}|\psi\rangle &= \hat{U}_{TB}\hat{H}_D^*(B)\hat{U}_{TB}^\dagger\hat{U}_{TB}\mathscr{C}|\psi\rangle \\ &= \hat{U}_{TB}\hat{H}_D^*(B)\mathscr{C}|\psi\rangle \\ &= \hat{U}_{TB}\mathscr{C}\hat{H}_D(B)|\psi\rangle \\ &= \hat{U}_{TB}\mathscr{C}E|\psi\rangle \\ &= E\hat{U}_{TB}\mathscr{C}|\psi\rangle\,. \end{aligned} \tag{3.28}$$

This means that it is not necessary to compute the spectrum of $\hat{H}_D$ for all magnetic fields, but only for positive ones because the spectra only depend on $|B|$, not on the particular sign and the eigenstates for opposite field configurations are linked by $\hat{U}_{TB}$. We call this *time-reversal field-inversion symmetry (TRFIS).* Note that in the limit of vanishing magnetic field, we recover the relations of TRS.

Let us now look at continuous symmetries. It is necessary for this to turn to the time-dependent equation of motion,

$$i\hbar\partial_t\psi(t,l,\phi) = \hat{H}_D\psi(t,l,\phi)\,. \tag{3.29}$$

In the following, when applying Einstein's summing convention, we add a zeroth component to it, the time t. Noether's theorem is most conveniently applied in the Lagrange formulation. Given the (classical) Lagrangian

$$\mathcal{L} = \sqrt{\det g}\,\psi^\dagger\left[-i\hbar\partial_t + \hat{H}_D\right]\psi\,, \tag{3.30}$$

it is readily checked that the Euler-Lagrange equations for fields

$$\partial_\mu\left(\frac{\partial\mathcal{L}}{\partial(\partial_\mu\psi^\dagger)}\right) - \frac{\partial\mathcal{L}}{\partial\psi^\dagger} = 0,\ \partial_\mu\left(\frac{\partial\mathcal{L}}{\partial(\partial_\mu\psi)}\right) - \frac{\partial\mathcal{L}}{\partial\psi} = 0 \tag{3.31}$$

yield the desired equations of motion for ψ and $\psi^\dagger$.

The Lagrangian is obviously invariant under a global $U(1)$ transformation $\psi \to \exp(i\alpha)\psi$ and $\psi^\dagger \to \psi^\dagger \exp(-i\alpha)$, with $\alpha \in \mathbb{R}$. At the level of infinitesimal transformations, the field deformations read $\Delta\psi = i\alpha\psi$ and $\Delta\psi^\dagger = -i\alpha\psi^\dagger$, whereas the Lagrangian itself remains untouched. Noether's theorem then yields the conserved current [93]

$$\begin{aligned} \mathcal{J}^\mu_{U(1)} &= \frac{\partial\mathcal{L}}{\partial(\partial_\mu\psi)}\frac{\partial\Delta\psi}{\partial\alpha} + \frac{\partial\mathcal{L}}{\partial(\partial_\mu\psi^\dagger)}\frac{\partial\Delta\psi^\dagger}{\partial\alpha} \\ &= i\frac{\partial\mathcal{L}}{\partial(\partial_\mu\psi)}\psi\,, \end{aligned} \tag{3.32}$$

for which $\partial_\mu\mathcal{J}^\mu_{U(1)} = 0$. The components read explicitly

$$\begin{aligned} \mathcal{J}^t_{U(1)} &= \hbar r(l)|\psi|^2\,, \\ \mathcal{J}^l_{U(1)} &= \hbar v_F r(l)\psi^\dagger\sigma_x\psi\,, \\ \mathcal{J}^\phi_{U(1)} &= \hbar v_F \psi^\dagger\sigma_y\psi\,. \end{aligned} \tag{3.33}$$

This yields the conservation law

$$\partial_t|\psi|^2 + v_F\frac{1}{r(l)}\partial_l\left(r(l)\psi^\dagger\sigma_x\psi\right) + v_F\frac{1}{r(l)}\partial_\phi\left(\psi^\dagger\sigma_y\psi\right) = 0\,. \tag{3.34}$$

We compare this to the general form of a continuity equation, with the divergence given in our curvilinear coordinates (Eq. (3.9)),

$$0 = \partial_t\rho + \mathrm{div}\vec{j} = \frac{1}{r(l)}\partial_l\left(r(l)j^1\right) + \frac{1}{r(l)}\partial_\phi j^2\,. \tag{3.35}$$

Identifying the charge density $\rho = -e|\psi|^2$, the current density is given by

$$\vec{j} = -ev_F\left(\psi^\dagger\sigma_x\psi\vec{e}_1 + \psi^\dagger\sigma_y\psi\vec{e}_2\right)\,. \tag{3.36}$$

We therefore obtained a charge (particle) conservation law from the global $U(1)$ symmetry, as one would also expect in relativistic field theories in flat Minkowski space.

Looking at the Lagrangian, another symmetry immediately catches the eye, the coordinate ϕ is cyclic and the equations of motion thus invariant under a shift $\phi \to \phi+\alpha$. We can interpret this as a $SO(2)$ symmetry. Again, when considering infinitesimal shifts, the field deformations read $\Delta\psi = \alpha\partial_\phi\psi$ and $\Delta\psi^\dagger = \alpha\partial_\phi\psi^\dagger$. Note here, that also the Lagrangian changes by a covariant divergence $\Delta\mathcal{L} = \alpha\partial_\phi\mathcal{L} = \alpha\partial_\mu(\delta^\mu_\phi\mathcal{L})$. The corresponding Noether current reads [93]

$$\begin{aligned} \mathcal{J}^\mu_{SO(2)} &= \frac{\partial\mathcal{L}}{\partial(\partial_\mu\psi)}\frac{\partial\Delta\psi}{\partial\alpha} + \frac{\partial\mathcal{L}}{\partial(\partial_\mu\psi^\dagger)}\frac{\partial\Delta\psi^\dagger}{\partial\alpha} - \delta^\mu_\phi\mathcal{L} \\ &= \frac{\partial\mathcal{L}}{\partial(\partial_\mu\psi)}\partial_\phi\psi - \delta^\mu_\phi\mathcal{L}\,. \end{aligned} \tag{3.37}$$

This time, we only take a look at the zeroth component

$$\mathcal{J}^0_{SO(2)} = -i\hbar r(l)\psi^\dagger \partial_\phi \psi = r(l)\psi^\dagger \hat{J}^z_{can}\psi\,, \tag{3.38}$$

where $\hat{J}^z_{can} = -i\hbar\partial_\phi$ can be identified as the canonical angular momentum operator in z-direction, whose expectation value is a conserved quantity. In presence of a magnetic field, the physical relevance of this is somewhat limited since it is not gauge invariant (contrary to the kinetic angular momentum) but rather an emerging symmetry due to gauge fixing. However, it allows us to simplify the Dirac equation further.

4. Dirac Landau levels on curved surfaces

This chapter is devoted to the computation of Landau levels of massless Dirac electrons on curved surfaces of revolution. In the first part of it, we study general properties of the corresponding Dirac equation. We will see that the problem carries a supersymmetric structure which enables us to proof many properties without assuming a specific surface. As a first example, we discuss the Dirac Landau levels on a pseudosphere. The spectrum for the case of an overall perpendicular magnetic field is given by a a general theorem for surfaces with constant Gaussian curvature, which is a central result of Spin geometry [30]. It has also been found by the author of this thesis in his Master project using a power series expansion [76]. We will complement this analysis by using two different approaches to find the spectrum, an algebraic one which exploits the shape invariance of the effective potential, as well as an analytical one, which reduces the problem to a differential equation. We further provide a closed formula for the wavefunctions. After this, we also study the corresponding problem for a coaxial magnetic field. It turns out that this can only be solved using semiclassical methods. We do this in two ways. First of all, we use an asymptotic solution for the differential equation which arises in this problem and second we use the SWKB method. In the second part of this chapter we examine Landau levels in a coaxial field for a general class of surfaces which is characterized by the condition $r'(l) \propto r^{\gamma}(l)$. We find the spectrum using SWKB and with this proof a conjecture, which can be found in [77], about the asymptotic scaling of Landau level energies as a function of magnetic field. A variation of this proof can be found in [29] but the original version, which is presented in this thesis, was solely made by the author of this thesis. We verify our findings with numerical calculations.

4.1. General concepts

We can directly use the cyclic coordinate ϕ by noticing that $\left[\hat{H}_D, \hat{J}^z_{can}\right] = 0$ (the continuous symmetry shows up in both, Lagrangian and Hamiltonian formalism). Therefore, common eigenstates of $\hat{H}_D$ and $\hat{J}^z_{can}$ exist. The eigenvalue equation

$$\hat{J}^z_{can}\chi(\phi) = -i\hbar\partial_\phi\chi(\phi) = \hbar m\chi(\phi)\,, \tag{4.1}$$

is obviously solved by $\chi(\phi) = \exp(im\phi)$. Note that because the spin quantization axis is not fixed with respect to the lab frame, but rotates with the local coordinates, we have to choose an antiperiodic boundary condition, $\chi(2\pi) = -\chi(0)$, which directly corresponds to the constraint $m \in (\mathbb{Z} + 1/2)$ [24, 26, 27]. We could derive this in a more pedestrian way in Chapter 2 for the Dirac equation on a flat plane in polar coordinates.

Separating coordinates by setting $\psi(l,\phi) = r^{-1/2}(l)\Psi(l)\chi(\phi)$ leads us to the radial Dirac equation

$$\hat{H}_D^R\Psi(l) := \hbar v_F\left[-i\sigma_x\partial_l + \sigma_y V(l)\right]\Psi(l) = E\Psi(l)\,, \tag{4.2}$$

where we defined the effective potential $V(l) = m/r(l) + e/\hbar A(l)$. It consists of a centrifugal and a magnetic part. Note that by the factor of $r^{-1/2}(l)$ in the ansatz, we could immediately get rid of the spin connection term.

Before we continue developing a solution strategy, it is worth taking a closer look at the effective potential in the important case of a coaxial magnetic field, where it reads $V(l) = m/r(l) + \nu r(l)/a^2$. An interesting symmetry catches the eye when taking a closer look at the scaling behavior of the magnetic and centrifugal terms. While the first mentioned scales with $r(l)$, the last mentioned goes with $1/r(l)$. This suggests that the roles of angular quantum number m and magnetic field ν are interchanged upon replacing the surface defined by $r(l)$ with one defined by the radial profile $\tilde{r}(l) \propto 1/r(l)$. This has first been discovered by Dusa [29, 77].

We can exploit the simple spinor structure of the Hamiltonian by writing the radial Dirac equation in matrix form,

$$\hbar v_F\begin{pmatrix}0 & \hat{A}^\dagger\\ \hat{A} & 0\end{pmatrix}\Psi(l) = E\Psi(l)\,, \tag{4.3}$$

where we defined $\hat{A} = -i\partial_l + iV(l)$ and its adjoint operator $\hat{A}^\dagger = -i\partial_l - iV(l)$. This is a system of two coupled first order differential equations.

In case of $E = 0$, they decouple and two solutions can easily be obtained by simple integration,

$$\Psi_0^\uparrow(l)\begin{pmatrix}1\\0\end{pmatrix} = \exp\left(\int dl\, V(l)\right)\begin{pmatrix}1\\0\end{pmatrix}\,, \tag{4.4}$$

$$\Psi_0^\downarrow(l)\begin{pmatrix}0\\1\end{pmatrix} = \exp\left(-\int dl\, V(l)\right)\begin{pmatrix}0\\1\end{pmatrix}\,. \tag{4.5}$$

Of course, it has to be checked in any case if these formal solutions are indeed normalizable and therefore valid. This depends on the magnetic field configuration, as well as the particular geometry. Note that vice versa, once an $E = 0$ wavefunction is known, the potential can be recovered by [78]

$$V(l) = \partial_l \log\left(\Psi_0^\uparrow(l)\right)\,, \tag{4.6}$$

$$V(l) = -\partial_l \log\left(\Psi_0^\downarrow(l)\right)\,. \tag{4.7}$$

If we assume $E \neq 0$, the system does not decouple. Plugging one component into the other yields two Schrödinger-like equations for each component of the spinor,

$$\begin{aligned} E^2\psi^\uparrow(l) &= \hbar^2 v_F^2 \hat{A}^\dagger\hat{A}\psi^\uparrow(l) \\ &= \hbar^2 v_F^2\left(-\partial_l^2 + V'(l) + V^2(l)\right)\psi^\uparrow(l) \\ &= \hbar^2 v_F^2\left(-\partial_l^2 + V_{S+}(l)\right)\psi^\uparrow(l) \\ &=: \hat{H}_D^{2\uparrow}\psi^\uparrow(l)\,, \end{aligned} \tag{4.8}$$

$$\begin{aligned} E^2\psi^{\downarrow}(l) &= \hbar^2 v_F^2 \hat{A}\hat{A}^{\dagger}\psi^{\downarrow}(l) \\ &= \hbar^2 v_F^2 \left(-\partial_l^2 - V'(l) + V^2(l)\right)\psi^{\downarrow}(l) \\ &= \hbar^2 v_F^2 \left(-\partial_l^2 + V_{S-}(l)\right)\psi^{\downarrow}(l) \\ &=: \hat{H}_D^{2\downarrow}\psi^{\downarrow}(l)\,, \end{aligned} \tag{4.9}$$

where we introduced $V_{S\pm} = \pm V'(l) + V^2(l)$. It is evident that the operators $\hat{H}_D^{2\uparrow}$ and $\hat{H}_D^{2\downarrow}$ are SUSY partner Hamiltonians with SUSY partner potentials $V_{S\pm}$ and SUSY superpotential $V(l)$. They therefore share the same spectrum, perhaps except for the ground state. If either of the zero energy solutions exists, SUSY is unbroken, whereas it is broken in the converse case.

Recall from Chapter 2 (Eq. (2.4)) that the partner potentials are shape invariant if

$$V_{S-}(a_1, l) = V_{S+}(a_2, l) + R(a_1)\,, \tag{4.10}$$

where a_1 denotes a family of parameters, $a_2 = f(a_1)$ and $R(a_1)$ functions of a_1. Since in our case $A(l) \propto B$, we can identify $a_1 = (m, B)$ and easily see that $a_2 = (-m, -B)$ and $R(a_1) = 0$ fulfill the desired property. This case of shape invariance is almost trivial because $R(a_+)$ vanishes and the transformation returns the Hamiltonians to their original state after two steps (it is an involution). In general, this is not enough to construct the whole bound state spectrum. If we impose a certain form $r(l)$ of the surface and a specific magnetic field $A(l)$, we may find a stronger form of shape invariance which allows the algebraic construction of the spectrum. We will do this for a specific example at a later stage of the work.

Even in case we cannot find a shape invariance which is strong enough to derive the spectrum from it, SUSY can help us understanding the structure of the eigenstates using properties summarized in Chapter 2. In our case, the partner Hamiltonians do not describe different systems but only the two spinor components of the wavefunction of a single system. In case SUSY is unbroken, $\hat{H}_D^{2\uparrow}$ or $\hat{H}_D^{2\downarrow}$ have a ground state with $E = 0$ which the other Hamiltonian does not possess. The remaining eigenvalues are shared by both but the n-th eigenstate of the Hamiltonian without the distinct ground state (with $(n-1)$ nodes) then corresponds to the $(n+1)$-th eigenstate of the one with the distinct ground state (with n nodes). This means that the ground state of the original Dirac Hamiltonian $\hat{H}_D^R$ has $E = 0$, is fully spin polarized and has no nodes. The n-th excited state has one component wavefunction with n nodes and one with $(n-1)$ nodes. In case of broken SUSY, both partner Hamiltonians have the same spectrum. The n-th state of the first one corresponds to the n-th state of the second one. The original Dirac operator $\hat{H}_D^R$ has no eigenstate with $E = 0$ and both component wavefunctions of the n-th eigenstate have $(n-1)$ nodes. Note, that independent on the brokenness of SUSY, we can always choose one spin component to be purely real. Using Eq. (4.3), one easily sees that then the remaining component is purely imaginary.

A general criterion on whether SUSY is unbroken or broken can be found in [78] and explained as follows. Since the ground state is nodeless, the wavefunction needs to have a local maximum and decay towards the boundaries (for $l \to 0$ and $l \to \infty$). Therefore, a critical point with $\partial_l \Psi_0^{\uparrow/\downarrow} = 0$ must exist. Due to monotonity of the logarithm, this is equivalent to $\partial_l \log\left(\Psi_0^{\uparrow/\downarrow}\right) = 0$. We easily see, using Eq. (4.6) and Eq. (4.7), that this directly corresponds to the requirement of the potential $V(l)$ changing sign. In case of a coaxial field, for $B > 0$, we require $m < 0$ and $m > 0$ for $B < 0$. The type of monotonity of $r(l)$ then decides, which term, the magnetic or the centrifugal, dominates in the limit $l \to \infty$ and whether $\Psi_0^{\uparrow}$ or $\Psi_0^{\downarrow}$ is a proper solution. The case of a perpendicular magnetic field is more involved, since the sign of the integrals in Eq. (4.4) and Eq. (4.5) is not clear without further assumptions.

While zero energy solutions may be found by simple integration (Eq. (4.4) and Eq. (4.5)), non-zero energy solutions are more involved. We want to give a general ansatz for finding them. A common method is to assume that the asymptotics of the $E = 0$ state is also correct for the excited states and their shape only differs locally. This justifies the ansatz $\Psi^{\uparrow/\downarrow}(l) = p^{\uparrow/\downarrow}(l)\Psi_0^{\uparrow/\downarrow}(l)$, where $p^{\uparrow/\downarrow}(l)$ is an unknown function, and directly yields the differential equations

$$p^{\uparrow\prime\prime}(l) + 2p^{\uparrow\prime}(l)V(l) + \frac{E^2}{\hbar^2 v_F^2} p^{\uparrow}(l) = 0\,, \tag{4.11}$$

$$p^{\downarrow\prime\prime}(l) - 2p^{\downarrow\prime}(l)V(l) + \frac{E^2}{\hbar^2 v_F^2} p^{\downarrow}(l) = 0\,. \tag{4.12}$$

Before starting with concrete examples, we have to talk about a few open issues. First of all, we note that many surfaces can be defined in a very similar form, $r(l) = af(l/a)$, where f is only a function of the ratio l/a and $f(0) = 1$. It turns out that in this case we can write the Dirac equation in a scale invariant form for the coaxial magnetic field using the previously defined dimensionless quantities $\epsilon = Ea/(\hbar v_F)$ and $\nu = \Phi/\Phi_0$. This comes with the price that we also have to rescale the coordinate l. For the sake of clarity, we will not go this way to the fullest and stick to the original Dirac equation, only using ϵ and ν loosely whenever appropriate.

A second open point is that the boundary condition at $l = 0$ has not yet been specified. When solving the Dirac equation analytically, we always assume atomic boundary conditions, which means that the wavefunction decays exponentially towards the boundary. We ignore possible, small probability densities outside the surface, i.e. for $l < 0$ and only demand exponential localization.

In case of numerical calculations, we simply only build a numerical lattice for $l \geq 0$, effectively imposing a hard wall boundary condition. As many of our surfaces are not compact, we have to introduce a lattice cut-off at $l = L$. We do this at a point, where we are sure that the wavefunction is virtually zero and the cut-off does not spoil the numerical results. Throughout this thesis, we only solve the radial Dirac equation numerically which is effectively one dimensional. A fully numerical treatment of both coordinates, l and ϕ increases computational costs enormously without any benefit, as the solution of the azimuthal part of the Dirac equation is trivial.

In conjunction with this, we have to discuss a problem which arises when using different boundary conditions for the analytical and numerical treatment, as well as considering zero energy states. Analytically, a zero energy state may exist when assuming atomic boundary conditions. Numerically, however, the situation is more complicated. When starting without a magnetic field, energies are fully determined by size quantization, a zero energy mode does not exist. Upon increasing the magnetic field, the two states closest to $E = 0$ (one with positive, one with negative energy due to chiral symmetry), $|\psi_0^+\rangle$ and $|\psi_0^-\rangle$, condense onto $E = 0$ in the limit of $B \to \infty$. Therefore, two eigenenergies converge to zero but are still not exactly zero for finite B. As explained in Chapter 3, these two eigenstates are linked to each other by the chiral symmetry operator σ_z. Since the Hamiltonian is hermitian, both eigenstates have to be orthogonal to each other, yielding $0 = \langle\psi_0^-|\psi_0^+\rangle = \langle\psi_0^+|\sigma_z|\psi_0^+\rangle$. Consequently, each spinor component equally contributes to the norm. Note that this does not restrict to the (almost) zero energy states. Chiral symmetry henceforth guarantees vanishing spin polarization of σ_z of all eigenstates. In case of the zero energy states, this leads to the problem that analytically we expect fully spin polarized states, which we cannot get numerically, as we asserted in this paragraph. We therefore have to expect artifacts in one of the spinor components.

To conclude this paragraph, we have to talk about degeneracy of eigenstates. We saw in Chapter 2 that in case of the flat plane, the degeneracy of Landau levels is given by the number of flux quanta piercing the surface [10, 84]. In case of curved surfaces, powerful index theorems from Spin geometry, like the *Atiyah-Singer index theorem* [94], hold and in some situations can give the degeneracy of the ground state [95, 96]. However, we will not go this way and do not care too much about quantitatively determining the degeneracy in the following. In general, it can be estimated by counting the eigenstates with equal energy which are localized within the surface. A good approximation for this is to demand the minimum of the effective potential to be located at $l > 0$ [27].

Throughout this chapter we assume $B > 0$, as chiral symmetry automatically yields corresponding results for $B < 0$.

4.2. Pseudosphere

As a first example, we consider the pseudosphere which is a surface with constant Gaussian curvature. A parametrization for the maximum radius being unity is given in [97] and can easily be extended to a maximum radius of a,

$$\Sigma : [0,\infty) \times [0, 2\pi] \to \mathbb{R}^3, (u,\phi) \mapsto \begin{pmatrix} \frac{a}{\cosh u} \cos\phi \\ \frac{a}{\cosh u} \sin\phi \\ a(u - \tanh u) \end{pmatrix}, \tag{4.13}$$

where we easily identify the radius as $r(u) = a/\cosh(u)$. We need to calculate

$$\frac{dz}{dr} = \frac{dz}{du}\left(\frac{dr}{du}\right)^{-1} = a\tanh^2 u \left(-\frac{\sinh u}{\cosh^2 u}\right)^{-1} = -\sinh u\,, \tag{4.14}$$

which gives

$$\left(\frac{dz}{dr}\right)^2 = \sinh^2 u = \cosh^2 u - 1 = \frac{a^2}{r^2} - 1\,. \tag{4.15}$$

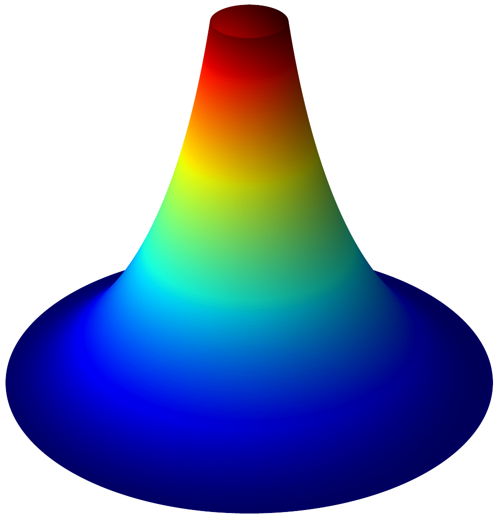

Figure 4.1: An exemplary pseudosphere. The colormap is exclusively used for better visualization and does not have any deeper meaning.

With this we can easily compute

$$l(r) = \int_r^a d\tilde{r} \sqrt{1 + \left(\frac{dz}{d\tilde{r}}\right)^2} = a \int_r^a d\tilde{r} \, \frac{1}{\tilde{r}} = a \log\left(\frac{a}{r}\right) . \tag{4.16}$$

The inverse relation is given by

$$r(l) = a \exp\left(-\frac{l}{a}\right) . \tag{4.17}$$

Fig. 4.1 shows an exemplary pseudosphere. In the following, we first of all take a look at the case of a perpendicular magnetic field and afterwards tackle the issue of a coaxial one.

4.2.1. Perpendicular magnetic field

Let us first have a look at the overall perpendicular magnetic field. The vector potential is given by (Eq. (3.14))

$$A(l) = -\frac{B}{r(l)} \int dl \, r(l) = -B \exp\left(\frac{l}{a}\right) \int dl \, \exp\left(-\frac{l}{a}\right) = Ba \, . \tag{4.18}$$

The effective potential therefore reads

$$V(l) = \frac{m}{a} \exp\left(\frac{l}{a}\right) + \frac{a}{l_B^2} \, . \tag{4.19}$$

A simple integration gives the two potential candidates for a zero energy solution,

$$\Psi_0^{\uparrow}(l)\begin{pmatrix}1\\0\end{pmatrix} = r(l)^{-\frac{a^2}{\tilde{l}_B^2}} \exp\left(+m\frac{a}{r(l)}\right)\begin{pmatrix}1\\0\end{pmatrix}, \tag{4.20}$$

$$\Psi_0^{\downarrow}(l)\begin{pmatrix}0\\1\end{pmatrix} = r(l)^{+\frac{a^2}{\tilde{l}_B^2}} \exp\left(-m\frac{a}{r(l)}\right)\begin{pmatrix}0\\1\end{pmatrix}. \tag{4.21}$$

Note, that the wavefunctions can explicitly be written as functions of l but we chose to keep $r(l)$ (Eq. (4.17)) for convenience. Only the first solution with $m < 0$ is possible, leaving SUSY unbroken. Inspecting the effective potential makes obvious that for the other branch of the angular quantum number m, not only SUSY is broken, but there are no bound states localized within the pseudosphere at all (see [27] for details).

Excited states - analytical way

We try to find excited states by solving Eq. (4.11),

$$p^{\uparrow\prime\prime}(l) + \left[\frac{2m}{a}\exp\left(\frac{l}{a}\right) + \frac{2a}{\tilde{l}_B^2}\right]p^{\uparrow\prime}(l) + \frac{E^2}{\hbar^2 v_F^2}p^{\uparrow}(l) = 0\,. \tag{4.22}$$

It makes sense to perform a coordinate transformation to the radius $r(l) = a\exp(-l/a)$. This yields

$$\left[r^2\partial_r^2 - \left(2ma + \frac{2a^2 r}{\tilde{l}_B^2} - r\right)\partial_r + \frac{a^2E^2}{\hbar^2 v_F^2}\right]p^{\uparrow}(r) = 0\,. \tag{4.23}$$

It is shown in Appendix A.2 (Eq. (A.13)) that the eigenevalues are then given by

$$\frac{a^2E^2}{\hbar^2 v_F^2} = -n^2 + n\frac{2a^2}{\tilde{l}_B^2}\,, \tag{4.24}$$

which finally yields

$$E_n = \pm\frac{\hbar v_F}{a}\sqrt{n\left(\frac{2a^2}{\tilde{l}_B^2} - n\right)}\,. \tag{4.25}$$

The corresponding (unnormalized) up component wavefunction is given by Eq. (A.15),

$$\Psi_n^{\uparrow}(r) = r^n L_n^{(-2n+2a^2/\tilde{l}_B^2)}\left(-\frac{(2m+1)a}{r}\right)\Psi_0^{\uparrow}(r)\,, \tag{4.26}$$

where we used the *associated Laguerre polynomials* $L_n^{(a)}(x)$ [98]. The down component wavefunction can easily be obtained using Eq. (4.3),

$$\begin{aligned}\Psi_n^{\downarrow}(r) &= \frac{\hbar v_F}{aE_n}\hat{A}\Psi_n^{\uparrow} \qquad (4.27)\\ &= i\frac{\hbar v_F}{aE_n}\left(-n + \frac{2a^2}{\tilde{l}_B^2}\right)r^n L_{n-1}^{(-2n+2a^2/\tilde{l}_B^2)}\left(-\frac{(2m+1)a}{r}\right)\Psi_0^{\uparrow}(r)\,.\end{aligned}$$

Excited states - algebraic way

To complement this, we want to derive the spectrum in an algebraic way, exploiting the translational shape invariance of the SUSY partner potentials which allows us to generate the whole spectrum starting from the ground state. The relevant parameter is B and the transforming functions are, introducing $k = e/\hbar$, $f(B) = B - 1/(ka^2)$ and $R(B_i) = 2kB_i - 1/a^2$ (see Appendix A.3 for a proof). Starting from $B_1 = B$, B_i is defined as $B_i = f^{i-1}(B)$. It is obvious that in closed form

$$B_i = B - \frac{i-1}{ka^2}\,. \tag{4.28}$$

The n-th eigenvalue of $\hat{H}_D^{2\uparrow}$ (starting from $n = 0$) is then given by Eq. (2.5),

$$\begin{aligned}
E_n^2 &= \hbar^2 v_F^2 \sum_{i=1}^{n} R(B_i) &\quad (4.29)\\
&= \hbar^2 v_F^2 \sum_{i=1}^{n} \left[2k\left(B - \frac{i-1}{ka^2}\right) - \frac{1}{a^2}\right]\\
&= \hbar^2 v_F^2 \sum_{i=1}^{n} \left(2kB - \frac{2i-1}{a^2}\right)\\
&= \hbar^2 v_F^2 \left(2kBn + \frac{1}{a^2}n - \frac{2}{a^2}\sum_{i=1}^{n} i\right)\\
&= \hbar^2 v_F^2 \left(2kBn + \frac{1}{a^2}n - \frac{2}{a^2}\frac{n(n+1)}{2}\right)\\
&= \frac{\hbar^2 v_F^2}{a^2}\left(\frac{2a^2}{\tilde{l}_B^2}n - n^2\right)\,.
\end{aligned}$$

This gives the final eigenenergies of $\hat{H}_D^R$,

$$E_n = \pm\frac{\hbar v_F}{a}\sqrt{n\left(\frac{2a^2}{\tilde{l}_B^2} - n\right)}\,. \tag{4.30}$$

The n-th (unnormalized) up component wavefunction is given by [78]

$$\Psi_n^\uparrow(l, B) = \hat{A}^\dagger(B_1)\hat{A}^\dagger(B_2)...\hat{A}^\dagger(B_n)\Psi_0^\uparrow(l, B_{n+1})\,, \tag{4.31}$$

whereas the corresponding down component can easily be obtained from Eq. (4.3) as

$$\Psi_n^\downarrow(l, B) = \frac{\hbar v_F}{E_n}\hat{A}(B_1)\hat{A}^\dagger(B_1)\hat{A}^\dagger(B_2)...\hat{A}^\dagger(B_n)\Psi_0^\uparrow(l, B_{n+1})\,. \tag{4.32}$$

Contrary to the eigenenergies, we will not simplify the wavefunctions further, as this is very cumbersome and will eventually lead to the same results as already gained analytically (Eq. (4.26) and Eq. (4.27)).

Excited states - comparison

The eigenenergies agree with each other as well as with previous findings in [27, 30]. We see that at fixed magnetic field, only a finite number of different Landau energies is available. Further, all levels are degenerate in the angular quantum number $m < 0$. A comparison of the eigenenergies, as well as the eigenfunctions, to numerical calculations can be found in [27], where it can be observed that they match perfectly well for strong magnetic fields ($l_B << a$, so that the eigenstates are localized within the pseudosphere). It remains to say that shape invariance is a very rare property of potentials, with many of them being classified and well-known. When taking a closer look at the effective potential, Eq. (4.19), one can easily check that it is a superpotential of the *Morse potential* [99].

4.2.2. Coaxial magnetic field

For the experimentally more relevant case of a coaxial magnetic field, the effective potential is given by

$$V(l) = \frac{m}{a} \exp\left(\frac{l}{a}\right) + \frac{\nu}{a} \exp\left(-\frac{l}{a}\right) . \tag{4.33}$$

Again, a simple integration yields two possible $E = 0$ solutions,

$$\Psi_0^{\uparrow}(l) \begin{pmatrix} 1 \\ 0 \end{pmatrix} = \exp\left(m\frac{a}{r(l)} - \frac{\nu}{a} r(l)\right) \begin{pmatrix} 1 \\ 0 \end{pmatrix} , \tag{4.34}$$

$$\Psi_0^{\downarrow}(l) \begin{pmatrix} 0 \\ 1 \end{pmatrix} = \exp\left(-m\frac{a}{r(l)} + \frac{\nu}{a} r(l)\right) \begin{pmatrix} 0 \\ 1 \end{pmatrix} . \tag{4.35}$$

Since $V(l)$ has to change sign, as discussed at the beginning of this chapter, and the wavefunction has to vanish at $l \to \infty$, the only possible solution is the one for spin-up and $m < 0$. In this case SUSY is unbroken. SUSY is broken for $m > 0$, but this time, contrary to the case of the overall perpendicular field, bound states with $E \neq 0$ can exist, as we shall see in the following.

Excited states - analytical way

We try to find excited states by solving the differential equation (Eq. (4.11))

$$p^{\uparrow''}(l) + 2\left[\frac{m}{a} \exp\left(\frac{l}{a}\right) + \frac{\nu}{a} \exp\left(-\frac{l}{a}\right)\right] p^{\uparrow'}(l) + \frac{E^2}{\hbar^2 v_F^2} p^{\uparrow}(l) = 0 . \tag{4.36}$$

Again, it makes sense to perform the substitution $r(l) = a \exp(-l/a)$, which gives

$$r^2 p^{\uparrow''}(r) + \left[-2ma + r - \frac{2\nu}{a} r^2\right] p^{\uparrow'}(r) + a^2 \epsilon^2 p^{\uparrow}(r) = 0 . \tag{4.37}$$

This is a *Doubly-Confluent Heun Equation (DCHE)* [98]. Before continuing, we note that further insight can be gained performing the rescaling $\tilde{r} = \frac{2r}{a}\nu$, resulting in

$$\tilde{r}^2 p^{\uparrow''}(\tilde{r}) + \left[-4m\nu + \tilde{r} - \tilde{r}^2\right] p^{\uparrow'}(r) + \epsilon^2 p^{\uparrow}(r) = 0 . \tag{4.38}$$

The two independent parameters, ν and m, only appear in a common coefficient. Since this differential equation encodes all spectral information (in case the wavefunction does not feel the boundary), we may assert that the exact eigenenergies are only a function of a single parameter, the product $m\nu$. This is by no means a coincidence but reflects a symmetry of the effective potential. When transforming to arclength coordinates, where the origin is at the potential minimum, done in the next section, we see that both exponential functions have the same exponent (up to a minus sign), condensing into a hyperbolic function. The effective potential is therefore symmetric around this point. The spectrum of the DCHE cannot be determined exactly, as a power series expansion leads to a more than two terms recurrence relation. However, in the limit of high magnetic fields, an asymptotic approximation in the small parameter $1/(m\nu)$ exists [100], yielding the constraint (up to second order)

$$\epsilon^2 = 4n\sqrt{-m\nu} + \frac{1}{2}n^2 - 1\,. \tag{4.39}$$

Clearly, this can only hold true if ν and m have opposite sign (when SUSY is unbroken). It turns out that we can find the spectrum for equal sign by solving Eq. (4.12). As this was not done by the author of this thesis, it is not covered at this point but details can be found in [27].

For the unbroken SUSY case, when $m < 0$, the eigenenergies ultimately read

$$\epsilon = \pm\sqrt{4n\sqrt{-m\nu} + \frac{1}{2}n^2 - 1}\,. \tag{4.40}$$

We can see, that in the limit of strong magnetic fields, $E \propto \nu^{1/4}$ holds, clearly deviating from the common linear (non-relativistic Schrödinger electrons) or square root (relativistic Dirac electrons) behavior. Further, the degeneracy in the angular quantum number is lifted for excited Landau level energies. Note that this asymptotic formula obviously does not correctly recover the zero energy Landau level.

Excited states - semiclassical way

We want to complement this calculation by computing the spectrum using the semiclassical supersymmetric WKB (SWKB) method. The minimum of $|V|$ is located at $l = \frac{a}{2}\log|\nu/m|$. As announced in the previous section, it makes sense to perform the coordinate transformation $\tilde{l} = l - \frac{l}{2}\log|\nu/m|$, shifting the origin to the minimum and resulting in

$$\begin{aligned} V(\tilde{l}) &= \frac{m}{a}\sqrt{\left|\frac{\nu}{m}\right|}\exp\left(\frac{\tilde{l}}{a}\right) + \frac{\nu}{a}\sqrt{\left|\frac{m}{\nu}\right|}\exp\left(-\frac{\tilde{l}}{a}\right) \\ &= \frac{\mathrm{sgn}(m)}{a}\sqrt{|m|\nu}\exp\left(\frac{\tilde{l}}{a}\right) + \frac{1}{a}\sqrt{|m|\nu}\exp\left(-\frac{\tilde{l}}{a}\right)\,. \end{aligned} \tag{4.41}$$

We also need the squared effective potential for SWKB,

$$V^2(\tilde{l}) = \frac{2}{a^2}|m|\nu \cosh\left(\frac{2\tilde{l}}{a}\right) + \frac{2}{a^2}m\nu\,. \tag{4.42}$$

Given the energy $\epsilon^2 \geq 0$ we define the shifted energy $\tilde{\epsilon}^2 = \epsilon^2 - 2m\nu$. Fixing $\tilde{\epsilon}^2$ and assuming that the particle does not touch the boundary, the two classical turning points are given by

$$\tilde{l}_\pm = \pm\frac{a}{2}\text{arcosh}\left|\frac{\tilde{\epsilon}^2}{2m\nu}\right|\,. \tag{4.43}$$

This directly yields the action (see Appendix A.4 for a detailed solution of the integral)

$$\begin{aligned} S &= 2\hbar\int_{\tilde{l}_-}^{\tilde{l}_+} d\tilde{l}\,\sqrt{\frac{\epsilon^2}{a^2} - V^2(\tilde{l})} \qquad (4.44)\\ &= \frac{4\hbar}{a}\int_0^{\tilde{l}_+} d\tilde{l}\,\sqrt{\tilde{\epsilon}^2 - 2|m|\nu\cosh\left(\frac{2\tilde{l}}{a}\right)} \\ &= 4\hbar\frac{\pi}{2}\frac{1}{2}\frac{\tilde{\epsilon}^2 - 2|m|\nu}{\sqrt{2\tilde{\epsilon}^2}}\,{}_2F_1\left(\frac{3}{2},\frac{1}{2};2;1-\frac{2|m|\nu}{\tilde{\epsilon}^2}\right) \\ &= \frac{\pi\hbar}{\sqrt{2}}(\tilde{\epsilon}^2)^{-\frac{1}{2}}\left(\tilde{\epsilon}^2 - 2|m|\nu\right)\,{}_2F_1\left(\frac{3}{2},\frac{1}{2};2;1-\frac{2|m|\nu}{\tilde{\epsilon}^2}\right) \\ &= \frac{\pi\hbar}{\sqrt{2}}(\tilde{\epsilon}^2)^{-\frac{1}{2}} f_1(\tilde{\epsilon},\nu) f_2(\tilde{\epsilon},\nu)\,, \end{aligned}$$

where ${}_2F_1(a,b;c;z)$ is the *Gaussian hypergeometric function* [98]. For convenience, we abbreviated the second factor of the final result as $f_1(\tilde{\epsilon},\nu)$ and the third as $f_2(\tilde{\epsilon},\nu)$. We need to invert the action as a function of energy to find the spectrum. However, this cannot be done exactly due to its complicated structure. Since we want to examine the behavior in presence of strong magnetic fields, it makes sense to take a look at the limit $\nu\to\infty$ and neglect subleading terms. We assume the relation between κ and ϵ to be some power function, so that in the strong field limit $\tilde{\epsilon}^2 = k\nu^\kappa$ for some $k > 0$ and $\kappa \in \mathbb{R}$. When doing asymptotic analysis of the action, we have to distinguish (at least) three possible cases, $\kappa < 1$ ($\tilde{\epsilon}^2$ grows slower than ν), $\kappa = 1$ ($\tilde{\epsilon}^2$ grows as fast as ν) and $\kappa > 1$ ($\tilde{\epsilon}^2$ grows faster than ν).

Let us focus on the case $\kappa > 1$ first of all. The first term takes the asymptotic form

$$\begin{aligned} f_1(\tilde{\epsilon},\nu) &\approx k\nu^\kappa - 2|m|\nu \qquad (4.45)\\ &\approx k\nu^\kappa\,, \end{aligned}$$

whereas the second one takes

$$\begin{aligned} f_2(\tilde{\epsilon},\nu) &\approx {}_2F_1\left(\frac{3}{2},\frac{1}{2};2;1-\frac{2|m|\nu}{k\nu^\kappa}\right) \qquad (4.46)\\ &\overset{[98]}{\approx} -\frac{\Gamma(2)}{\Gamma\left(\frac{3}{2}\right)\Gamma\left(\frac{1}{2}\right)}\log\left(\frac{2|m|}{k\nu^{\kappa-1}}\right)\,. \end{aligned}$$

The overall action must not depend on the magnetic field ν, as it is quantized to constant values. There is no term to compensate the logarithm in this factor, so $\kappa > 1$ is not possible.

The next case we want to examine further is $\kappa = 1$. The first term is special here,

$$f_1(\tilde{\epsilon}, \nu) \approx k\nu - 2|m|\nu\,, \tag{4.47}$$

as it has a zero in case $k = 2|m|$. Let us assume for the moment that k does not have this value. Then, we can approximate the second term as

$$\begin{aligned} f_2(\tilde{\epsilon}, \nu) &\approx {}_2F_1\left(\frac{3}{2}, \frac{1}{2}; 2; 1 - \frac{2|m|\nu}{k\nu}\right) \\ &\approx {}_2F_1\left(\frac{3}{2}, \frac{1}{2}; 2; 1 - \frac{2|m|}{k}\right)\,, \end{aligned} \tag{4.48}$$

which is just a constant. For the action to be constant, the overall exponent of ν has to vanish, leading to the constraint

$$-\frac{1}{2} + 1 = 0 \Leftrightarrow \frac{1}{2} = 0\,, \tag{4.49}$$

which obviously cannot be fulfilled. Let us now assume $k = 2|m|$. Then the action will vanish to leading order and we have to take the next to leading order into account, at least for the first term. This can be done by making the ansatz $\tilde{\epsilon}^2 = 2|m|\nu\left(1 + \tilde{k}\nu^\delta\right)$, with $\tilde{k} > 0$ and $\delta < 0$. For the first term, we now have

$$\begin{aligned} f_1(\tilde{\epsilon}, \nu) &\approx 2|m|\nu\left(1 + \tilde{k}\nu^\delta\right) - 2|m|\nu \\ &\approx 2|m|\tilde{k}\nu^{1+\delta}\,. \end{aligned} \tag{4.50}$$

The second term can be expanded as

$$\begin{aligned} f_2(\tilde{\epsilon}, \nu) &\approx {}_2F_1\left(\frac{3}{2}, \frac{1}{2}; 2; 1 - \frac{2|m|\nu}{2|m|\nu\left(1 + \tilde{k}\nu^\delta\right)}\right) \\ &\approx {}_2F_1\left(\frac{3}{2}, \frac{1}{2}; 2; 0\right) \\ &\approx 1\,. \end{aligned} \tag{4.51}$$

Balancing the exponents of ν yields

$$-\frac{1}{2} + (1 + \delta) = 0 \Leftrightarrow \delta = -\frac{1}{2}\,. \tag{4.52}$$

This is consistent. Inserting δ into our original ansatz determines

$$\tilde{k} = \frac{1}{\sqrt{|m|}}\left(2n + \Theta(m)\right)\,, \tag{4.53}$$

where we used the unbroken SUSY quantization condition for $m < 0$ and the broken SUSY quantization condition for $m > 0$. We do not need to examine the case $\kappa < 1$ anymore, as the solution for $\kappa = 1$ is dominant anyway. The overall energy finally reads

$$\epsilon = \pm\sqrt{2m\nu + 2|m|\nu + 2\sqrt{|m|\nu}\,(2n + \Theta(m))}\,. \tag{4.54}$$

We see that depending on the sign of m, we have two qualitatively different spectral branches. For $m > 0$, the first two terms under the radicand add up and give the dominant contribution for large magnetic fields, yielding an overall scaling of $\epsilon \propto \nu^{1/2}$, whereas for $m < 0$, they cancel and the next to leading order term becomes dominant, yielding a scaling of $\epsilon \propto \nu^{1/4}$. The degeneracy of the excited Landau level energies in m is again lifted, as we have seen before.

Excited states - numerical way and comparison

We want to perform numerical calculations to validate our analytically gained spectrum as well as to take a look at the wavefunctions of the Landau levels.

Fig. 4.2 and Fig. 4.3 show the first 20 (positive) Landau level energies for exemplary negative and positive angular quantum numbers, respectively. The black crosses mark numerically gained solutions, while the solid lines represent analytical solutions. The upper panels correspond to angular quantum numbers of $m = -1/2$ and $m = 1/2$, while the lower ones correspond to $m = -3/2$ and $m = 3/2$. The left panels show solutions gained from an asymptotic treatment of the Heun equation (Eq. (4.40) for $m < 0$ and Eq. 71 in [27] for $m > 0$). Correspondingly, the right ones show SWKB solutions (Eq. (4.54)).

In general, the agreement is good for strong magnetic fields ν. This is expected since our asymptotic treatment of the Dirac equation was explicitly based on the assumption that $l_B < a$. Quantitative agreement also becomes better for higher magnitude of the angular quantum number, which is plausible as well considering that we found that only the combined parameter $m\nu$ determines the spectrum.

When comparing Heun and SWKB solutions, we notice that the first mentioned seems to be more precise. This does not come as a surprise, as the expansion in the semiclassical parameter $1/(m\nu)$ was performed until second order in case of the Heun asymptotic approximation, and only until first order in case of SWKB. However, the SWKB approximation correctly predicts the zero energy level for negative m.

The agreement is best for small main quantum numbers n. Upon rising it, the Heun method overestimates the energy, while the SWKB method underestimates it. This might come unexpected, as asymptotic methods are usually associated with better results for higher energies. However, in this case we have to remember that the effective potential is $V(\tilde{l}) \propto \cosh\left(\tilde{l}/a\right)$, which means that the derivative (with respect to $\tilde{l}$) is $\propto \sinh\left(\tilde{l}/a\right)$. The potential changes exponentially when going away from the equilibrium point at $\tilde{l} = 0$, violating the requirement for semiclassical methods to work, slowly varying potential compared to the Fermi wavelength, more and more.

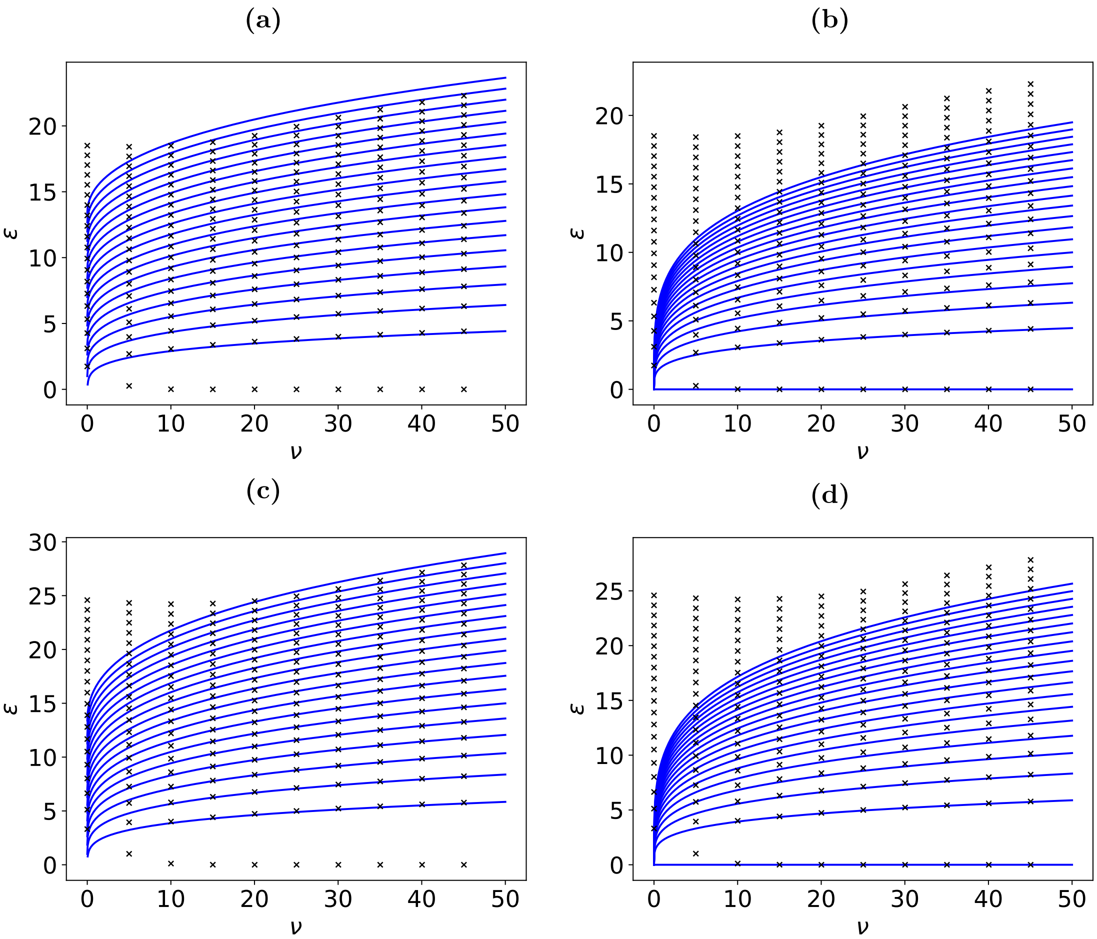

Figure 4.2: Lowest positive Dirac Landau level energies as a function of magnetic field ν of the pseudosphere in a coaxial magnetic field for $m = -1/2$ ((a) and (b)), as well as for $m = -3/2$ ((c) and (d)). Blue lines in figures (a) and (c) represent analytical solutions gained using asymptotic methods for the *DCHE* (Eq. (4.40)). Blue lines in figures (b) and (d) represent analytical solutions obtained using the SWKB approximation (Eq. (4.54)). Black crosses mark numerical solutions of the radial Dirac equation (Eq. (4.2)). A lattice spacing of $\Delta l = 0.005a$ as well as a cut-off of $L = 5a$ were used.

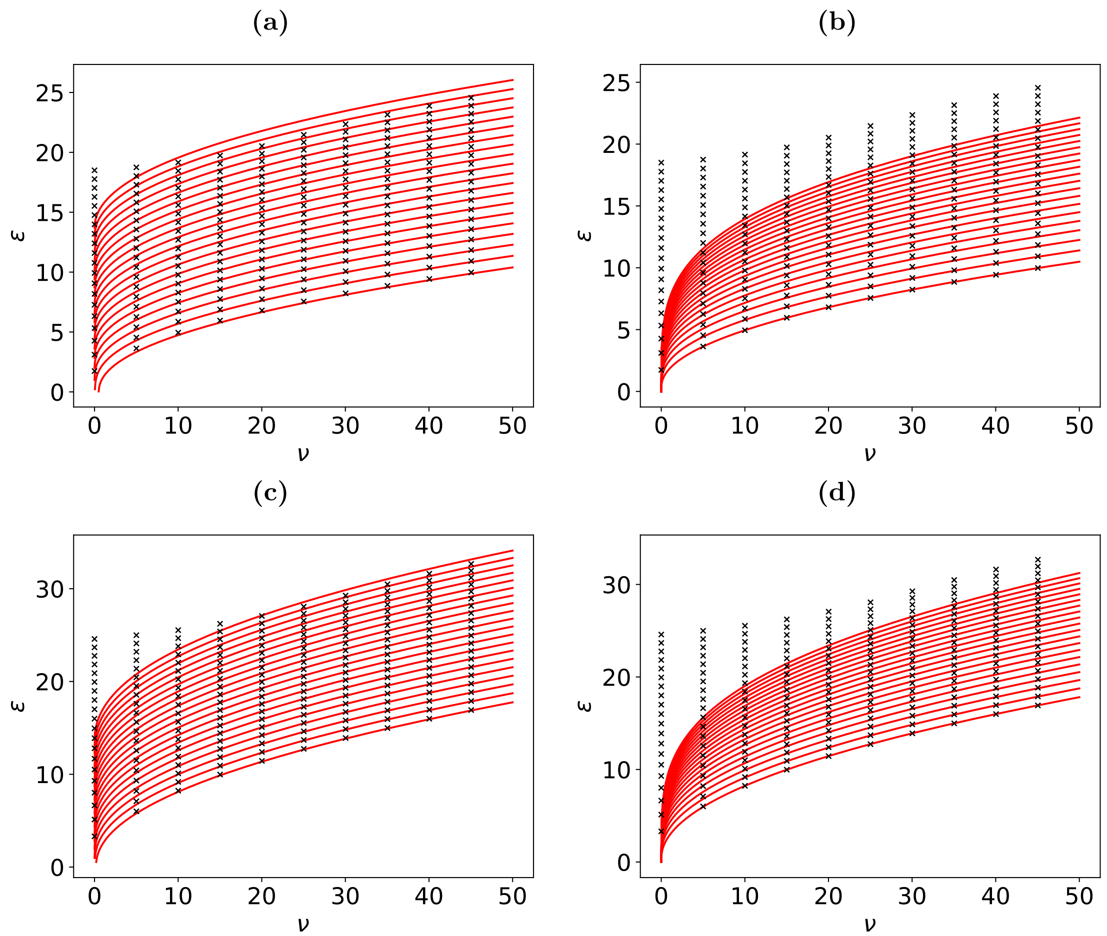

Figure 4.3: Lowest positive Dirac Landau level energies as a function of magnetic field ν of the pseudosphere in a coaxial magnetic field for $m = 1/2$ ((a) and (b)), as well as for $m = 3/2$ ((c) and (d)). Red lines in figures (a) and (c) represent analytical solutions gained using asymptotic methods for the *DCHE* (Eq. (71) in [27]). Red lines in figures (b) and (d) represent analytical solutions obtained using the SWKB approximation (Eq. (4.54)). Black crosses mark numerical solutions of the radial Dirac equation (Eq. (4.2)). A lattice spacing of $\Delta l = 0.005a$ as well as a cut-off of $L = 5a$ were used.

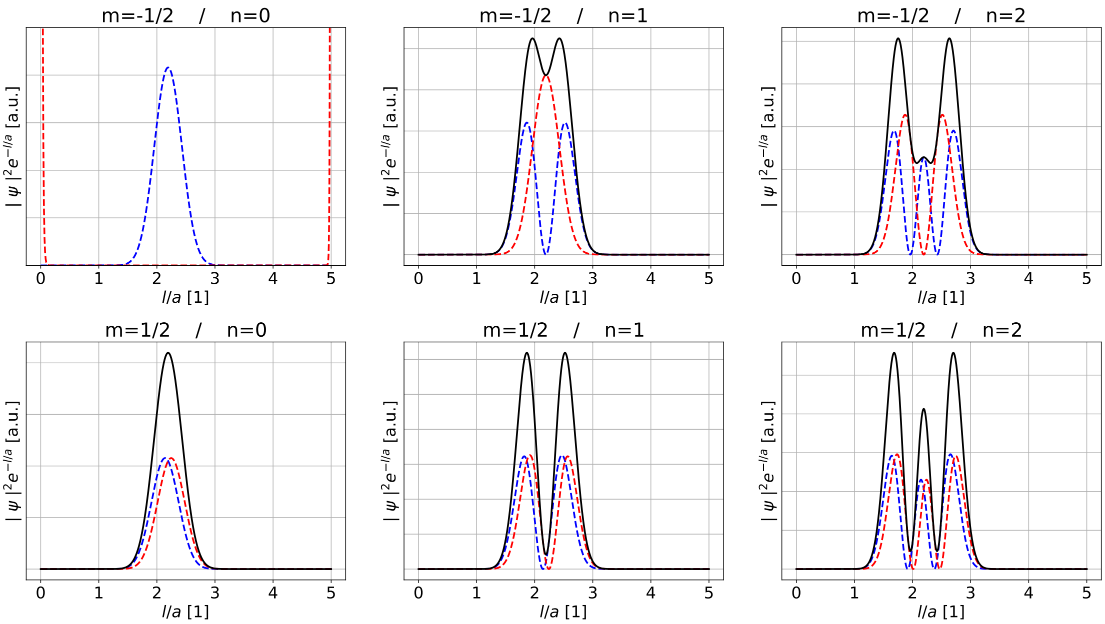

Figure 4.4: Numerically gained overall, radial probability densities $|\psi|^2 \exp(-l/a)$ (black, solid lines), as well as radial probability densities of the up component $|\psi^{\uparrow}|^2 \exp(-l/a)$ (blue, dashed lines) and down component $|\psi^{\downarrow}|^2 \exp(-l/a)$ (red, dashed lines) for the pseudosphere in a coaxial magnetic field and the angular quantum numbers $m = -1/2$ (upper panels) and $m = 1/2$ (lower panels). A lattice spacing of $\Delta l = 0.005a$ as well as a cut-off of $L = 5a$ were used.

Fig. 4.4 shows the four lowest lying Landau levels for the angular quantum numbers $m = -1/2$ (upper row) and $m = 1/2$ (lower row). We can see that the modulus squared of all the total wavefunctions are symmetric with respect to a certain point l/a. This reflects the symmetry of the effective potential $V(\tilde{l}) \propto \cosh\left(\tilde{l}/a\right)$, which enforces definite parity of all eigenspinor components. Most notably, we see that the number of nodes of up and down components of the spinor wavefunctions exactly agrees with our prediction from SUSY theory. For negative m, SUSY is unbroken and the up component always has one node more than the down component. The zeroth Landau level is fully spin polarized, however we may observe a divergence of the down component at the lattice borders. The origin of this numerical artifact has already been covered at the beginning of this chapter. For positive m, SUSY is broken and the number of nodes of up and down components of a single eigenstate is the same.

We can summarize this section by noticing that we confirmed the exact Dirac Landau level energies and found closed expressions for the eigenstates of a pseudosphere in an overall perpendicular magnetic field. In the second part, we successfully found asymptotic analytical expressions for the Landau level energies of a pseudosphere in a coaxial magnetic field which hold in the high field limit. Most notably, it turned out that the degeneracy of Landau levels in the angular quantum number m is not only lifted but angular branches with different sign of m also possess a different energy scaling in magnetic field. While the $m > 0$ branch shows the usual $\nu^{1/2}$ scaling, the $m < 0$ branch exhibits a very unconventional $\nu^{1/4}$ scaling. Clearly, the non-degeneracy of levels can be attributed to the fact that the projection of the magnetic field onto the surface normal is not constant along the arclength, yielding different effective field strengths. In case of the coaxial field, we also verified our results numerically. Wavefunctions show the same number of nodes as predicted by SUSY.

4.3. A general class of surfaces

When taking a look at the defining property of the cone and the pseudosphere, we find that the first mentioned fulfills $r'(l) \propto r^0(l)$, while the last mentioned fulfills $r'(l) \propto r^1(l)$. Based on this observation, a more general class of surfaces was introduced in [77], characterized by the defining property $r'(l) \propto r^\gamma(l)$, with $\gamma \in \mathbb{Z}$. In this thesis, we generalize this by allowing $\gamma \in \mathbb{R} \setminus \{0, 1, 2\}$. We exclude $\gamma \in \{0, 1, 2\}$ as these numbers lead to special integrals which do not align with the most general solution of the remaining cases. This is not a problem, since $\gamma = 1$ is the case of the pseudosphere which was extensively covered in the last section of this thesis and $\gamma = 0$ / $\gamma = 2$ correspond to the cone and the reciprocal cone, respectively, which have already been treated in [29, 77]. Writing the proportionality explicitly yields $r'(l) = \pm(r(l)/a)^\gamma$, with $a > 0$ and the sign $\pm$ chosen such that a physical solution exists. Separation of variables leads to the general solution

$$r(l) = \left(K \mp (\gamma - 1) a^{-\gamma} l\right)^{-\frac{1}{\gamma-1}} , \tag{4.55}$$

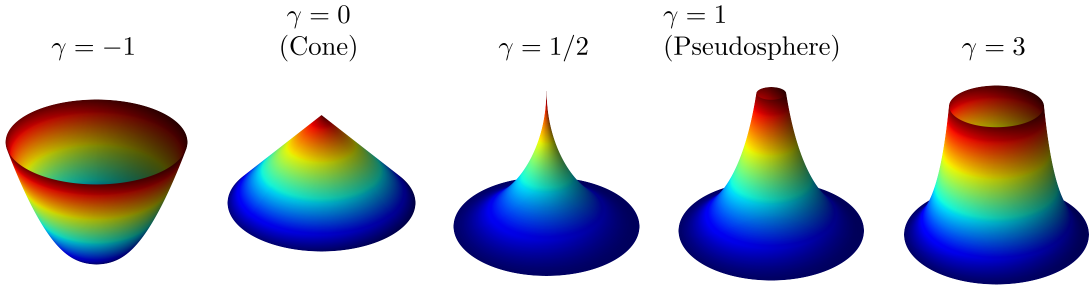

Figure 4.5: Representatives of the general class of surfaces. The colormap is exclusively used for better visualization and does not have any deeper meaning.

with $K \in \mathbb{R}$. The function $r(l)$ has to fulfill the property $|r'(l)| \leq 1$ in order to represent a surface which is immersible in ambient space. Further, we want the surface to have finite radius at $r(0) = a$ and to be parametrized in z-direction by positive l. This yields $K = a^{-(\gamma-1)}$. The particular value of γ fixes the sign and leads to the following cases:

- $\gamma > 1$: For the lower sign ($+$ in Eq. (4.55)), these surfaces have a maximal radius of a with $r(l)$ monotonously decreasing with $r \to 0$ at $l \to \infty$. They are not compact.
- $0 < \gamma < 1$: For the lower sign ($+$ in Eq. (4.55)), these surfaces have a maximal radius of a with $r(l)$ monotonously decreasing until $r = 0$ at $l = \frac{a}{1-\gamma}$. They are compact.
- $\gamma < 0$: For the upper sign ($-$ in Eq. (4.55)), these surfaces have a minimal radius of a with $r(l)$ monotonously increasing with $r \to 0$ at $l \to \infty$. They are not compact.

We can summarize that for all γ the relation

$$r(l) = a \left(1 \mp (\gamma - 1)\frac{l}{a}\right)^{-\frac{1}{\gamma-1}}, \tag{4.56}$$

with the respective sign holds. Note that after an appropriate shift of l we see that a surface with γ has a reciprocal surface with $\tilde{\gamma} = 2 - \gamma$ in the sense of the duality discussed at the very beginning of this chapter [29]. Interestingly, the pseudosphere is a fix point of this transformation. This perfectly matches with the observation made in the last section that m and ν always appear together in the Dirac equation, with only the product $m\nu$ being an independent parameter.

Fig. 4.5 shows a few representatives of the general class of surfaces, including the pseudosphere and the cone. In the following, we try to solve the Dirac equation for this general class of surfaces but focusing solely on the practically more relevant case of the overall coaxial magnetic field. The effective potential reads

$$V(l) = \frac{m}{a}\left(1 \mp (\gamma - 1)\frac{l}{a}\right)^{\frac{1}{\gamma-1}} + \frac{\nu}{a}\left(1 \mp (\gamma - 1)\frac{l}{a}\right)^{-\frac{1}{\gamma-1}}. \tag{4.57}$$

4.3.1. Zero energy states

We want to find possible zero energy states as a first step. It makes sense to perform the substitution

$$s(l) = a^{-(\gamma-1)} \mp (\gamma-1)a^{-\gamma} l\,, \tag{4.58}$$

so that

$$V(s) = m s^{\frac{1}{\gamma-1}} + \frac{\nu}{a^2} s^{-\frac{1}{\gamma-1}}\,. \tag{4.59}$$

As we have seen when discussing the general concepts, for $\nu > 0$ we have to choose $m < 0$ in order to ensure that the potential changes sign and the state is localized within the surface. Since the surface is compact for $0 < \gamma < 1$, the existence of the zero energy states is guaranteed as long as it is localized within the surface. For $\gamma > 1$ and $\gamma < 0$, the existence is linked to the behavior of the integral over the potential,

$$\begin{aligned}\int dl\, V(l) &= \mp \frac{1}{\gamma-1} a^{\gamma} \int ds \left(m s^{\frac{1}{\gamma-1}} + \frac{\nu}{a^2} s^{-\frac{1}{\gamma-1}} \right) \\ &= \mp a^{\gamma} \left(\frac{m}{\gamma} s^{\frac{\gamma}{\gamma-1}} + \frac{\nu}{a^2} \frac{1}{\gamma-2} s^{\frac{\gamma-2}{\gamma-1}} \right)\,,\end{aligned} \tag{4.60}$$

at $l \to \infty$. For $\gamma > 1$, the centrifugal term dominates in this limit. Since $m < 0$, the overall integral is negative and the spin-up solution $\Psi_0^{\uparrow}$ exists. Contrary to this, for $\gamma < 0$, the magnetic term dominates and gives an overall positive sign of the integral, leading to a valid spin-down solution $\Psi_0^{\downarrow}$. Overall, SUSY is unbroken for $m < 0$ and broken for $m > 0$.

4.3.2. Excited states - semiclassical way

We try to find the excited states employing the SWKB method. Again, it makes sense to perform the substitution

$$s(l) = a^{-(\gamma-1)} \mp (\gamma-1)a^{-\gamma} l\,, \tag{4.61}$$

so that

$$V^2(s) = m^2 s^{\frac{2}{\gamma-1}} + \frac{\nu^2}{a^4} s^{-\frac{2}{\gamma-1}} + \frac{2}{a^2} m\nu\,. \tag{4.62}$$

Given the energy $\epsilon^2 > 0$, we define the shifted energy $\tilde{\epsilon}^2 = \epsilon^2 - 2m\nu$. The classical turning points of the potential $V^2(s)$ are given by

$$s_{\pm}^{\frac{2}{\gamma-1}} = \frac{1}{2a^2 m^2} \left(\tilde{\epsilon}^2 \pm \sqrt{\tilde{\epsilon}^4 - 4m^2\nu^2} \right)\,.$$

We assume that both turning points are located within the surface. In this case, defining $l_{\pm} = l(s_{\pm})$, the action of a closed orbit is calculated by (see Appendix A.5 for a detailed solution of the integral)

$$
\begin{aligned}
S &= 2\hbar\left|\int_{l_-}^{l_+} dl\,\sqrt{\frac{\epsilon^2}{a^2}-V^2(l)}\right| \qquad (4.63)\\
&= 2\hbar|\gamma-1|^{-1}a^{\gamma}\int_{s_-}^{s_+} ds\,\sqrt{\frac{\epsilon^2}{a^2}-V^2(s)}\\
&= \frac{\hbar\pi}{8}a^{\gamma}|m|\left(s_+^{\frac{2}{\gamma-1}}-s_-^{\frac{2}{\gamma-1}}\right)^2\left(s_-^{\frac{2}{\gamma-1}}\right)^{-\frac{3}{2}+\frac{\gamma-1}{2}}\\
&\quad\times {}_2F_1\left(\frac{3}{2}-\frac{\gamma-1}{2},\frac{3}{2};3;1-\left(\frac{s_+}{s_-}\right)^{\frac{2}{\gamma-1}}\right)\\
&= \frac{\hbar\pi}{2^{1+\frac{\gamma}{2}}}|m|^{1-\gamma}(\tilde{\epsilon}^4-4m^2\nu^2)\\
&\quad\times\left(\tilde{\epsilon}^2-\sqrt{\tilde{\epsilon}^4-4m^2\nu^2}\right)^{-2+\frac{\gamma}{2}}\\
&\quad\times {}_2F_1\left(2-\frac{\gamma}{2},\frac{3}{2};3;1-\left(\frac{s_+}{s_-}\right)^{\frac{2}{\gamma-1}}\right)\\
&= \frac{\hbar\pi}{2^{1+\frac{\gamma}{2}}}|m|^{1-\gamma}f_1(\tilde{\epsilon},\nu)f_2(\tilde{\epsilon},\nu)f_3(\tilde{\epsilon},\nu)\,,
\end{aligned}
$$

where ${}_2F_1(a,b;c;z)$ is the *Gaussian hypergeometric function* [98]. For convenience, we abbreviated the remaining factor in the first line of the final result as $f_1(\tilde{\epsilon},\nu)$, the term in the second line as $f_2(\tilde{\epsilon},\nu)$ and the one in the third line as $f_3(\tilde{\epsilon},\nu)$. We need to invert the action as a function of energy to find the spectrum. As in case of the pseudosphere, this cannot be done exactly due to its complicated structure. We resort to the same strategy and examine the behavior in presence of strong magnetic fields, only keeping leading order terms in ν and neglecting subleading ones. The relation between κ and ϵ has to be some power function because there are no transcendental prefactors in the Dirac equation, so that in the strong field limit $\tilde{\epsilon}^2 = k\nu^{\kappa}$ for some $k>0$ and $\kappa\in\mathbb{R}$. As in the last section, we have to distinguish (at least) three possible cases, $\kappa<1$ ($\tilde{\epsilon}^2$ grows slower than ν), $\kappa=1$ ($\tilde{\epsilon}^2$ grows as fast as ν) and $\kappa>1$ ($\tilde{\epsilon}^2$ grows faster than ν). Before starting, we can directly see that the case $\kappa<0$ cannot hold true, since the radicand would become negative for high ν.

Case 1: $\kappa > 1$

We start with the case $\kappa>1$ and have a look at the first term,

$$
\begin{aligned}
f_1(\tilde{\epsilon},\nu) &= k^2\nu^{2\kappa}\left(1-\frac{4m^2}{k^2}\nu^{2-2\kappa}\right) \qquad (4.64)\\
&\approx k^2\nu^{2\kappa}\,.
\end{aligned}
$$

The second term can be approximated by

$$
\begin{aligned}
f_2(\tilde{\epsilon},\nu) &= \left[k\nu^\kappa - k\nu^\kappa\sqrt{1-\frac{4m^2\nu^2}{k^2\nu^{2\kappa}}}\right]^{-2+\frac{\gamma}{2}} \\
&\approx \left[k\nu^\kappa - k\nu^\kappa\left(1-\frac{1}{2}\frac{4m^2\nu^2}{k^2\nu^{2\kappa}}\right)\right]^{-2+\frac{\gamma}{2}} \\
&= \left(\frac{2m^2}{k}\nu^{2-\kappa}\right)^{-2+\frac{\gamma}{2}} .
\end{aligned} \tag{4.65}
$$

For the third term, we first of all have to approximate the ratio

$$
\begin{aligned}
\left(\frac{s_+}{s_-}\right)^{\frac{2}{\gamma-1}} &= \frac{\tilde{\epsilon}^2+\sqrt{\tilde{\epsilon}^4-4m^2\nu^2}}{\tilde{\epsilon}^2-\sqrt{\tilde{\epsilon}^4-4m^2\nu^2}} \\
&= \frac{1+\sqrt{1-\frac{4m^2\nu^2}{\tilde{\epsilon}^4}}}{1-\sqrt{1-\frac{4m^2\nu^2}{\tilde{\epsilon}^4}}} \\
&\approx \frac{1+1}{1-\left(1-\frac{1}{2}\frac{4m^2\nu^2}{\tilde{\epsilon}^4}\right)} \\
&= \frac{\tilde{\epsilon}^4}{m^2\nu^2} = \frac{k^2}{m^2}\nu^{2\kappa-2} .
\end{aligned} \tag{4.66}
$$

This directly gives us an asymptotic approximation of $f_3(\tilde{\epsilon},\nu)$,

$$
\begin{aligned}
f_3(\tilde{\epsilon},\nu) &\approx {}_2F_1\left(2-\frac{\gamma}{2},\frac{3}{2};3;-\frac{k^2}{m^2}\nu^{2\kappa-2}\right) \\
&\overset{[98]}{\approx} +\Theta(\gamma-1)\frac{\Gamma(3)\Gamma\left(\frac{\gamma-1}{2}\right)}{\Gamma\left(\frac{3}{2}\right)\Gamma\left(1+\frac{\gamma}{2}\right)}\left(\frac{k^2}{m^2}\nu^{2\kappa-2}\right)^{-2+\frac{\gamma}{2}} \\
&\quad +\Theta(1-\gamma)\frac{\Gamma(3)\Gamma\left(\frac{1-\gamma}{2}\right)}{\Gamma\left(\frac{3}{2}\right)\Gamma\left(2-\frac{\gamma}{2}\right)}\left(\frac{k^2}{m^2}\nu^{2\kappa-2}\right)^{-\frac{3}{2}} .
\end{aligned} \tag{4.67}
$$

The action has to be constant. We therefore require the overall exponent of ν to vanish. For $\gamma > 1$, this yields the constraint

$$
\begin{aligned}
& 2\kappa + (2-\kappa)\left(-2+\frac{\gamma}{2}\right) + (2\kappa-2)\left(-2+\frac{\gamma}{2}\right) = 0 \\
\Leftrightarrow\ & 2\kappa + \kappa\left(-2+\frac{\gamma}{2}\right) = 0 \\
\Leftrightarrow\ & \kappa = 0 \vee \gamma = 0 .
\end{aligned} \tag{4.68}
$$

Both possible constraints contradict our assumptions ($\kappa > 1$ and $\gamma > 1$). Therefore, this ansatz is not valid for surfaces with $\gamma > 1$. For $\gamma < 1$, we have the constraint

$$
\begin{aligned}
& 2\kappa + (2-\kappa)\left(-2+\frac{\gamma}{2}\right) + (2\kappa-2)\left(-\frac{3}{2}\right) = 0 \qquad (4.69)\\
\Leftrightarrow\quad & \kappa + \gamma - \frac{\kappa\gamma}{2} - 1 = 0\\
\Leftrightarrow\quad & \kappa = \frac{2-2\gamma}{2-\gamma}\,.
\end{aligned}
$$

$\kappa > 1$ by assumption, so that this ansatz is only consistent for $\gamma < 0$. Overall, we see that for $\gamma < 0$, the dominant scaling is given by

$$\tilde{\epsilon}^2 = k\nu^{\frac{2-2\gamma}{2-\gamma}}\,. \qquad (4.70)$$

Inserting κ into the original ansatz, we easily find

$$k = \left(2\sqrt{\pi}\frac{\Gamma\left(2-\frac{\gamma}{2}\right)}{\Gamma\left(\frac{1}{2}-\frac{\gamma}{2}\right)}\left(2n+\Theta(m)\right)\right)^{\frac{2}{2-\gamma}}\,, \qquad (4.71)$$

where we used the unbroken SUSY quantization condition for $m < 0$ and the broken SUSY quantization condition for $m > 0$. The overall energy is then given by

$$
\begin{aligned}
\epsilon &= \pm\sqrt{\tilde{\epsilon}^2 + 2m\nu} \qquad (4.72)\\
&\approx \pm\sqrt{k\nu^{\frac{2-2\gamma}{2-\gamma}} + 2m\nu}\\
&\approx \pm\sqrt{k\nu^{\frac{2-2\gamma}{2-\gamma}}}\\
&\approx \pm k^{\frac{1}{2}}\nu^{\frac{1-\gamma}{2-\gamma}}\,.
\end{aligned}
$$

Case 2: $\kappa = 1$

Let us proceed with the case of $\kappa = 1$. The first term is very decisive in this case since

$$f_1(\tilde{\epsilon},\nu) = (k^2 - 4m^2)\nu^2 \qquad (4.73)$$

has a zero for $k = 2|m|$. Let us assume for the moment that k does not have this value. This obviously only makes sense if $k > 2|m|$. Then, we can approximate

$$f_2(\tilde{\epsilon},\nu) \approx \left[\left(1-\sqrt{1-\frac{4m^2}{k^2}}\right)k\nu\right]^{-2+\frac{\gamma}{2}}\,. \qquad (4.74)$$

Again, we need the ratio s_+/s_- for the last term,

$$
\begin{aligned}
\left(\frac{s_+}{s_-}\right)^{\frac{2}{\gamma-1}} &= \frac{\tilde{\epsilon}^2 + \sqrt{\tilde{\epsilon}^4 - 4m^2\nu^2}}{\tilde{\epsilon}^2 - \sqrt{\tilde{\epsilon}^4 - 4m^2\nu^2}} \qquad (4.75)\\
&= \frac{1+\sqrt{1-\frac{4m^2}{k^2}}}{1-\sqrt{1-\frac{4m^2}{k^2}}}\,.
\end{aligned}
$$

Since $f_3(\tilde{\epsilon},\nu)$ will be independent of ν, we can already balance the dominant powers,

$$2-2+\frac{\gamma}{2}=0 \Leftrightarrow \gamma=0\,. \tag{4.76}$$

This requires $\gamma=0$ which is excluded from the treatment here. Let us now assume $k=2|m|$. Then the action will vanish to leading order and we have to take the next to leading order into account, at least for the first term. This can be done by making the ansatz $\tilde{\epsilon}^2=2|m|\nu\left(1+\tilde{k}\nu^{\delta}\right)$, with $\tilde{k}>0$ and $\delta<0$, yielding

$$\begin{aligned} f_1(\tilde{\epsilon},\nu) &\approx \left[2|m|\nu\left(1+\tilde{k}\nu^{\delta}\right)\right]^2-4m^2\nu^2 \\ &\approx 4m^2\nu^2\left(1+2\tilde{k}\nu^{\delta}+\tilde{k}^2\nu^{2\delta}\right)-4m^2\nu^2 \\ &\approx 8m^2\tilde{k}\nu^{2+\delta}\,. \end{aligned} \tag{4.77}$$

The second term is simply given by

$$f_2(\tilde{\epsilon},\nu)\approx(2|m|\nu)^{-2+\frac{\gamma}{2}}\,, \tag{4.78}$$

whereas the third one reads

$$f_3(\tilde{\epsilon},\nu)\approx {}_2F_1\left(2-\frac{\gamma}{2},\frac{3}{2};3;0\right)=1\,. \tag{4.79}$$

Balancing of the dominant terms is straightforward in this case,

$$2+\delta-2+\frac{\gamma}{2}=0 \Leftrightarrow \delta=-\frac{\gamma}{2}\,. \tag{4.80}$$

We assumed $\delta<0$, so that this ansatz is only valid for $\gamma>0$. Inserting δ into the original ansatz yields

$$\tilde{k}=|m|^{-1+\frac{\gamma}{2}}\left(2n+\Theta(m)\right)\,, \tag{4.81}$$

where we used the unbroken SUSY quantization condition for $m<0$ and the broken SUSY quantization condition for $m>0$. The overall energy finally reads

$$\begin{aligned} \epsilon &= \pm\sqrt{2m\nu+2|m|\nu+2|m|^{\frac{\gamma}{2}}\left(2n+\Theta(m)\right)\nu^{\frac{2-\gamma}{2}}} \\ &= \pm\sqrt{4m\nu\Theta(m)+2|m|^{\frac{\gamma}{2}}\left(2n+\Theta(m)\right)\nu^{\frac{2-\gamma}{2}}}\,. \end{aligned} \tag{4.82}$$

Final results

To conclude the calculation, we have to reconsider our assumption. Our main motivation was to find the Landau level scaling for the case when the classical orbits are fully inside the surface, i.e. the particle does not feel the boundary. This is often associated with a high magnetic field, so that the magnetic length l_B becomes much smaller than the system dimensions. However, one must be careful with this in some cases of our general class of surfaces. When inspecting the effective potential, $V(l)=m/r(l)+\nu r(l)/a^2$, we see that for monotonously falling $r(l)$ the wavefunctions are pushed towards the boundary for rising angular quantum number m and inside the surface for rising magnetic field ν. Vice versa, if $r(l)$ is monotonously increasing, the wavefunctions are pushed towards the boundary for rising ν and inside the surface for rising m. As discussed in the introduction of this section, this is exactly the case for $\gamma < 0$. We conclude that the interesting limit to look at for these surfaces is $m \to \infty$, rather than $\nu \to \infty$. Luckily, we do not have to repeat all of the calculation above. Looking at Eq. (4.62), we see that the calculation for the limit of large m is the same as the one for the limit of large ν upon interchanging m and ν and simultaneously replacing γ by $2-\gamma$ in the final energy formula. Interestingly, this directly leads to the same energy formula as for surfaces with $\gamma > 0$ (this is not a coincidence but reflects the duality of these surfaces, as presented in [29]), so that our final energy formula for all γ reads

$$\epsilon \;=\; \pm\sqrt{4m\nu\Theta(m) + 2|m|^{\frac{\gamma}{2}}\left(2n + \Theta(m)\right)\nu^{\frac{2-\gamma}{2}}}\,, \tag{4.83}$$

where we have to stress that it is only a good approximation formula in the correct regime, large ν for surfaces with $\gamma > 0$ and large m for surfaces with $\gamma < 0$.

As for the pseudosphere, degeneracy in the angular quantum number m is lifted for excited Landau level energies and, depending on the sign of m, we have two qualitatively different spectral branches. For $m > 0$, the first two terms under the radicand add up and give the dominant contribution for large magnetic fields, yielding an overall scaling of $\epsilon \propto \nu^{1/2}$, whereas for $m < 0$, they cancel and the next to leading order term becomes dominant, yielding a scaling of $\epsilon \propto \nu^{(2-\gamma)/4}$. This is exactly the conjecture formulated in [77]. We therefore successfully proved it. Note that Eq. (4.83) also holds for the pseudosphere ($\gamma = 1$).

4.3.3. Excited states - numerical way and comparison

We want to perform numerical calculations to validate our analytically gained spectrum as well as to take a look at the wavefunctions of the Landau levels. We do this exemplarily for two surfaces, one with $\gamma = 3 > 1$ and one with $\gamma = -1 < 1$.

Fig. 4.6 shows the first 20 (positive) Landau level energies for a surface with $\gamma = 3$. The left panels show the results for the angular quantum number of $m = -19/2$, while the right ones show them for $m = 19/2$. The upper panels show a usual linear plot, while the lower ones have a double logarithmic scale in order to verify the semiclassically expected scaling exponents of the energies with magnetic field. The black crosses mark numerically gained solutions, while the solid lines represent analytical solutions in case of the linear plots. In case of the double logarithmic plots they represent a linear fitting to the five black crosses at strongest magnetic field. The mean value of the slope of these lines is given in the graphs, representing the scaling exponent of the magnetic field in the energy.

Again, the agreement is good for strong magnetic fields ν. This is for the same reason as in case of the pseudosphere, $l_B < a$ in this regime, and orbits are localized far away from the boundary of the surface, fulfilling our assumption for using SWKB very well.

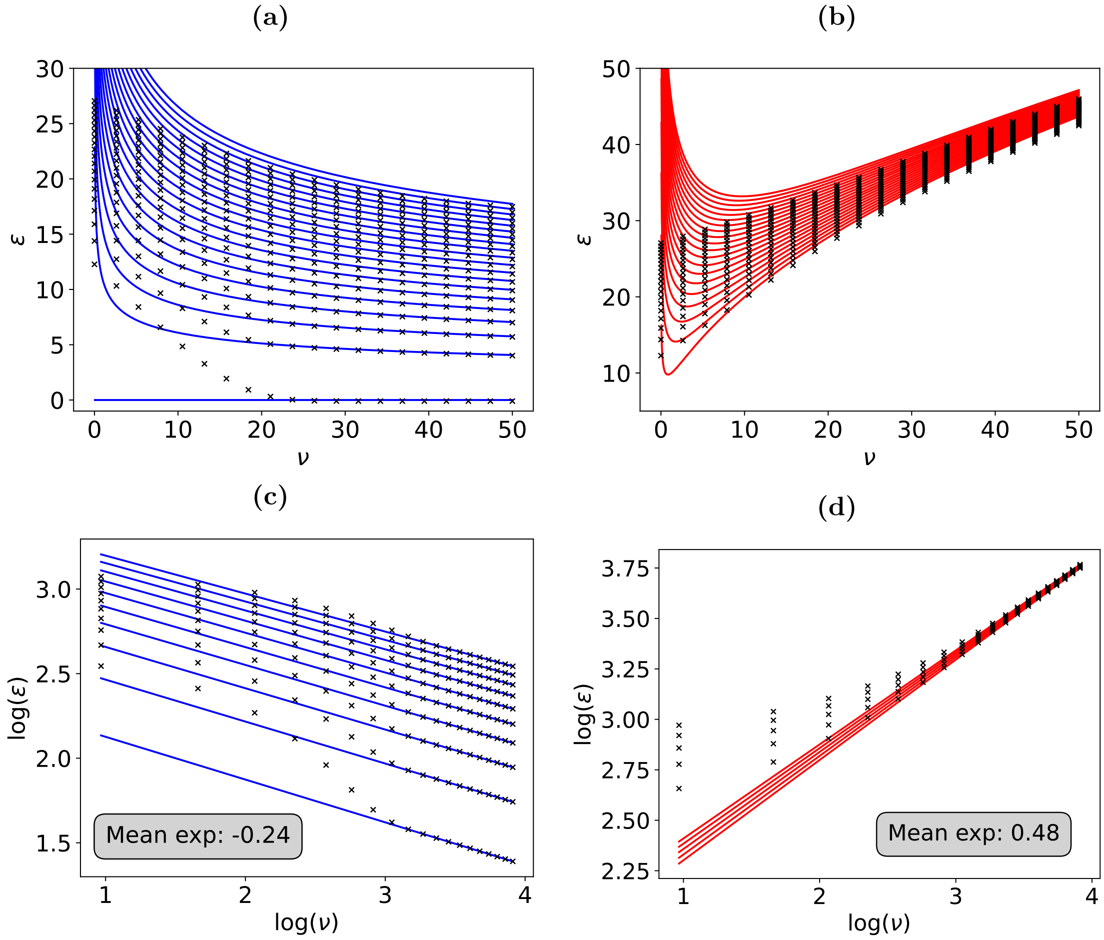

Figure 4.6: Lowest positive Dirac Landau level energies as a function of magnetic field ν of a surface with $\gamma = 3$ in a coaxial magnetic field for $m = -19/2$ ((a) and (c)) as well as for $m = 19/2$ ((b) and (d)). The upper panels show linear plots, while the lower ones show double logarithmic plots. Black crosses mark numerical solutions of the radial Dirac equation (Eq. (4.2)). A lattice spacing of $\Delta l = 0.0025a$ as well as a cut-off of $L = 5a$ were used. Solid lines in the linear plots represent analytical solutions from SWKB approximation (Eq. (4.83)). Solid lines in double logarithmic plots represent linear fitting curves to the numerical solutions at the five highest magnetic field strengths. Each linear fitting curve belongs to one main quantum number n. The slopes of these curves yield the scaling exponent κ in $\epsilon \propto \nu^{\kappa}$. The mean slope is given in each double logarithmic plot.

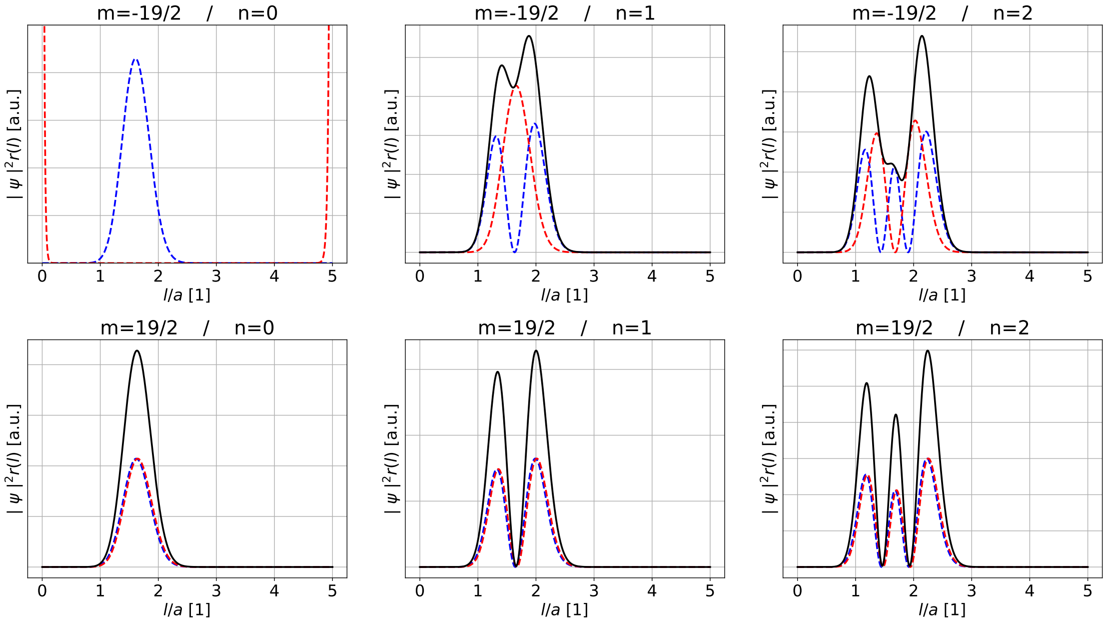

Figure 4.7: Numerically gained overall, radial probability densities $|\psi|^2 r(l)$ (black, solid lines), as well as radial probability densities of the up component $|\psi^{\uparrow}|^2 r(l)$ (blue, dashed lines) and down component $|\psi^{\downarrow}|^2 r(l)$ (red, dashed lines) for a surface with $\gamma = 3$, as well as angular quantum numbers $m = -19/2$ (upper panels) and $m = 19/2$ (lower panels). A lattice spacing of $\Delta l = 0.0025a$ as well as a cut-off of $L = 5a$ were used.

The agreement is best for small energies (low main quantum numbers n), as in case of the pseudosphere, with underestimation of eigenenergies in the higher energy regime. We can explain this finding with the same argument, the strong non-linearity of the potential well when moving away from the potential minimum.

The scaling exponents -0.24 for $m = -19/2$ and 0.48 for $m = 19/2$ match very well with the SWKB predictions of $-1/4$ and $1/2$, respectively.

Fig. 4.7 shows the three lowest lying Landau levels for the angular quantum numbers $m = -19/2$ (upper row) and $m = 19/2$ (lower row). Again, we observe that the number of nodes of up and down components of the spinor wavefunctions exactly agrees with our prediction from SUSY theory. For $m = -19/2$, SUSY is unbroken and the up component always has one node more than the down component. The zeroth Landau level is again fully spin polarized but shows the same numerical artifact as in case of the pseudosphere. For $m = 19/2$, SUSY is broken and the number of nodes of up and down component of a single eigenstate is the same.

Let us continue with the results for a surface with $\gamma = -1$. Fig. 4.8 depicts the lowest (positive) Landau level energies. The left panels show the results for the angular quantum number of $m = -199/2$, while the right ones show them for $m = 199/2$. The upper panels show a usual linear plot, while the lower ones have a double logarithmic scale in order to verify the semiclassically expected scaling exponents of the energies

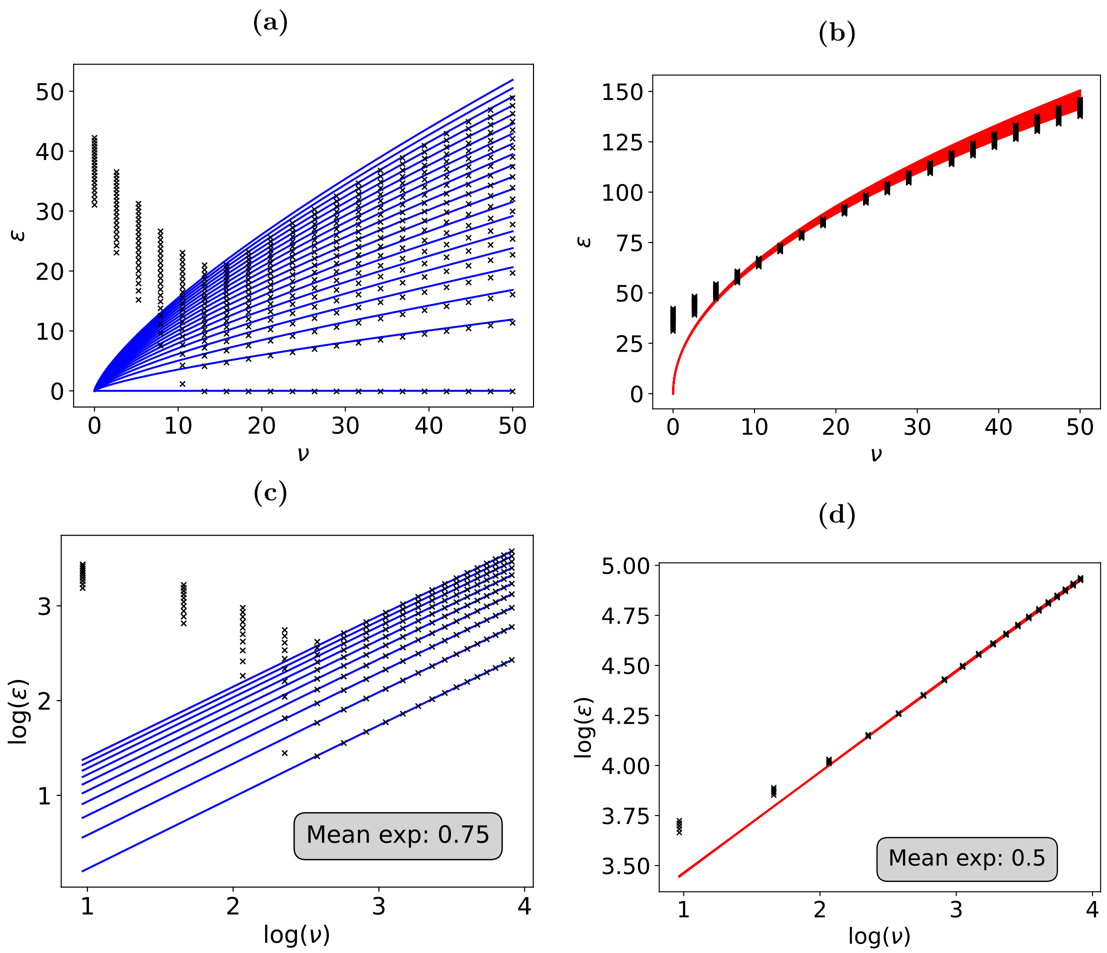

Figure 4.8: Lowest positive Dirac Landau level energies as a function of magnetic field ν of a surface with $\gamma = -1$ in a coaxial magnetic field for $m = -199/2$ ((a) and (c)), as well as for $m = 199/2$ ((b) and (d)). The upper panels show linear plots, while the lower ones show double logarithmic plots. Black crosses mark numerical solutions of the radial Dirac equation (Eq. (4.2)). A lattice spacing of $\Delta l = 0.0025a$ as well as a cut-off of $L = 5a$ were used. Solid lines in the linear plots represent analytical solutions from SWKB approximation (Eq. (4.83)). Solid lines in double logarithmic plots represent linear fitting curves to the numerical solutions at the five highest magnetic field strengths. Each linear fitting curve belongs to one main quantum number n. The slope of these curves yield the scaling exponent κ in $\epsilon \propto \nu^{\kappa}$. The mean slope is given in each double logarithmic plot.

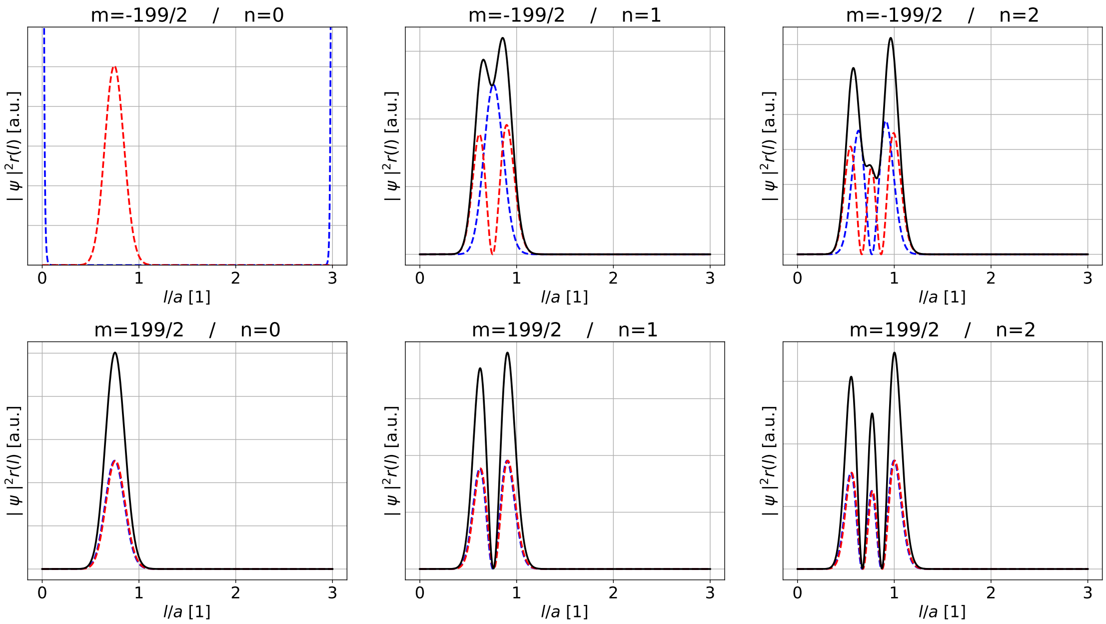

Figure 4.9: Numerically gained overall, radial probability densities $|\psi|^2 r(l)$ (black, solid lines), as well as radial probability densities of the up component $|\psi^{\uparrow}|^2 r(l)$ (blue, dashed lines) and down component $|\psi^{\downarrow}|^2 r(l)$ (red, dashed lines) for a surface with $\gamma = -1$ as well as angular quantum numbers $m = -199/2$ (upper panels) and $m = 199/2$ (lower panels). A lattice spacing of $\Delta l = 0.0025a$ as well as a cut-off of $L = 5a$ were used.

with magnetic field. The black crosses mark numerically gained solutions, while the solid lines represent analytical solutions (Eq. (4.83)) in case of the linear plots. In case of the double logarithmic plots they represent a linear fitting to the five black crosses at strongest magnetic field. The mean value of the slope of these lines is given in the graphs, representing the scaling exponent of the magnetic field in the energy.

We can clearly see that Eq. (4.83) gives good results. This verifies our previous argument about the choice of the correct asymptotic limit. In case of negative m, the matching is better for smaller main quantum numbers n. For higher n, the eigenenergies are overestimated by SWKB. For positive m, the energies lay much closer to each other. This can be explained with the spectral formula (Eq. (4.83)), where the factor $2m\nu$, independent of n, is dominant over the n dependent one, which is only subleading.

The scaling exponents 0.75 for $m = -199/2$ and 0.5 for $m = 199/2$ match perfectly with the SWKB predictions of $3/4$ and $1/2$, respectively.

Fig. 4.9 shows the three lowest lying Landau levels for the angular quantum numbers $m = -199/2$ (upper row) and $m = 199/2$ (lower row). Again, we observe that the number of nodes of up and down components of the spinor wavefunctions exactly agrees with our prediction from SUSY theory. For $m = -199/2$, SUSY is unbroken and the down component always has one node more than the up component (note that the roles of up and down component are exactly reversed compared to the pseudosphere or $\gamma = 3$). The zeroth Landau level is again fully spin polarized but shows the same numerical artifact as in cases of the pseudosphere and $\gamma = 3$. For $m = 199/2$, SUSY is broken and the number of nodes of up and down component of a single eigenstate is the same.

We can summarize this section by noticing that we could successfully proof a conjecture, made in [77], about the Dirac Landau level scaling for surfaces of the general class using the SWKB method. We confirmed that the excited Landau level energies are not degenerate in the angular quantum number m anymore and the spectrum decomposes into two branches, depending on the sign of m. For $m > 0$, the scaling ($\epsilon \propto \nu^{1/2}$) is independent of the geometrical parameter γ, whereas for $m < 0$, it strongly depends on it ($\epsilon \propto \nu^{(2-\gamma)/4}$). Again, we can explain this unconventional behavior qualitatively by the non-homogeneous orthogonal projection of the magnetic field onto the surface normal. We verified our results numerically which also revealed the perfect agreement of the eigenstate structure with the prediction we made using SUSY.

4.4. Persistent currents and magnetic dipole moment

We want to complement our analysis of the spectrum by examining how the structure of the eigenstates influences the local current density and therefore also the magnetic dipole moment. The current density in $\vec{\partial}_l$ direction vanishes because as explained at the beginning of this chapter, we can always choose one spin component to be purely real, while the remaining one is purely imaginary. Therefore, the product of one complex-conjugated component with the remaining one is always purely imaginary, so that (recall Eq. (3.36) for the current density)

$$\begin{aligned} j^1 &= -ev_F\psi^\dagger\sigma_x\psi \\ &= -\frac{ev_F}{r(l)}\left(\Psi^{\uparrow *}\Psi^{\downarrow} + \Psi^{\uparrow}\Psi^{\downarrow *}\right) \\ &= -\frac{ev_F}{2r(l)}\mathrm{Re}\left\{\Psi^{\uparrow *}\Psi^{\downarrow}\right\} \\ &= 0\,. \end{aligned} \tag{4.84}$$

Using the same arguments, we find for the current density in $\vec{\partial}_\phi$ direction,

$$\begin{aligned} j^2 &= -ev_F\psi^\dagger\sigma_y\psi \\ &= -\frac{ev_F}{r(l)}\left(i\Psi^{\downarrow *}\Psi^{\uparrow} - i\Psi^{\uparrow *}\Psi^{\downarrow}\right) \\ &= -\frac{ev_F}{2r(l)}\mathrm{Im}\left\{\Psi^{\uparrow *}\Psi^{\downarrow}\right\}\,. \end{aligned} \tag{4.85}$$

Basic electrodynamics gives us a formula for the magnetic dipole moment (in z-direction), which can be simplified using Hellman-Feynman theorem and the original expression for the current density,

$$
\begin{aligned}
m_z &= \frac{1}{2}\int_\Sigma dV \, \left(\vec{r}^{3D} \times \vec{j}^{3D}\right)_z &(4.86)\\
&= \frac{1}{2}\int_\Sigma dV \, j^2 \left(\vec{r}^{3D} \times \frac{\vec{\partial_\phi}^{3D}}{\left\|\vec{\partial_\phi}^{3D}\right\|}\right)_z \\
&= \frac{1}{2}\int_\Sigma dV \, j^2 r(l) \\
&= -\frac{ev_F}{2}\int_\Sigma dV \, \psi^\dagger \sigma_y r(l)\psi \\
&= -\frac{ev_F}{2}\langle\psi|\sigma_y r(l)|\psi\rangle \\
&= -\left\langle \psi \left| \frac{\partial \hat{H}}{\partial B} \right| \psi \right\rangle \\
&= -\frac{\partial E}{\partial B}\,.
\end{aligned}
$$

Note that this is indeed consistent with the thermodynamical definition of magnetic dipole moment of a single occupied state. Deeper insight can be gained when rewriting the current density in terms of the two spinor components,

$$
\begin{aligned}
m_z &= \frac{1}{2}\int_\Sigma dV \, j^2 r(l) &(4.87)\\
&= -\frac{ev_F}{4}\int_\Sigma dV \, \mathrm{Im}\left\{\Psi^{\uparrow *}\Psi^{\downarrow}\right\} \\
&= -\frac{\pi e v_F}{2}\int dl \, r(l)\mathrm{Im}\left\{\Psi^{\uparrow *}\Psi^{\downarrow}\right\}\,.
\end{aligned}
$$

Because the product of the spinor components is purely imaginary, we can interpret the magnetic dipole moment as a measure of the correlation between the up and down components. Both oscillate within the same region, where one may have one node more than the other. Correlation and therefore magnetic dipole moment is high, when both components oscillate in phase, whereas it is low when they are anti-phase.

A very good example to show this is the reciprocal cone (which is part of the general class of surfaces with $\gamma = 2$). As found in [29] and also confirmed by our SWKB results (see Eq. (4.83)), energy eigenvalues of one spectral branch do not depend on the magnetic field ν at all in the limit of strong fields ($\nu >> 1$). Fig. 4.10 shows the azimuthal current density of the Dirac Landau level state with $n = 3$ and $m = -5/2$, as well as $m = 5/2$ for a reciprocal cone with opening angle of $\theta = 70°$ of the original cone. It can clearly be seen that for $m > 0$, the current only flows in one direction, yielding a large magnetic dipole moment. Contrary to this, for $m < 0$, the current flows in both directions, depending on the arclength coordinate l. This suggest a highly attenuated magnetic dipole moment. Eq. (4.86) even suggests that a vanishing dependency of energy on the magnetic field

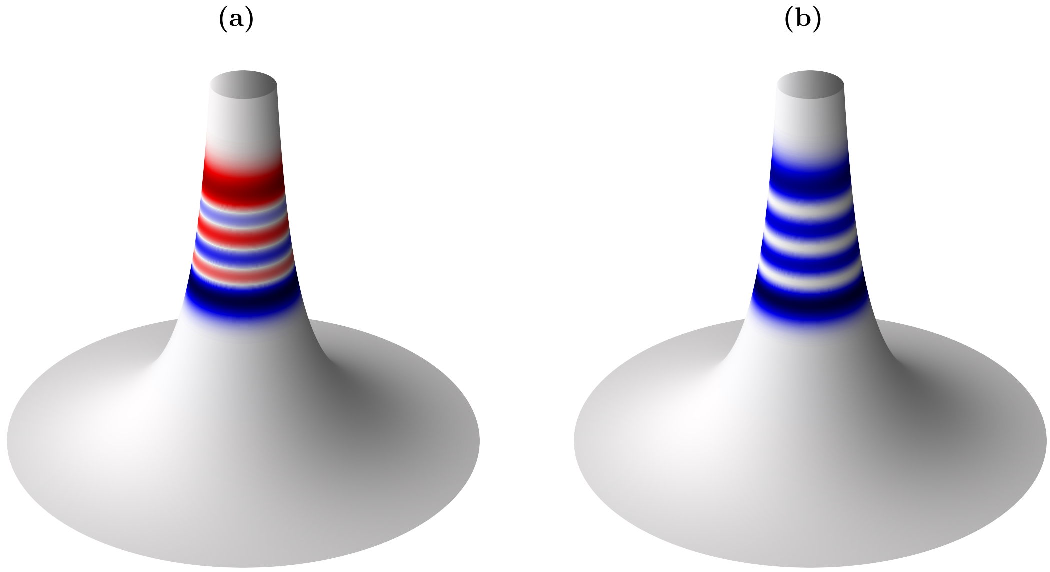

Figure 4.10: Azimuthal current density of the Dirac Landau level state with $n = 3$ and $m = -5/2$ ((a)) and $m = 5/2$ ((b)) for a reciprocal cone (surface of the general class of surfaces with $\gamma = 2$) with opening angle of $\theta = 70°$ of the original cone. Current flows clockwise if color is blue and counter clockwise if color is red. Stronger color means higher magnitude of current. The current has analytically been calculated using Eq. (4.85) and wavefunctions obtained in [29].

implies totally vanishing dipole moment. This is indeed confirmed explicitly to be the case in [29] by solving Eq. (4.87).

5. Magnetization of Dirac quasiparticles on curved surfaces

One of the experimental possibilities to probe Dirac Landau levels is to directly measure its impact on the magnetic field. This is captured by the magnetic susceptibility χ. We especially want to study how geometry affects its properties and therefore choose three exemplary surfaces, namely the pseudosphere, a cone with opening angle $\theta = \pi/2$ and an half sphere, which we just call a sphere for simplicity in the following. The key to understanding how χ looks like in case of curved surfaces is to have a full understanding of the spectrum. We partially gained this for the pseudosphere in the previous chapter, however only in the high field limit. In the first section of this chapter, we will summarize known results in this regime for all three surfaces and then also study the opposite regime, the weak field limit. We perform analytical calculations without assuming a specific geometry, whenever possible. After the analytical discussion, a numerical calculation of the full spectrum in the vicinity of zero energy is presented. The second section revises thermodynamical basics which are necessary to compute the susceptibility, introduces a very elegant method to compute the grand canonical potential analytically, featuring Poisson summation as well as the bilateral Laplace transform, and further summarizes the main characteristics of χ for flat Dirac systems. After this preparatory work, a fully numerical calculation of χ for all three surfaces is performed. We find that dHvA oscillations are different for pseudosphere, cone and sphere. Finally, we present an analytical calculation of this effect in case of the pseudosphere, which is highly non-trivial due to the non-degenerate nature of its Landau levels. As always, we assume positive magnetic field, $\nu > 0$, throughout this chapter. The case of negative field can be trivially derived from this due to chiral symmetry. Fig. 5.1 shows the three surfaces treated in this chapter.

5.1. Discussion of the spectrum

The spectrum of the Hamiltonian is the key to understand magnetization properties of the whole system. We therefore try to understand this in the first step and present asymptotic eigenenergies in the strong field regime ($l_B << a$) of the massless Dirac Hamiltonian with coaxial magnetic field on our three exemplary surfaces, the pseudosphere, the cone, as well as the sphere. We also examine how the spectrum looks in the opposite limit, the weak field regime ($l_B >> a$). In order to get a detailed overview of the spectrum within the full range of magnetic fields, we also take a look at numerical solutions. As the spectrum is symmetric with respect to $E = 0$ due to chiral symmetry, we focus on positive energy solutions in the following.

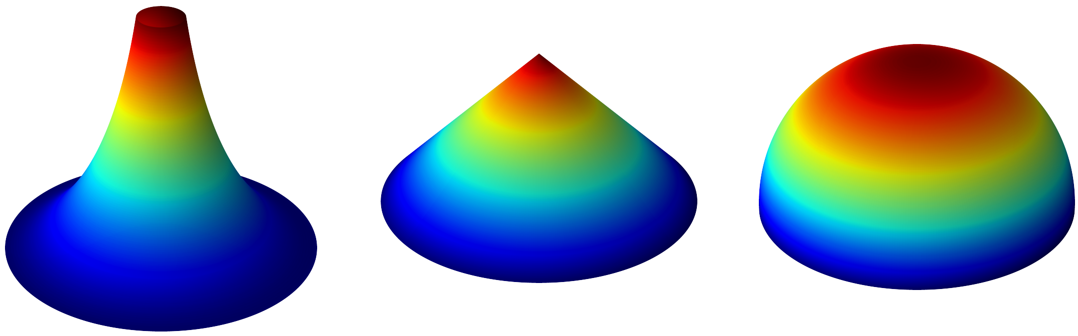

Figure 5.1: The three surfaces treated in this chapter, the pseudosphere ((a)), a cone with opening angle $\theta = \pi/2$ ((b)) and a sphere ((c)). The colormap is exclusively used for better visualization and does not have any deeper meaning.

5.1.1. Strong magnetic field

In case of the pseudosphere, we work with the solutions found using the asymptotic formula for the *DCHE* since it is more accurate. For negative angular quantum numbers, we derived it in Chapter 4 (Eq. (4.40)). For convenience, we recall

$$\epsilon = \sqrt{4n\sqrt{-m\nu} + \frac{1}{2}n^2 - 1}, \text{for}\, m < 0,\ n > 0\,. \tag{5.1}$$

As explained previously, the zeroth Landau level is not captured correctly by this formula but we know it exists. For positive angular quantum numbers, the corresponding solution can be found in [27],

$$\epsilon = \sqrt{4m\nu + (4n+2)\sqrt{m\nu} + \frac{1}{2}n^2 + \frac{1}{2}n - 2}, \text{for}\, m > 0,\ n \geq 0. \tag{5.2}$$

None of the solutions, except for the zero energy states, show degeneracy. The energy of the angular branch with $m < 0$ asymptotically scales with $\propto \nu^{1/4}$, while the branch with $m > 0$ scales with $\propto \nu^{1/2}$. Interestingly, for large ν and $m > 0$, the main level structure is determined by the angular quantum number m, rather than the main quantum number n, since the first term under the root scales with ν, while the second one only scales with $\nu^{1/2}$. Henceforth, increasing m by one changes the energy much more than increasing n by one.

The exact solutions for the cone (with atomic boundary conditions) were obtained in [77]. The eigenenergies read

$$\epsilon = \sqrt{4n\nu \sin\left(\frac{\theta}{2}\right)}, \text{for}\, m < 0,\ n \geq 0\,, \tag{5.3}$$

and

$$\epsilon = \sqrt{4\nu \sin\left(\frac{\theta}{2}\right)\left(n + \frac{1}{2} + \frac{m}{\sin\left(\frac{\theta}{2}\right)}\right)}, \text{for}\, m > 0,\, n \geq 0\,, \tag{5.4}$$

where θ is the opening angle of the cone. Note, that for $m < 0$, the energies are degenerate in m. In the limit of the flat plane ($\theta = \pi$), the formula for $m > 0$ simplifies to $\epsilon = \sqrt{4\nu(n + 1/2 + m)}$ and since $m \in \mathbb{Z} + 1/2$, the levels have the same energy as those of the $m < 0$ branch. It is an interesting matter of fact that this is only possible because the contribution of 1/2 from the *Spin-1/2 Berry phase* adds up with $n + 1/2$, which semiclassically comes from the broken SUSY SWKB quantization condition, to give an integer. Both branches asymptotically scale with $\propto \nu^{1/2}$.

Asymptotic eigenenergies for strong magnetic field of the sphere were found in [101] and read

$$\epsilon = \sqrt{2\nu\left(2n + (2m+1)\Theta(m)\right)}, \text{for}\, n \geq 0\,. \tag{5.5}$$

Surprisingly, the same energy levels as for the flat plane are obtained (see Eq. (2.12)). Numerical calculations performed in [102] show that the degeneracy of Landau levels in case of the sphere only holds for very strong magnetic fields. While convergence of the individual levels to the expected, degenerate Landau levels in case of the cone happens very quickly (with respect to magnetic field strength), it turns out to be very slow in case of the sphere. A second peculiarity found there is that the zero energy Landau level should not exist according to analytical calculations [101] but shows up numerically. As due to its energy being independent of the magnetic field strength ($\epsilon = 0$), it will not influence magnetic susceptibility calculations in a relevant way, we decided to assume it exists and keep it in this chapter for simplicity.

5.1.2. Weak magnetic field

We also want to examine what happens in the opposite limit, the weak magnetic field regime. Our strategy here is to decompose the problem into two separate ones. We first of all compute the eigenenergies in the complete absence of a magnetic field. This task can however only be performed when assuming a specific geometry. As an example, we do this for the pseudosphere. The second step is to consider the weak magnetic field as a small perturbation and calculate energy corrections within first order perturbation theory.

We try to find the spectrum of the pseudosphere in the absence of a magnetic field using SWKB. The effective potential in this case simplifies to

$$V(l) = \frac{m}{a}\exp\left(\frac{l}{a}\right)\,. \tag{5.6}$$

Assuming the energy ϵ^2, the classical turning points are given by $l_- = 0$ (the hard wall boundary of the surface) and $l_+ = \frac{a}{2}\log\left(\frac{a^2\epsilon^2}{m^2}\right)$. This gives rise to the classical action

$$
\begin{aligned}
S &= \frac{2\hbar}{a}\int_{l_-}^{l_+} dl\,\sqrt{\epsilon^2 - m^2\exp\left(\frac{2l}{a}\right)} \qquad (5.7)\\
&= 2\hbar\left[|\epsilon|\sqrt{1-\frac{m^2}{a^2\epsilon^2}\exp\left(\frac{2l}{a}\right)}\right]_{l_-}^{l_+}\\
&\quad -2\hbar\left[|\epsilon|\mathrm{artanh}\left(\sqrt{1-\frac{m^2}{a^2\epsilon^2}\exp\left(\frac{2l}{a}\right)}\right)\right]_{l_-}^{l_+}\\
&= 2\hbar|\epsilon|\left(-\sqrt{1-\frac{m^2}{a^2\epsilon^2}}+\mathrm{artanh}\left(\sqrt{1-\frac{m^2}{a^2\epsilon^2}}\right)\right)\\
&\approx 2\hbar|\epsilon|\left(\log\left(\frac{2a|\epsilon|}{|m|}\right)-1\right)\,.
\end{aligned}
$$

As a zero energy eigenstate obviously does not exist, we use the SWKB quantization condition for broken SUSY ($S = 2\pi\hbar\,(n+1/2)$) to obtain the energies

$$
\epsilon = \pm\pi\frac{n+\frac{1}{2}}{\mathrm{W}\left(\frac{2\pi\left(n+\frac{1}{2}\right)}{e|m|}\right)}\,, \qquad (5.8)
$$

where we used the *Lambert W function* $W(x)$ [98]. Note, that in this context e denotes the *Euler number*.

We now turn to the calculation of the energy correction $\Delta\epsilon$ due to a weak magnetic field. Contrary to the previous calculation, this one does not require us to specify a particular surface but holds in general. Starting from the radial Dirac Hamiltonian (Eq. (4.2)), we define the unperturbed Hamiltonian as

$$
\hat{H}_0 = \hbar v_F\left[-i\sigma_x\partial_l + \sigma_y\frac{m}{r(l)}\right]\,, \qquad (5.9)
$$

and the perturbation as

$$
\hat{H}_1 = \hbar v_F\sigma_y\frac{r(l)}{a^2}\nu\,. \qquad (5.10)
$$

We assume to have an eigenstate $|\Psi_0\rangle$ of $\hat{H}_0$ with energy E_0. The energy correction then reads

$$
\begin{aligned}
\Delta E &= \langle\Psi_0|\hat{H}_1|\Psi_0\rangle \qquad (5.11)\\
&= \frac{1}{2E_0}\left\langle\Psi_0\left|\left\{\hat{H}_0,\hat{H}_1\right\}\right|\Psi_0\right\rangle\\
&= \frac{\hbar^2v_F^2}{E_0a^2}\left(m\nu+\frac{\nu}{2}\langle\Psi_0|\sigma_z r'(l)|\Psi_0\rangle\right)\,.
\end{aligned}
$$

Interestingly, we found two contributions. The first term can be identified as the well-known Zeeman term, which splits the Kramers pairs, lowering the state with $m < 0$ while lifting the one with $m > 0$ in energy for rising magnetic field. However, the second term stems from the combination of a coaxial magnetic field and a curved geometry. This can be seen best when assuming a flat plane for which $r'(l) = 0$ and the term vanishes.

While this is physically very interesting, we will assume the geometric contribution to be subleading in the following. This can be justified for two reasons. First of all, due to chiral symmetry $\langle\Psi_0|\sigma_z|\Psi_0\rangle = 0$, so the expectation value is inherently suppressed due to the sole structure of σ_z, especially for barely changing $r'(l)$. Second, the magnitude of $r'(l)$ will be low for slowly varying radial profile compared to the first factor for angular quantum numbers m with high modulus. When neglecting this second term, we can approximate

$$\Delta\epsilon \approx \frac{m\nu}{\epsilon_0}\,. \tag{5.12}$$

For the case of the pseudosphere, we can overall write for positive energies

$$\epsilon = \pi\frac{n+\frac{1}{2}}{\mathrm{W}\left(\frac{2\pi\left(n+\frac{1}{2}\right)}{e|m|}\right)} + \frac{m\nu}{\pi\left(n+\frac{1}{2}\right)}\mathrm{W}\left(\frac{2\pi\left(n+\frac{1}{2}\right)}{e|m|}\right)\,. \tag{5.13}$$

We want to compare these findings with numerical calculations.

Fig. 5.2 shows the lowest five (positive) eigenenergies for angular quantum numbers $m = -1/2$ (upper left panel) and $m = 1/2$ (upper right panel), as well as the lowest ten (positive) eigenenergies for $m = -21/2$ (lower left panel) and $m = 21/2$ (lower right panel). Black crosses mark numerical solutions while the blue and red solid lines represent our approximation (Eq. (5.13)). We can see that the eigenenergies without magnetic field ($\nu = 0$) match well with our SWKB predictions for small magnitude of m, while especially the lowest eigenvalues are a bit off for higher magnitude of m. For negative m, also the finite ν approximation with perturbation theory worked very well, showing negative slopes in a good agreement with numerical results. Contrary to this, for small, positive m the slopes of the analytical approximation and the numerical solutions clearly differ, even though the slope is still positive, as anticipated. The quantitative disagreement most likely comes from the neglection of the second term in Eq. (5.11). This is supported by the fact that for large, positive m, the approximation again predicts the slope very well. As we asserted before, it becomes better for higher magnitude of m.

5.1.3. Numerical calculation of the spectrum

As we discussed in the previous two paragraphs, we can approximate the Landau level spectrum very well for the limits of strong and weak magnetic fields. In general, however, it is virtually impossible to get a meaningful expression for the eigenenergies in closed form for the whole range of ν. We therefore take a look at the numerical results and discuss the spectra of our three exemplary surfaces, the pseudosphere, the cone and

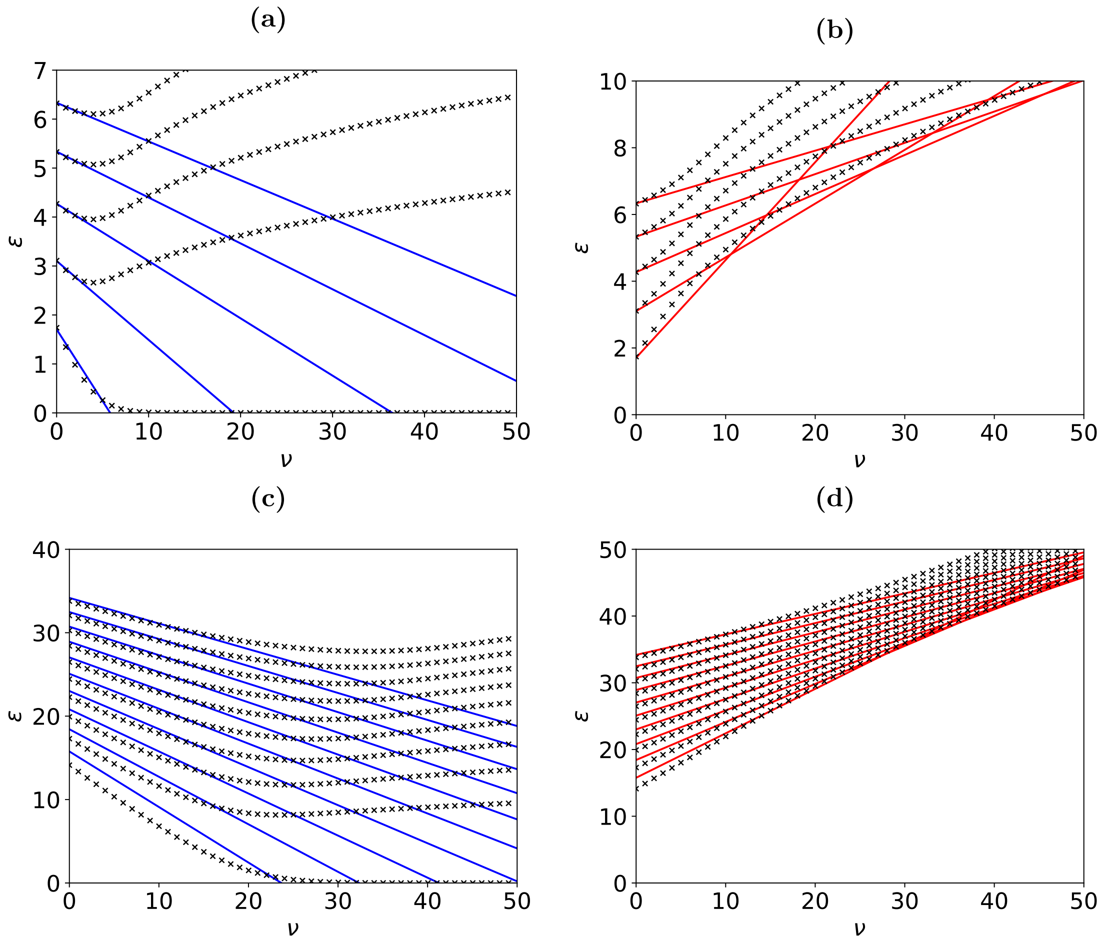

Figure 5.2: Lowest positive eigenenergies as a function of field strength ν of the radial Dirac Hamiltonian (Eq. (4.2)) on a pseudosphere in a coaxial magnetic field for $m = -1/2$ ((a)), $m = 1/2$ ((b)), $m = -21/2$ ((c)), as well as for $m = 21/2$ ((d)). Solid lines represent analytical solutions gained using SWKB for the zero field energies and first order perturbation theory for finite field corrections (Eq. (5.13)). Black crosses mark numerical solutions. A lattice spacing of $\Delta l = 0.005a$ as well as a cut-off of $L = 5a$ were used.

the sphere. As seen in the first paragraph of this section, the spectrum is qualitatively different for the two branches of the angular quantum number, $m < 0$ and $m > 0$. Subspectra with the same sign of m behave similarly, we therefore pick $m = -3/2$ and $m = 3/2$ as two representatives.

Fig. 5.3 shows the Landau levels in the vicinity of $\epsilon = 0$ for the two angular quantum numbers. The following spectral features can be observed:

- In case of the pseudosphere, eigenenergies show different scalings in the magnetic field ν for the two branches of the angular quantum number (blue lines for $m = -3/2$ and red lines for $m = 3/2$).
- The spectrum is double degenerate (Kramers' degeneracy) for vanishing magnetic field $\nu = 0$ due to preservation of TRS, as discussed in Chapter 3.
- Three regimes are visible. Within the first one (I), the eigenenergies have approximately linear scaling, suggesting that we are in a weak field regime. Even though a second contribution to the energy splitting is present, as we saw in the last section, we call this region the Zeeman regime in the following. Taking a closer look at the localization of the eigenstates (not shown here), it becomes clear that the states in this regime are edges states. The magnetic field is too weak to fully confine the electrons within the bulk.
- In regime (III), eigenenergies scale asymptotically in ν as stated before. We call it the Landau regime in the following. Eigenstates are fully localized inside the bulk.
- The regime (II) is where the transition between the Zeeman and the Landau regime takes place. It is particularly hard to describe, as the magnetic field is too strong to be treated as a small perturbation and too weak for the asymptotic approximations to be valid.

Now that we know how the subspectrum of each geometry behaves for the two branches of m, we also have to look at the complete spectrum in each case. Contrary to the subspectrum of a fixed angular quantum number, which is virtually a one-dimensional system, levels can show crossings or avoided crossings, creating a complicated pattern which will also reflect in susceptibility. We show the complete spectrum for all three geometries (Fig. 5.4 for the pseudosphere, Fig. 5.5 for the cone and Fig. 5.6 for the sphere) but divide it between the positive and negative angular branches for convenience.

Again, we can find some interesting features which stem from the combination of all the subspectra. For $m < 0$, the cone shows clearly distinguishable, highly degenerate Landau levels while in case of the sphere those levels can be seen but seem to be more broadened. As already explained above, further numerical investigations done in [102] hint that while the eigenstates are degenerate in the high field limit, it takes a much higher field compared to the cone for them to converge onto the common Landau level. The most notable feature might be that the pseudosphere shows much flatter levels in this angular momentum branch. As expected, degeneracies can barely be observed. For $m > 0$, the eigenstates are in general higher in energy, compared to the other branch. In

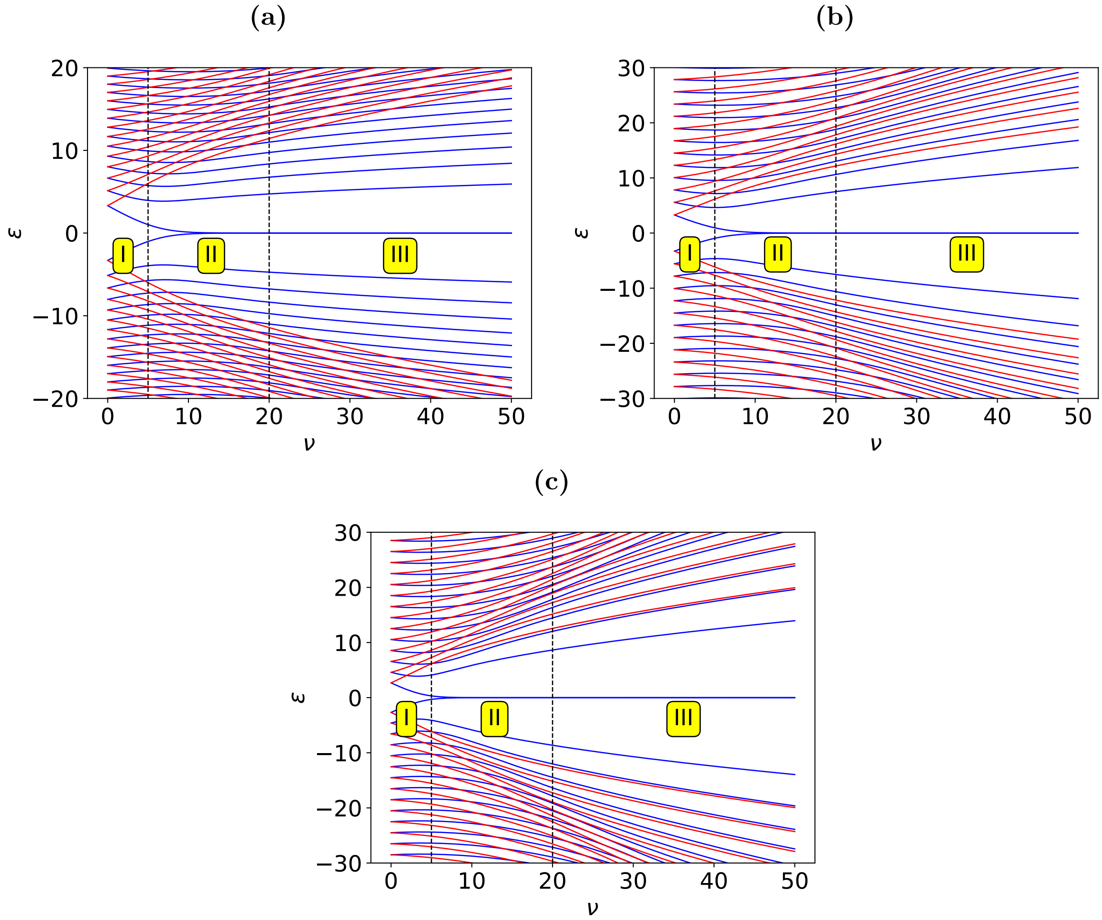

Figure 5.3: Numerically gained eigenenergies (closest to $\epsilon = 0$) as a function of field strength ν of the radial Dirac Hamiltonian (Eq. (4.2)) on a pseudosphere ((a)), a cone ((b)), as a well as a sphere ((c)) in a coaxial magnetic field for $m = -3/2$ (blue lines) and $m = 3/2$ (red lines). Lattice spacings of $\Delta l = 0.005a$ for the pseudosphere, $\Delta l = 0.003a$ for the cone and $\Delta l = 0.0015a$ for the sphere were used. Cut-offs of $L = 5a$ for the pseudosphere, $L = \sqrt{2}a$ for the cone and $L = \pi a/2$ for the sphere were used.

(a)

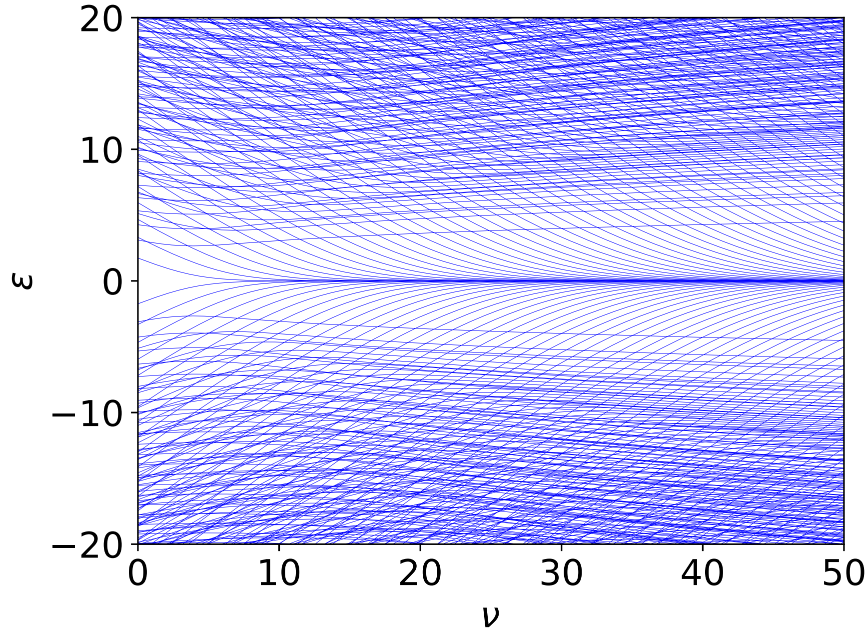

(b)

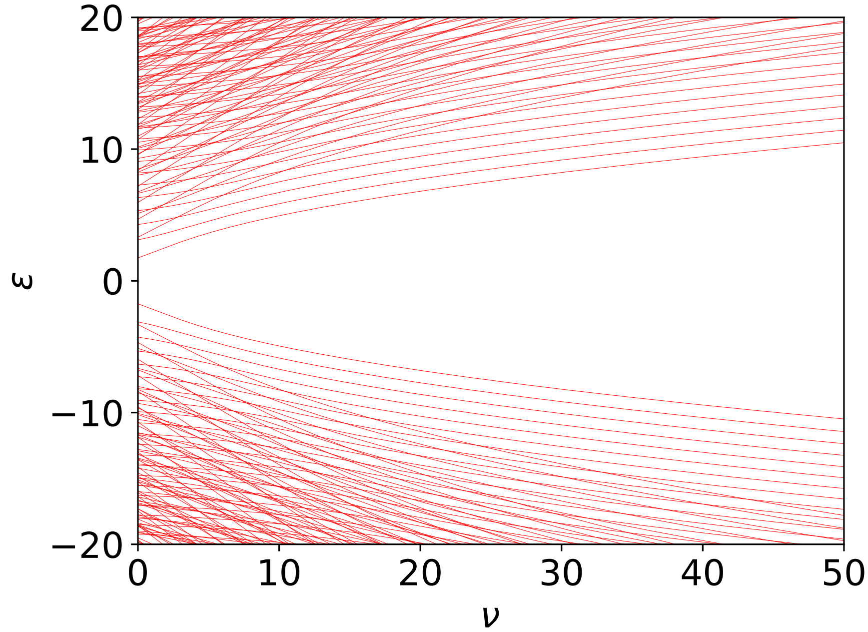

Figure 5.4: Numerically gained eigenenergies (closest to $\epsilon = 0$) as a function of field strength ν of the radial Dirac Hamiltonian (Eq. (4.2)) on a pseudosphere in a coaxial magnetic field. (a) shows eigenenergies for all $m < 0$, while (b) shows them for all $m > 0$. Lattice spacing of $\Delta l = 0.005a$ and cut-off of $L = 5a$ were used.

(a)

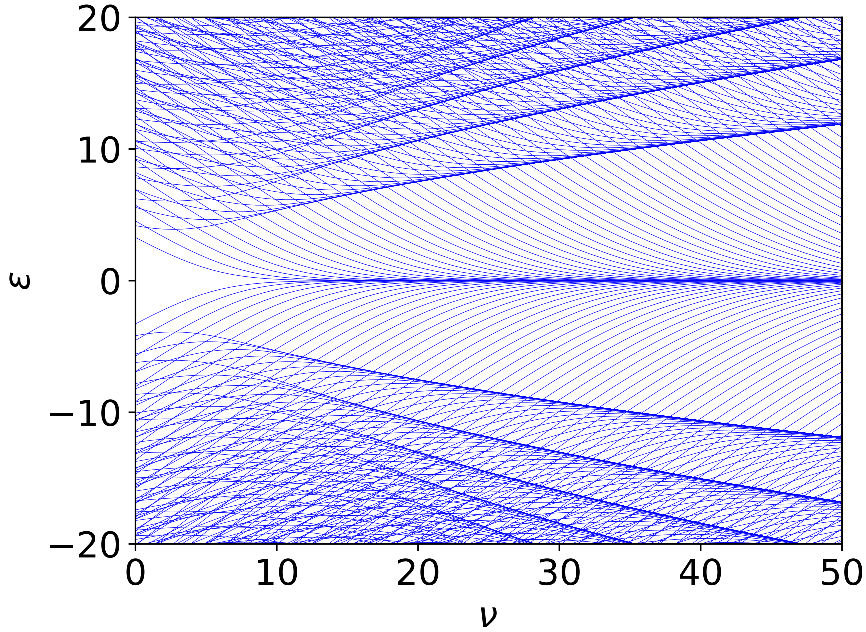

(b)

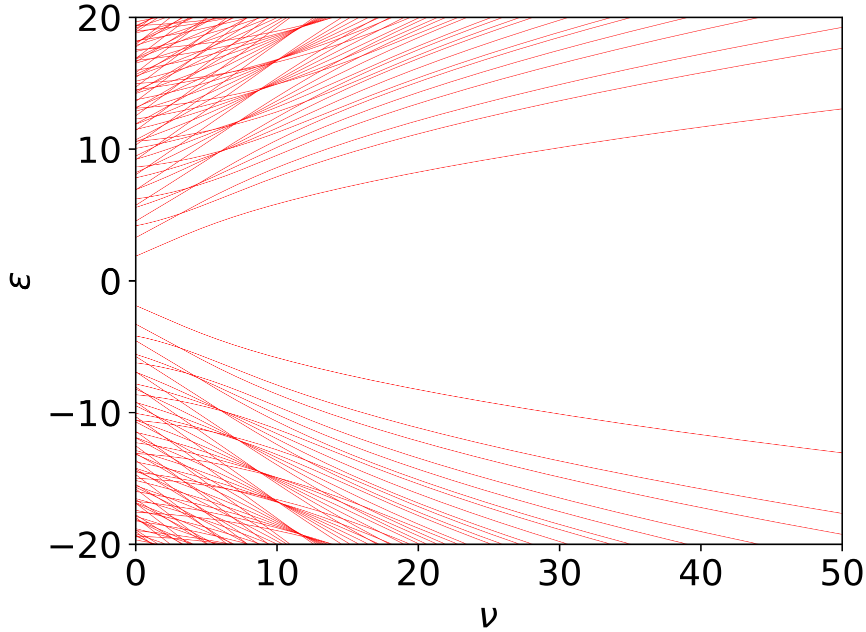

Figure 5.5: Numerically gained eigenenergies (closest to $\epsilon = 0$) as a function of field strength ν of the radial Dirac Hamiltonian (Eq. (4.2)) on a cone in a coaxial magnetic field. (a) shows eigenenergies for all $m < 0$, while (b) shows them for all $m > 0$. Lattice spacing of $\Delta l = 0.003a$ and cut-off of $L = \sqrt{2}a$ were used.

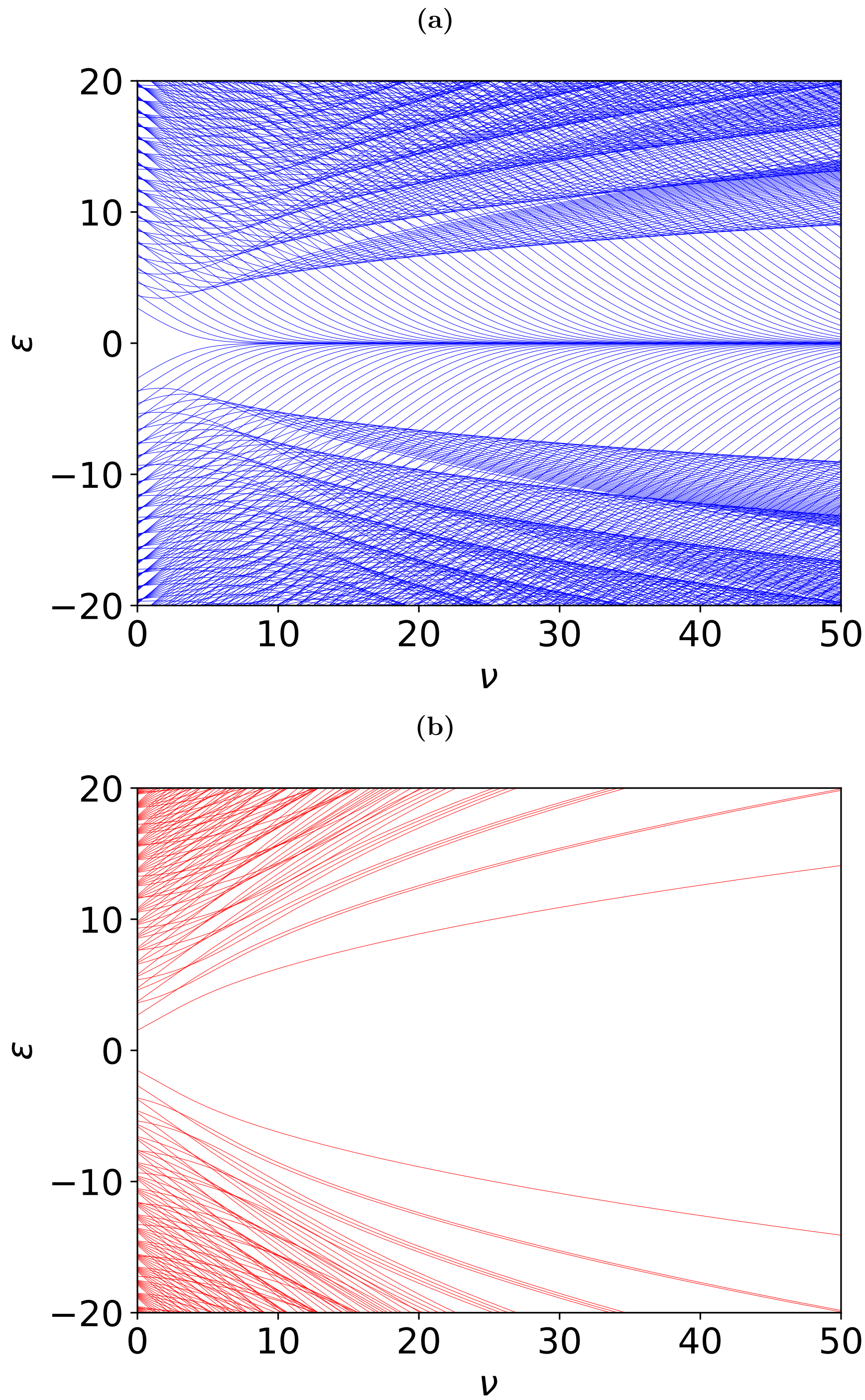

Figure 5.6: Numerically gained eigenenergies (closest to $\epsilon = 0$) as a function of field strength ν of the radial Dirac Hamiltonian (Eq. (4.2)) on a sphere in a coaxial magnetic field. (a) shows eigenenergies for all $m < 0$, while (b) shows them for all $m > 0$. Lattice spacing of $\Delta l = 0.0015a$ and cut-off of $L = \pi a/2$ were used.

the high field limit, they are not degenerate in case of the cone but show an interesting phenomenon. There exist points in the transition zone between the Zeeman and Landau regimes, where many levels exactly cross, leading to a highly degenerate eigenenergies. All these points seem to lay on a straight line, creating an oscillation of density of states (DOS) along it. In case of the sphere it may be observed that levels are only approximately degenerate (as in case of the other angular branch). The pseudosphere shows non-degenerate levels which increase much steeper in energy compared to the $m < 0$ branch. All observed features here are in accordance with our analytical findings.

Let us conclude this section by noting that numerical convergence of the zero energy levels with $m = -1/2$ (for all surfaces) and $m = -3/2$ (in case of the sphere) is poor so that we decided to neglect these states in the following, whenever using numerically obtained spectra. Since these are zero energy states, this step will not affect the susceptibility in a meaningful way.

5.2. Foundations of magnetization

In the first part of this section, we will introduce the thermodynamical description of magnetization. In the second part, we summarize the basic properties of the susceptibility of massless Dirac electrons on a plane.

5.2.1. Thermodynamical description of magnetization

The susceptibility of a non-interacting Fermi gas is most conveniently computed in the grand canonical ensemble, characterized by temperature and chemical potential, allowing for exchange of entropy and particles, respectively. As we have already noted before, the spectra of surfaces with defining equation in the form of $r(l) = af(l/a)$, where a is the radius at $l = 0$ and f only depends on the ratio r/a, can be written in a scale invariant manner (pseudosphere, cone and sphere belong to this class). Therefore, before proceeding, let us have a look at the different energy scales, that enter the game. These are the energy set by the geometry, $\hbar v_F/a$, the chemical potential μ^{SI}, the thermal energy $k_B T^{SI}$, as well as the energy set by the magnetic length, $\hbar v_F/l_B$. The scale invariance of the problem makes evident that only three of them are non-trivially independent of each other. Consequently, it makes sense to work with scale independent quantities. We choose $\hbar v_F/a$ as a basis energy scale and write all remaining energies in terms of it. The number of flux quanta, $\nu = \Phi/\Phi_0$, which we previously defined, already relates the energy scale set by the magnetic length to our basis energy scale. We further define the dimensionless thermal energy

$$T = \frac{a}{\hbar v_F} k_B T_{SI} \, , \tag{5.14}$$

and the dimensionless chemical potential

$$\mu = \frac{a}{\hbar v_F} \mu_{SI} \, . \tag{5.15}$$

We also frequently use the already defined dimensionless energy $\epsilon = Ea/(\hbar v_F)$ during our calculations.

To compute the grand canonical potential, we need the density of states (DOS). Since we have chiral symmetry, it is enough to consider it for positive energies. Given the positive single particle eigenenergies ϵ_{nm}, we can write down the DOS as

$$\rho(\epsilon) = \sum_m \sum_n \delta(\epsilon - \epsilon_{nm}) \,. \tag{5.16}$$

Using the antiderivative of the Fermi-Dirac distribution,

$$F(\epsilon) = -T \log\left(1 + \exp\left(-\frac{\epsilon}{T}\right)\right) \,, \tag{5.17}$$

and taking into account the symmetry of the spectrum with respect to $\epsilon = 0$, we can write the grand canonical potential as

$$\begin{aligned} \Omega(T, \nu, \mu) &= \sum_m \sum_n (F(\epsilon_{nm} - \mu) + F(-\epsilon_{nm} - \mu)) \\ &= \int_0^\infty d\epsilon\, \rho(\epsilon) F(\epsilon - \mu) + \int_0^\infty d\epsilon\, \rho(\epsilon) F(-\epsilon - \mu) \,. \end{aligned} \tag{5.18}$$

Note, that also $\Omega(T, \nu, \mu)$ is now given in units of $\hbar v_F/a$. In SI units, the magnetic susceptibility is defined as [103]

$$\chi_{SI} = -\frac{\mu_0}{A} \left(\frac{\partial^2 \Omega^{SI}}{\partial B^2}\right)_{T_{SI}, \mu_{SI}} \,, \tag{5.19}$$

where μ_0 is the vacuum permeability and we normalized the quantity to the surface area A. Instead of calculating χ_{SI} directly, it makes sense to define the corresponding dimensionless susceptibility,

$$\chi = -\left(\frac{\partial^2 \Omega}{\partial \nu^2}\right)_{T, \mu} \,, \tag{5.20}$$

and relate it to χ_{SI} by comparing coefficients and variables,

$$\chi_{SI} = \frac{\mu_0 e^2}{4\hbar} v_F \frac{a^3}{A} \chi \,. \tag{5.21}$$

To have some feeling of how big the effects can be, we compare this to the Landau diamagnetism of non-relativistic Schrödinger electrons, given in two dimensions by $\chi_L^{SI} = -\mu_0 e^2/(12\pi m_e)$ [104], where e is the elementary charge and m_e is the free electron mass. We arrive at

$$\frac{\chi^{SI}}{|\chi_L^{SI}|} = 3\pi \frac{m_e}{\hbar} v_F \frac{a^3}{A} \chi \,. \tag{5.22}$$

Since a is the only characteristic length of the geometry, the surface must be $A \propto a^2$, so that surprisingly $\chi^{SI}/|\chi_L^{SI}| \propto a$. This happens, since the energy scale (defined by the typical length of the geometry, whereas the magnetic length is fully absorbed into χ) of non-relativistic electrons is set by $\hbar^2/(m_e a^2)$, while the one of ultra-relativistic electrons is given by $\hbar v_F/a$. Choosing typical values for a mesoscopic setup, $v_F = 10^5$m/s, $a =$ 200nm, and $A = 40000\text{nm}^2$, this roughly equals $\chi^{\mathrm{SI}}/|\chi_{\mathrm{L}}^{\mathrm{SI}}| \approx 173\chi$. This means that for these values, $\chi = 1$ is approximately 173 times as strong as (or two orders of magnitude stronger than) Landau diamagnetism of a non-relativistic, free 2DEG.

When proceeding to calculate the grand canonical potential, we face the problem that the spectrum of a Dirac operator is in general not bounded from below. It makes sense to perform a mathematical trick, following [70],

$$
\begin{aligned}
\Omega(T,\mu,\nu) &= \int_0^\infty d\epsilon\,\rho(\epsilon)F(\epsilon-\mu) + \int_0^\infty d\epsilon\rho(\epsilon)F(-\epsilon-\mu) \qquad (5.23)\\
&= -T\int_0^\infty d\epsilon\,\rho(\epsilon)\log\left(1+\exp\left(-\frac{\epsilon-\mu}{T}\right)\right)\\
&\quad -T\int_0^\infty d\epsilon\,\rho(\epsilon)\log\left(1+\exp\left(-\frac{-\epsilon-\mu}{T}\right)\right)\\
&= -T\int_0^\infty d\epsilon\,\rho(\epsilon)\log\left(1+\exp\left(-\frac{\epsilon-\mu}{T}\right)\right)\\
&\quad -T\int_0^\infty d\epsilon\,\rho(\epsilon)\log\left(\exp\left(-\frac{-\epsilon-\mu}{T}\right)\left[1+\exp\left(-\frac{\epsilon+\mu}{T}\right)\right]\right)\\
&= -\int_0^\infty d\epsilon\,\rho(\epsilon)(\epsilon+\mu)\\
&\quad -T\int_0^\infty d\epsilon\,\rho(\epsilon)\log\left(1+\exp\left(-\frac{\epsilon-\mu}{T}\right)\right)\\
&\quad -T\int_0^\infty d\epsilon\,\rho(\epsilon)\log\left(1+\exp\left(-\frac{\epsilon+\mu}{T}\right)\right)\\
&= -\int_0^\infty d\epsilon\,\rho(\epsilon)(\epsilon+\mu) + \int_0^\infty d\epsilon\,\rho(\epsilon)\left[F(\epsilon-\mu)+F(\epsilon+\mu)\right]\\
&=: \Omega^0(\mu,\nu) + \Omega^T(T,\mu,\nu)\,,
\end{aligned}
$$

where we decomposed the grand canonical potential into two parts. $\Omega^0(\mu,\nu)$ is temperature-independent and represents the contribution of the negative energy states to the grand canonical potential of the system at $T = 0$, i.e. when all negative energy states are fully occupied. The part $\Omega^T(T,\mu,\nu)$ carries the contribution to the grand canonical potential which stems from the deviation to this state, i.e. it takes care of the correction coming from finite temperature and positive energy states. The advantage of this decomposition is that all possibly divergent parts of $\Omega(T,\mu,\nu)$, due to the spectrum not being bounded from below, are inside $\Omega^0(\mu,\nu)$, which does not depend on temperature and can be analyzed separately for different regularization schemes. Possible oscillations of the magnetic susceptibility, like de Haas-Van Alphen (dHvA) oscillations, come from $\chi^T(T,\mu,\nu)$ [70] and may be analyzed independently of the respective regularization. Before proceeding, let us note that the temperature-dependent part of the grand canonical potential is independent of the sign of μ. Strictly, this is not fully true for the temperature-dependent part. Since we are most interested in the first mentioned part, we assume $\mu \geq 0$ in the following for convenience.

A very powerful method to evaluate the integral for the grand canonical potential is to go to Laplace space. We can integrate the temperature-dependent part of the grand canonical potential twice by parts,

$$\begin{aligned} \Omega^T(T,\nu,\mu) &= \int_0^\infty d\epsilon\, \rho(\epsilon)\, [F(\epsilon-\mu)+F(\epsilon+\mu)] \\ &= \int_0^\infty d\epsilon\, \mathcal{N}(\epsilon)\, \left[F''(\epsilon-\mu)+F''(\epsilon+\mu)\right] , \end{aligned} \tag{5.24}$$

where $\mathcal{N}''(\epsilon) = \rho(\epsilon)$. The boundary terms of both partial integration steps vanish as the DOS approaches zero at $\epsilon = 0$ and the Fermi-Dirac part approaches zero at $\epsilon \to \infty$. Looking at Eq. (5.24), we see that the integral has the form of a cross-correlation between $\mathcal{N}(\epsilon)$ and $F''(\epsilon)$, evaluated at $-\mu$ and μ for the first and the second part of the sum, respectively. This can be written as

$$\Omega^T(T,\nu,\mu) = (\mathcal{N} \star F'')(-\mu) + (\mathcal{N} \star F'')(\mu)\,, \tag{5.25}$$

where $\star$ denotes the cross-correlation operator. This can be evaluated most comfortably using the cross-correlation property of the bilateral Laplace transform [105]. First of all, we have to transform $\mathcal{N}(\epsilon)$ and $F''(\epsilon)$ into Laplace space,

$$\mathcal{N}(s) = \int_{-\infty}^\infty d\epsilon\, \mathcal{N}(\epsilon) \exp(-\epsilon s)\,, \tag{5.26}$$

$$F''(s) = \int_{-\infty}^\infty d\epsilon\, F''(\epsilon) \exp(-\epsilon s)\,. \tag{5.27}$$

Now we are in the position to use the mentioned property of the Laplace transform and represent the temperature-dependent part of the grand canonical potential as

$$\begin{aligned} \Omega^T(T,\nu,\mu) &= \frac{1}{2\pi i}\int_{\sigma-i\infty}^{\sigma+i\infty} ds\, \mathcal{N}^*(-s^*) F''(s) \exp(-\mu s) \\ &\quad + \frac{1}{2\pi i}\int_{\sigma-i\infty}^{\sigma+i\infty} ds\, \mathcal{N}^*(-s^*) F''(s) \exp(\mu s) \\ &= \frac{1}{\pi i}\int_{\sigma-i\infty}^{\sigma+i\infty} ds\, \mathcal{N}^*(-s^*) F''(s) \cosh(\mu s)\ , \end{aligned} \tag{5.28}$$

where σ is a real number which needs to be chosen within the region of convergence (ROC).

5.2.2. Susceptibility of massless Dirac electrons on a plane

Before we start considering curved surfaces, it makes sense to revise the basic properties of the magnetic susceptibility of a free gas of massless Dirac electrons on a plane. A thorough study of this problem is provided by [70].

Landau diamagnetism is a key property of the non-relativistic 2DEG and describes a diamagnetic contribution to the susceptibility which is independent of temperature and chemical potential [7, 70, 104]. Contrary to this, when replacing these Schrödinger electrons by massless Dirac electrons, the effect differs drastically. In the limit of zero temperature and vanishing field, it can be shown to approach negative infinity at zero chemical potential [106]. When considering a finite magnetic field ν or chemical potential μ, the Landau susceptibility shows a scaling of $\chi \propto -1/\sqrt{\nu + \mu^2/\alpha}$, with some constant α [106]. Contrary to the non-relativistic case, the effect becomes weaker for non-zero temperature [106].

When thermal energy is much smaller than the level spacing due to Landau quantization (in the regime of low temperature and strong magnetic field), dHvA oscillations can occur at chemical potentials which are higher than the Landau level spacing [70]. These can be described by the oscillating part of the overall susceptibility which, to leading order in chemical potential and adapted to our scale invariant definition of susceptibility (Eq. 5.20), reads [70]

$$\chi_{plane}^{dHvA} = \frac{1}{2\sqrt{\pi}} \frac{\mu^3}{\nu^2} \sum_{k=1}^{\infty} R_T\left(\frac{\pi k \mu}{\nu}\right) \cos\left(\frac{\pi}{2} \frac{k\mu^2}{\nu}\right), \tag{5.29}$$

with the temperature damping factor $R_T(x) = \pi T x / \sinh(\pi T x)$ [70, 104].

5.3. Temperature-dependent susceptibility χ^T

With all the preparatory work done, we want to take a look at the numerically gained temperature-dependent susceptibility χ^T (Eq. 5.23) for the three surfaces of pseudosphere, cone and sphere. In general, it is a function of three parameters, T, μ and ν. We choose three temperature regimes, $T = 0.1$ (thermal energy is much smaller than the energy scale set by the geometry), $T = 0.5$ (thermal energy is smaller but in the same order of magnitude as the energy scale set by the geometry) and $T = 1.5$ (thermal energy is higher but in the same order of magnitude as the energy scale set by the geometry). We provide a heatmap of χ^T as a function of ν (x-axis) and μ (y-axis) for all three temperature regimes. All of them feature two sections through the μ-ν-plane, one with fixed $\nu = 30$ (green plot / dashed line), the other with fixed $\mu = 25$ (ruby plot / dashed line).

5.3.1. Low temperature regime

Fig. 5.7 shows $\chi^T(T, \mu, \nu)$ plotted as a function of ν and μ at $T = 0.1$ for the pseudosphere, cone and sphere.

In general, contributions from individual levels, even if they are close to each other, can be observed in this regime. We can identify the following properties:

- For chemical potentials close to $\epsilon = 0$, the only effect we can see is levels condensing onto the zeroth Landau level, as ν increases, which is a finite-size effect.

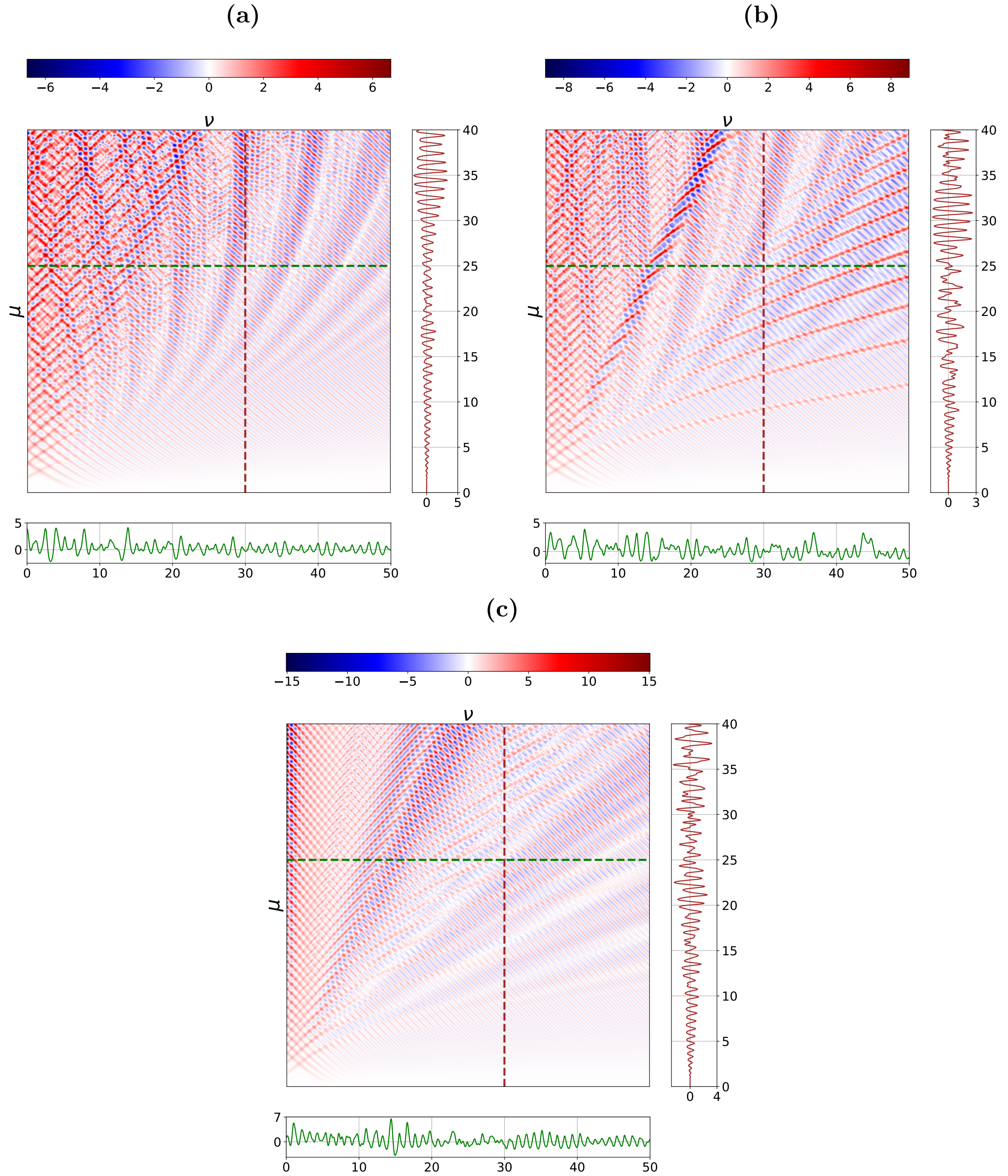

Figure 5.7: Numerically gained temperature-dependent magnetic susceptibility χ^T as a function of magnetic field ν and chemical potential μ at $T = 0.1$ for the pseudosphere ((a)), the cone ((b)) and the sphere ((c)). Energy eigenvalues were calculated using the parameters given in Fig. 5.4, Fig. 5.5 and Fig. 5.6

.

Other effects are strongly suppressed, as the chemical potential is too small to see fingerprints of higher levels.

- In the regime of weak magnetic fields ν and high chemical potentials μ, finite-size effects also dominate the behavior. We have seen in the previous section that eigenenergies rise or fall linearly in this case (Zeeman regime), roughly depending on the sign of m. This leads to a diamond pattern in χ^T.

- All three geometries show the appearance of "fingers", connected regions where susceptibility is lower than in their respective surrounding areas. These fingers are approximately located along straight lines in case of the sphere, while they are curved in case of the pseudosphere or the cone. In the last mentioned cases they also seem to become broader for rising chemical potential.

- In case of the cone, a finger can be seen which is clearly different to the aforementioned. It lays along an almost perfect line between the points $(\nu, \mu) = (0, 0)$ and $(\nu, \mu) = (25, 40)$ and shows enhanced signal compared to the surrounding area. This is a hallmark of the aforementioned highly degenerate points laying along a line in the spectrum of the positive angular branch and creating oscillations of the DOS along this line.

- Signatures of the Landau regime are visible in case of the cone, while they seem to be strongly attenuated for the sphere and completely absent for the pseudosphere. This can be attributed to the high degeneracy of Landau levels in the first mentioned case, the only approximate degeneracy in the second mentioned one (convergence onto Landau levels is very slow with respect to ν) and completely absent degeneracy in the last one. The corresponding dHvA oscillations can hardly be identified in the sections along lines with constant ν.

- Overall, finite-size effects clearly dominate this temperature regime. This can especially be seen when solely looking at the section plots, where χ^T oscillates with almost constant frequency, reflecting the diamond structure of the spectrum already mentioned before. Similar effects were also observed in quantum rings [107–110] and graphene [70].

5.3.2. Moderate temperature regime

Fig. 5.8 shows $\chi^T(T, \mu, \nu)$ plotted as a function of ν and μ at $T = 0.5$ for the pseudosphere, cone and sphere. As dHvA oscillations are so important in this regime, a detailed plot of χ^T as a function of μ at fixed ν is also given. The highly degenerate Landau levels in case of the cone and the sphere are marked by vertical, dashed lines. In case of the pseudosphere, where Landau levels are not degenerate in m and the main Landau structure is given by m for $m > 0$ (see our discussion at the beginning of the chapter), black lines correspond to states with $n = 0$ / $m > 0$, while orange ones correspond to $n = 1$ / $m > 0$.

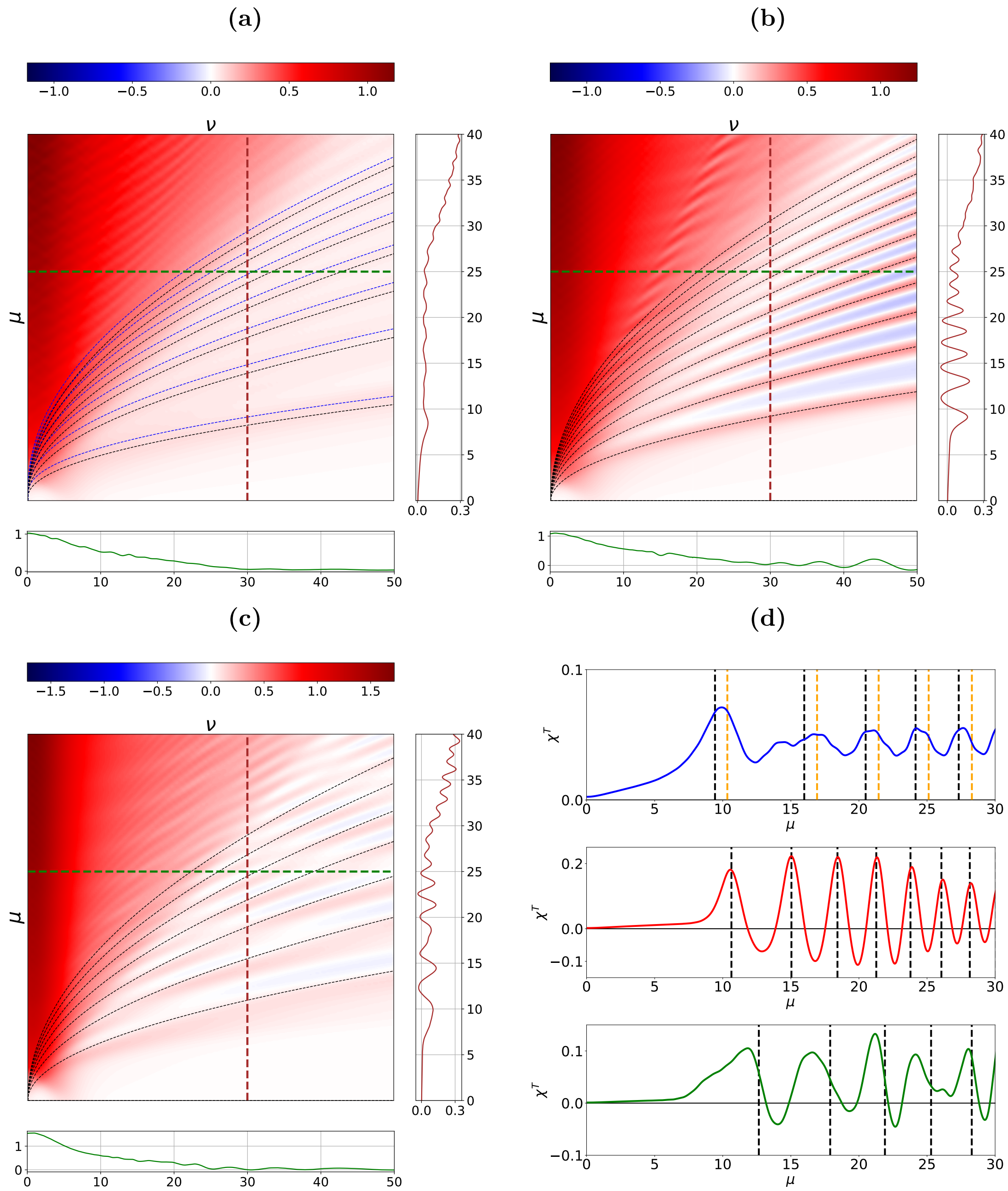

Figure 5.8: Numerically gained temperature-dependent magnetic susceptibility χ^T as a function of magnetic field ν and chemical potential μ at $T = 0.5$ for the pseudosphere ((a)), the cone ((b)) and the sphere ((c)). Panel (d) shows a section at fixed magnetic field $\nu = 40$ for the pseudosphere (blue graph), the cone (red graph) and the sphere (green graph). In case of the cone and the sphere, the highly degenerate Landau levels are marked as black lines. In case of the pseudosphere, states with $n = 1$ (black lines), as well as $n = 2$ (blue lines in the heatmap, orange lines in the section) are marked (see Eq. 71 in [27]). Energy eigenvalues were calculated using the parameters given in Fig. 5.4, Fig. 5.5 and Fig. 5.6

.

Temperature is now at the order of magnitude of the characteristic energy $\hbar v_F/a$ determined by the length scale of the geometry. This smoothes finite-size effects and increases visibility of actual bulk properties of the system. We can observe the following properties:

- In case of weak magnetic fields and high chemical potentials, the overall behavior of all three geometries is paramagnetic. This declines rapidly when increasing the magnetic field strength.
- Conversely, for strong magnetic fields and low chemical potentials, dHvA oscillations can be observed for all three geometries. In the vicinity of $\mu = 0$, they are absent, since the energy of the zeroth Landau level does not change with magnetic field and therefore no oscillation can be observed until μ is high enough for the first excited Landau level to be occupied. Oscillations are most pronounced for the cone, as its eigenenergies converge quickly onto the highly degenerate Landau levels when increasing the field. This convergence is, as already noted before, much slower in case of the sphere, where these oscillations are present, albeit smeared out. This does not happen due to temperature smoothing, but because of the only approximate degeneracy of the levels.
- dHvA oscillations of the sphere are different compared to those of the cone. It can be seen that in case of the cone, the Landau level energies exactly align with the maxima of the susceptibility. Contrary to this, Landau level energies seem to be a bit higher in energy than the chemical potentials, at which χ^T peaks. In general, the susceptibility oscillation is much more irregular in case of the sphere compared to the very clean oscillations in case of the cone.
- While dHvA oscillations were expected for the cone and the sphere, they come as a surprise in case of the pseudosphere because all Landau levels are non-degenerate. The form of oscillations in the heatmap suggests that they originate from $\epsilon \propto \nu^{1/2}$ states ($m > 0$) states rather than from $\epsilon \propto \nu^{1/4}$ ($m < 0$) states. The explanation for this is that in the high field limit, Landau levels become approximately degenerate in n. As discussed before, when looking at Eq. (5.2), the leading order term of the energy in ν is $\epsilon \propto \sqrt{2m\nu}$ for strong magnetic fields. This is very counterintuitive. Energies are not only not degenerate anymore, but they depend stronger on the angular quantum number m than on the main quantum number n. Therefore, it is the quantum number m which creates the level structure and therefore the dHvA oscillations here. Nevertheless, the peaks of the oscillations do not seem to align with any of the Landau level energies.
- Signatures of $\epsilon \propto \nu^{1/4}$ ($m < 0$) states in case of the pseudosphere are not visible at all. This can be explained by the much weaker dependence of the energy on the magnetic field.

5.3.3. High temperature regime

Fig. 5.9 shows $\chi^T(T,\mu,\nu)$ plotted as a function of ν and μ at $T = 1.5$ for the pseudosphere, cone and sphere.

In this regime, temperature is expected to smear out any oscillatory part of the susceptibility. We find the following items:

- The overall behavior is paramagnetic in all regions of ν and μ.
- Still, two regions can be identified. One for high chemical potential and low field strength, where paramagnetism is strong and one for the converse case, where it is weak. We can expect the two regions to be governed by dominant Zeeman and Landau behavior, respectively.
- The two regions seem to be approximately separated by a straight line.
- Differences between the three geometries can hardly be observed. Calculated susceptibilities even agree quantitatively very well. This suggests an almost equal mean density of states for all three surfaces. Obviously, one can ask whether this universal behavior can be observed with all surfaces of revolution.

We can sum up this section by noticing that we examined the temperature-dependent susceptibility for three exemplary surfaces, the pseudosphere, the cone and the sphere. While some features of χ^T can be identified, which are characteristic for the respective surface, most features are shared by all three of them. A big exception from this are dHvA oscillations, best visible in the moderate temperature regime, which clearly differ in amplitude, phase and shape, depending on the individual geometry.

5.4. Temperature-independent susceptibility χ^0

We have not yet taken the temperature-independent susceptibility χ^0 (Eq. 5.23) into account. As it does not depend on temperature but only on chemical potential μ and magnetic field ν, it might seem at first glance that this is the easiest contribution to calculate. However, this is not true since we sum over the negative energy states which are all fully occupied, leading to a divergent grand canonical potential $\Omega^0(\nu,\mu)$. There are of course techniques to regularize this singularity and isolate a finite, field-dependent part. This is impractical in case of our curved surfaces because the spectrum is often not degenerate in the angular quantum number m, as well as only known in an analytical form for strong fields and not too high quantum numbers m and n. The issue may be fixed when going back to the origin of the problem, the description of emergent, effectively massless Dirac fermions in condensed matter systems. These quasiparticles only behave in this manner within a very limited energy range in the vicinity of a certain Dirac point in the Brillouin zone of the respective material. When going too far away from this point, the quasiparticle loses more and more of its Dirac nature, gains

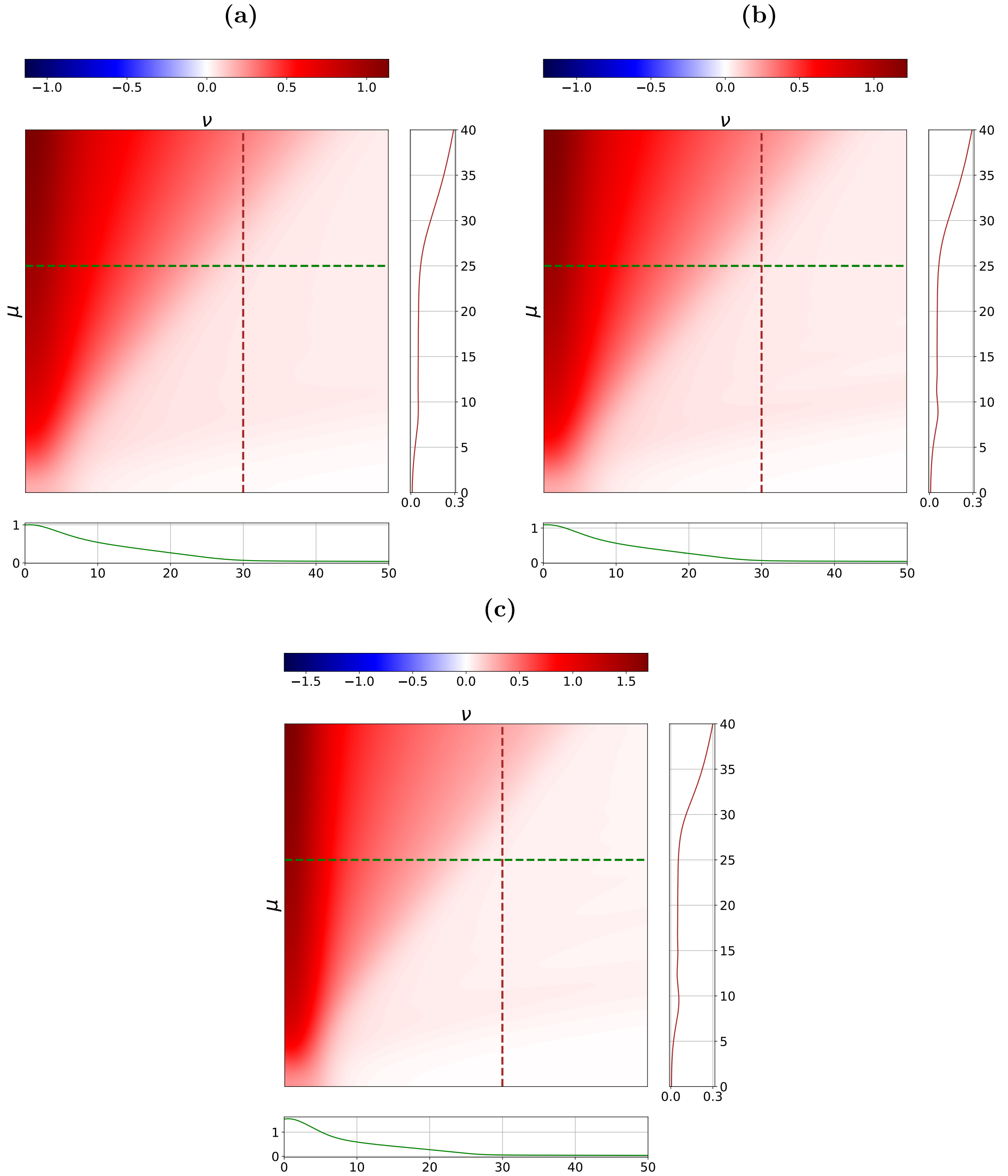

Figure 5.9: Numerically gained temperature-dependent magnetic susceptibility χ^T as a function of magnetic field ν and chemical potential μ at $T = 1.5$ for the pseudosphere ((a)), the cone ((b)) and the sphere ((c)). Energy eigenvalues were calculated using the parameters given in Fig. 5.4, Fig. 5.5 and Fig. 5.6

.

effective mass and eventually behaves more like a non-relativistic Schrödinger particle. Henceforth, in a real system, not all negative energy states contribute to $\Omega^0(\nu, \mu)$, as only a limited number even exists. We can introduce a UV cut-off of the DOS at a certain energy ϵ_C, where we assume that the system is not correctly described anymore by our Dirac model and treatment of properties in this regime are therefore beyond the scope of this work. The simplest way to implement this is obviously to multiply the DOS with a Heaviside function $\Theta(\epsilon_C - \epsilon)$. This, however, leads to problems on its own since when varying the magnetic field ν, levels may cross ϵ_C, creating an abrupt jump of the thermodynamic potential which reflects in singular magnetization and susceptibility. This is of course unphysical and can be solved by replacing the Heaviside function with a softer regulator. The ideal choice for this are sigmoid functions which are zero at the origin and continuously approach one when the argument goes to infinity. We choose the Fermi-Dirac function and introduce an artificial smoothing temperature T_C. The DOS modified in this way can be written as

$$\rho_C(\epsilon) = \rho(\epsilon) \frac{1}{1 + \exp\left(\frac{\epsilon - \epsilon_C}{T_C}\right)} . \tag{5.30}$$

As an example, we calculate χ^0 for $\epsilon_C = 40$ and $T_C = 8$ which is shown in Fig. 5.10. A few features immediately catch the eye:

- The overall behavior is diamagnetic in all regions of ν and μ.
- The absolute value of χ^0 seems to increase linearly with μ.
- Diamagnetism is strongest for very weak magnetic fields ν, increases with field strength and decreases again from approximately $\nu = 30$ on. This non-monotonic behavior can be traced back to the energy cut-off and therefore only has limited physical relevance. This is consistent with the Landau diamagnetism in flat Dirac systems.
- As χ^T for high temperatures, χ^0 barely shows differences between the three geometries. The results agree even quantitatively quite well, with the sphere showing a slightly higher modulus of the susceptibility in general. This comes as a surprise, as Landau levels in case of the pseudosphere even show a completely different scaling in ν for one angular branch.

5.5. De Haas-van Alphen oscillations on the pseudosphere

We have seen that the pseudosphere shows dHvA oscillations which differ enormously from those of the cone or the sphere. We assessed from the shape of the oscillations in the heatmap (Fig. 5.8) that they originate from states with positive angular quantum number m. As a first step towards understanding this special form of the dHvA effect, we want to verify this claim numerically.

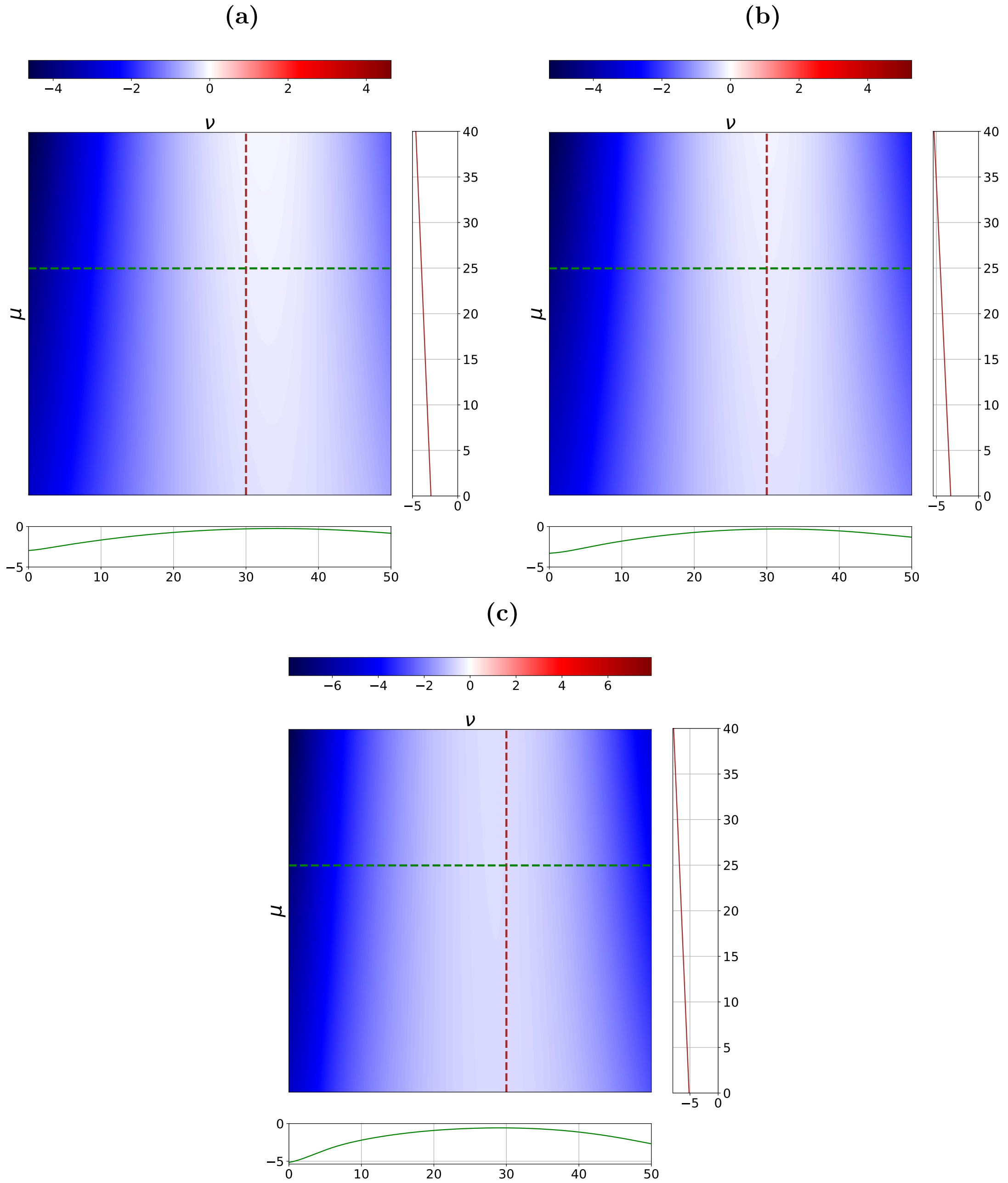

Figure 5.10: Numerically gained temperature-independent magnetic susceptibility χ^0 as a function of magnetic field ν and chemical potential μ for the pseudosphere ((a)), the cone ((b)) and the sphere ((c)). A cut-off energy of $\epsilon_C = 40$ and a cut-off temperature of $T_C = 8$ were used. Energy eigenvalues were calculated using the parameters given in Fig. 5.4, Fig. 5.5 and Fig. 5.6

.

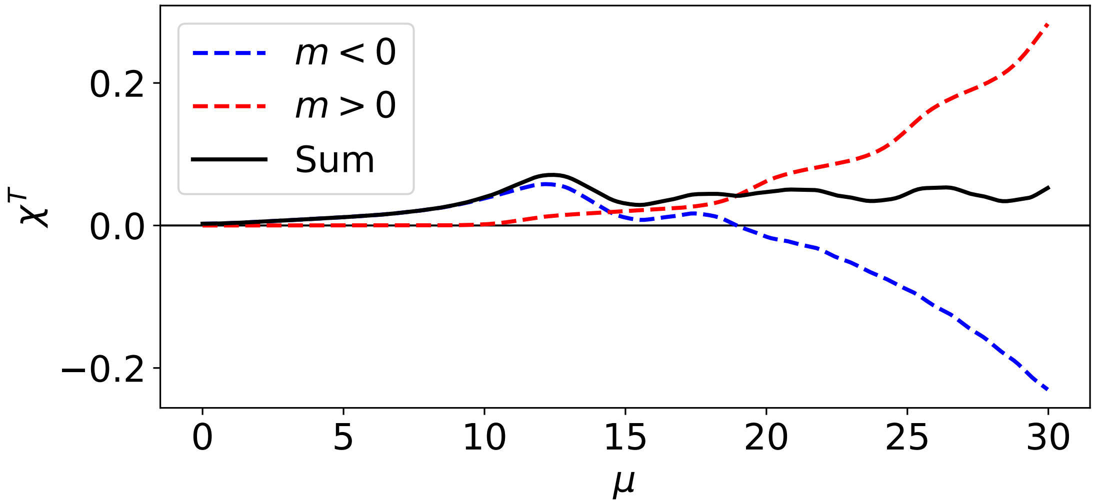

Figure 5.11: Numerically gained temperature-dependent magnetic susceptibility χ^T as a function of chemical potential μ at magnetic field $\nu = 40$ and $T = 0.5$ for the pseudosphere. The black, solid line shows the overall susceptibility, while the blue and red, dashed lines show contributions from the negative and positive angular branches, respectively. Energy eigenvalues were calculated using the parameters given in Fig. 5.4.

Fig. 5.11 shows the individual contributions from both angular branches, as well as their sum. We can immediately see that the smooth, non-oscillatory part of the susceptibility has opposite sign for the two angular branches. They even compensate each other almost totally, so that their sum, χ^T, seems to only oscillate around a constant value for larger chemical potentials. Regarding our main interest, the oscillatory part, we can observe that for small chemical potentials there are no oscillations. We have already seen this before and can attribute it to the great gap between the zeroth and higher Landau levels. From about $\mu = 10$ on, we can see an oscillation where the positive angular branch contributes to it over the whole range of chemical potential, from $\mu = 10$ on. Contrary to this, the negative angular branch only gives an oscillatory contribution in the chemical potential range from around $\mu = 10$ to $\mu = 20$. Therefore, our assumption that dHvA oscillations mainly originate from the positive angular branch was mostly correct, with the negative angular branch giving a correction, especially for the first few oscillations with respect to chemical potential.

We want to calculate this explicitly but restrict our goal to the computation of the dHvA oscillations. This means, when decomposing χ^T into a smooth and an oscillatory part, $\bar{\chi}^T$ and $\tilde{\chi}^T$ respectively, so that $\chi^T = \bar{\chi}^T + \tilde{\chi}^T$, we focus on the second mentioned term and do not care much about the first mentioned. As oscillations come mainly from the positive angular branch, we restrict our calculation to it, neglecting contributions from the negative one. Starting from Eq. (5.2), we approximate the (positive) energy levels as

$$\epsilon_{nm} = \sqrt{(4m+2)\nu + (2n+1)\sqrt{(4m+2)\nu}}\,, \tag{5.31}$$

where we label the energies by the quantum numbers $n \geq 0$ and $m \geq 0$ and neglected terms which do not depend on ν (this modified equation is exactly what we obtained from SWKB calculations (Eq. (4.54))). Without this simplification, an analytical treatment is virtually impossible. The DOS is then given by

$$\rho(\epsilon) = \sum_{m=0}^{\infty}\sum_{n=0}^{\infty} \delta\left(\epsilon - \epsilon_{nm}\right)\,. \tag{5.32}$$

It makes sense to rewrite this sum by means of Poisson summation which allows us to extract the oscillatory part explicitly. We arrive at [111]

$$\rho(\epsilon) = \sum_{k=-\infty}^{\infty}\sum_{l=-\infty}^{\infty} \rho_{kl}(\epsilon)\,, \tag{5.33}$$

with [111]

$$\rho_{kl}(\epsilon) = \int_0^\infty dm \int_0^\infty dn\, \delta\left(\epsilon - \epsilon_{nm}\right) \exp(-i2\pi(km + ln))\,. \tag{5.34}$$

We evaluate this step by step, starting with the second integral,

$$\begin{aligned} & \int_0^\infty dn\, \delta\left(\epsilon - \epsilon_{nm}\right) \exp(-i2\pi ln) \qquad (5.35) \\ = \;& (-1)^l \frac{\epsilon}{\sqrt{(4m+2)\nu}} \exp\left(-i\pi l \frac{\epsilon^2 - (4m+2)\nu}{\sqrt{(4m+2)\nu}}\right) \\ & \times\Theta\left(\epsilon - \sqrt{(4m+2)\nu + \sqrt{(4m+2)\nu}}\right)\,. \end{aligned}$$

We are left with evaluating

$$
\begin{aligned}
\rho_{kl}(\epsilon) \quad &= \quad (-1)^l \int_0^\infty dm \, \frac{\epsilon}{\sqrt{(4m+2)\nu}} \exp\left(-i\pi l \frac{\epsilon^2-(4m+2)\nu}{\sqrt{(4m+2)\nu}}\right) \\
&\quad \times \exp(-i2\pi km)\Theta\left(\epsilon - \sqrt{(4m+2)\nu + \sqrt{(4m+2)\nu}}\right) \qquad (5.36) \\
&= \quad (-1)^{l+k}\frac{\epsilon}{4\nu}\int_{2\nu}^\infty du \, \frac{1}{\sqrt{u}} \exp\left(-i\pi l \frac{\epsilon^2-u}{\sqrt{u}}\right) \\
&\quad \times \exp\left(-i\pi k\frac{u}{2\nu}\right)\Theta\left(\epsilon - \sqrt{u+\sqrt{u}}\right) \\
&= \quad (-1)^{l+k}\frac{\epsilon}{4\nu}\Theta\left(\epsilon - \sqrt{2\nu+\sqrt{2\nu}}\right) \\
&\quad \times \int_{2\nu}^{\frac{1}{4}\left(\sqrt{1+4\epsilon^2}-1\right)^2} du \, \frac{1}{\sqrt{u}} \exp\left(-i\pi l \frac{\epsilon^2-u}{\sqrt{u}}\right)\exp\left(-i\pi k\frac{u}{2\nu}\right) \\
&\overset{\nu>>1}{\approx} \quad (-1)^{l+k}\frac{\epsilon}{4\nu}\Theta\left(\epsilon - \sqrt{2\nu}\right) \\
&\quad \times \int_{2\nu}^{\epsilon^2} du \, \frac{1}{\sqrt{u}} \exp\left(-i\pi l \frac{\epsilon^2-u}{\sqrt{u}}\right)\exp\left(-i\pi k\frac{u}{2\nu}\right) \\
&= \quad (-1)^{l+k}\frac{\epsilon}{2\nu}\Theta\left(\epsilon - \sqrt{2\nu}\right) \\
&\quad \times \int_{\sqrt{2\nu}}^{\epsilon} dt \, \exp\left(-i\pi l \frac{\epsilon^2-t^2}{t}\right)\exp\left(-i\pi k\frac{t^2}{2\nu}\right) \\
&\overset{\epsilon>>\sqrt{2\nu}}{\approx} \quad (-1)^{l+k}\frac{\epsilon}{2\nu}\Theta(\epsilon)\int_0^\epsilon dt \, \exp\left(-i\pi l \frac{\epsilon^2-t^2}{t}\right)\exp\left(-i\pi k\frac{t^2}{2\nu}\right) ,
\end{aligned}
$$

which is very hard to solve for general k and l. To proceed, we have to determine which components are dominant. When considering Poisson summation as a kind of Fourier decomposition, the term ρ_{00} represents the non-oscillatory, mean DOS. ρ_{k0}, with $k \neq 0$, are the oscillatory components which come from the discrete level structure due to the angular quantum number m. Contrary to this, ρ_{0l}, with $l \neq 0$, corresponds to the oscillatory components originating from the discrete level structure due to the main quantum number n. The remaining components, ρ_{kl}, with $k \neq 0$ and $l \neq 0$, are oscillatory components due to the discreteness of both, m and n. As explained above, our main scope is to find the terms responsible for dHvA oscillations. We found above that for large magnetic field, the main level structure and therefore magnetooscillations come from m, with all levels being degenerate in n in the limit $\nu \to \infty$ (see Eq. (5.2)). Therefore, the level spacing between eigenstates with identical m but adjacent n is much smaller than vice versa and the discreteness of n can assumed to be washed out due to thermal smoothing. We can conclude that the contribution of the Poisson sum, which is mainly responsible for dHvA, is ρ_{k0}, with $k \neq 0$. These terms keep the discreteness of m but integrate over a continuous n.

5.5.1. Calculation of ρ_{00}

For completeness, we also want to evaluate the smooth term ρ_{00}, which reads

$$\begin{aligned}\rho_{00}(\epsilon) &= \frac{\epsilon}{2\nu}\Theta(\epsilon)\int_0^\epsilon dt \\ &= \frac{\epsilon^2}{2\nu}\Theta(\epsilon)\,.\end{aligned} \tag{5.37}$$

The Laplace transform of it is given by

$$\begin{aligned}\rho_{00}(s) &= \int_{-\infty}^{\infty} dE\,\rho_{00}(E)\exp(-Es) \\ &= \frac{1}{2\nu}\int_0^\infty dE\,E^2\exp(-Es) \\ &= \frac{1}{\nu s^3}\,,\end{aligned} \tag{5.38}$$

where the region of convergence is clearly $\sigma > 0$. To proceed, we need to integrate this twice, which can be done very easily in Laplace space (multiplying twice with $1/s$), yielding

$$\mathcal{N}_{00}(s) = \frac{1}{\nu s^5}\,. \tag{5.39}$$

The smooth part of the temperature-dependent grand canonical potential can then be written as

$$\begin{aligned}\Omega_{00}^T(T,\nu,\mu) &= -\frac{1}{\pi i}\int_{\sigma-i\infty}^{\sigma+i\infty} ds\,\frac{1}{\nu(-s)^5}\frac{\pi T s}{\sin(\pi T s)}\cosh(\mu s) \\ &= +\frac{1}{2\pi i}\int_{\sigma-i\infty}^{\sigma+i\infty} ds\,\frac{1}{\nu s^5}\frac{\pi T s}{\sin(\pi T s)}\exp(\mu s) \\ &\quad +\frac{1}{2\pi i}\int_{\sigma-i\infty}^{\sigma+i\infty} ds\,\frac{1}{\nu s^5}\frac{\pi T s}{\sin(\pi T s)}\exp(-\mu s) \\ &=: +\frac{1}{2\pi i}\int_{\sigma-i\infty}^{\sigma+i\infty} ds\,\left(G_+(s)+G_-(s)\right)\,,\end{aligned} \tag{5.40}$$

where the region of convergence is now (according to the bilateral Laplace cross-correlation theorem [105]) $-1/T < \sigma < 0^-$ and we defined $G_\pm(s)$. We can solve this using the residue theorem but have to evaluate either of the terms on their own, as the integration contour has to be chosen differently. For the first term, it has to be closed to the left, whereas for the second one it has to be closed to the right. $G_\pm(s)$ have poles of order five at $s = 0$ and of order one at $s = j/T$ for $j \in \mathbb{Z}\backslash\{0\}$.

Fig. 5.12 illustrates the integration contours used, as well as the pole structures.

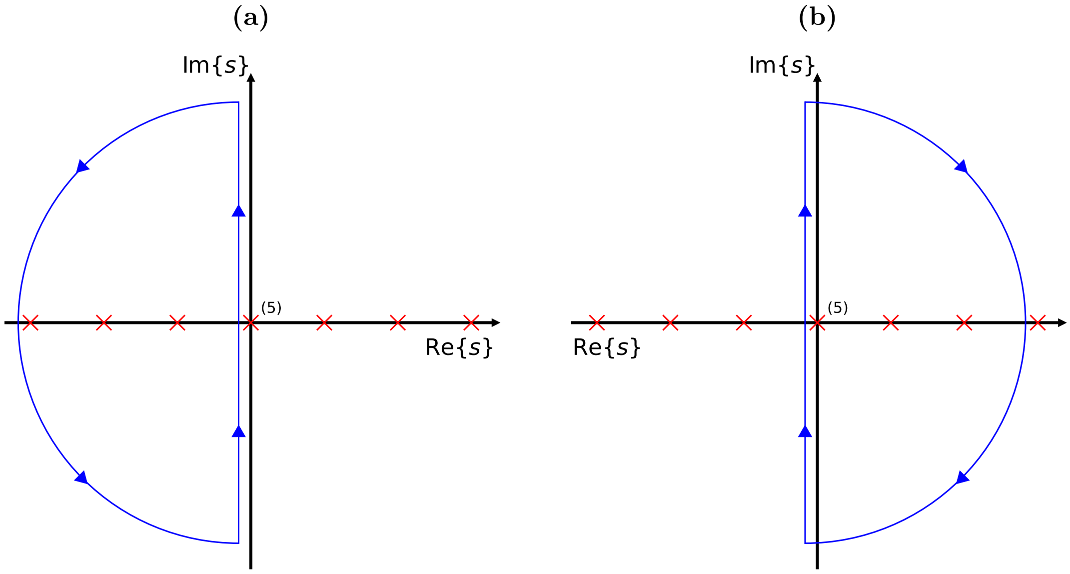

Figure 5.12: Contour (blue) for evaluation of the integrals over $G_+(s)$ ((a)) and $G_-(s)$ ((b)), as well as poles (red) of $G_\pm(s)$. The radius of the half circle goes to infinity in the real calculation. A finite radius was only chosen for the sake of illustration.

Applying the residue theorem yields

$$\begin{aligned}
\Omega_{00}^T(T,\nu,\mu) &= -\operatorname*{Res}_{s=0}\{G_-(s)\} \\
&\quad -\sum_{j=1}^{\infty}\operatorname*{Res}_{s=\frac{j}{T}}\{G_-(s)\}+\sum_{j=1}^{\infty}\operatorname*{Res}_{s=-\frac{j}{T}}\{G_+(s)\} \\
&\overset{[112]}{=} -\frac{1}{\nu}\left(\frac{7\pi^4}{360}T^4+\frac{\pi^2}{12}T^2\mu^2+\frac{1}{24}\mu^4\right) \\
&\quad -\sum_{j=1}^{\infty}(-1)^j\frac{T^4}{\nu j^4}\exp\left(-\mu\frac{j}{T}\right) \\
&\quad +\sum_{j=1}^{\infty}(-1)^j\frac{T^4}{\nu j^4}\exp\left(-\mu\frac{j}{T}\right) \\
&= -\frac{1}{\nu}\left(\frac{7\pi^4}{360}T^4+\frac{\pi^2}{12}T^2\mu^2+\frac{1}{24}\mu^4\right).
\end{aligned} \tag{5.41}$$

The corresponding susceptibility is simply given

$$\begin{aligned}
\chi_{00}^T &= -\frac{\partial^2\Omega_{00}^T}{\partial\nu^2} \\
&= \frac{1}{\nu^3}\left(\frac{7\pi^4}{180}T^4+\frac{\pi^2}{6}T^2\mu^2+\frac{1}{12}\mu^4\right).
\end{aligned} \tag{5.42}$$

We see that the main, smooth contribution to the susceptibility from $m > 0$ states is paramagnetic and rising for increasing chemical potential μ. This perfectly aligns with what we saw in Fig. 5.11.

5.5.2. Calculation of ρ_{k0}

Now we come to the more important part, ρ_{k0}, with $k \neq 0$. It is most convenient to evaluate terms with opposite k simultaneously, yielding

$$\begin{aligned}
\rho_{|k|0}(\epsilon) &:= \rho_{k0}(\epsilon) + \rho_{-k0}(\epsilon) \\
&= (-1)^k \frac{\epsilon}{\nu} \Theta(\epsilon) \int_0^{\epsilon} dt \cos\left(\pi k \frac{t^2}{2\nu}\right) \\
&= (-1)^k \frac{\epsilon}{\nu} \Theta(\epsilon) \sqrt{\frac{\nu}{k}} \int_0^{\sqrt{\frac{k}{\nu}}\epsilon} dt \cos\left(\frac{\pi}{2} t^2\right) \\
&= (-1)^k \frac{\epsilon}{\sqrt{k\nu}} \mathrm{C}\left(\sqrt{\frac{k}{\nu}}\epsilon\right) \Theta(\epsilon) ,
\end{aligned} \tag{5.43}$$

where $\mathrm{C}(x)$ is the *Cosine Fresnel integral* [98]. Even though the Laplace transform of $\mathrm{C}(x)$ is an entire function, it has a very strong divergence at infinity when going along some lines in the complex plane. Therefore, the residue method to calculate the inverse Laplace transform cannot be used in its simple form and the whole method becomes impractical. We therefore proceed in energy space and as a first step need to integrate two times, giving

$$\begin{aligned}
\mathcal{N}_{|k|0}(\epsilon) &= \int_0^{\epsilon} d\epsilon' \int_0^{\epsilon'} d\epsilon'' \, (-1)^k \frac{\epsilon''}{\sqrt{k\nu}} \mathrm{C}\left(\sqrt{\frac{k}{\nu}}\epsilon''\right) \\
&\overset{[98]}{=} +(-1)^k \frac{1}{\sqrt{k\nu}} \left[\frac{\epsilon^3}{6} \mathrm{C}\left(\sqrt{\frac{k}{\nu}}\epsilon\right) + \frac{\nu\epsilon}{2\pi k} \mathrm{S}\left(\sqrt{\frac{k}{\nu}}\epsilon\right)\right] \\
&\quad +(-1)^k \frac{1}{\sqrt{k\nu}} \left[-\frac{\epsilon^2}{6\pi}\sqrt{\frac{\nu}{k}} \sin\left(\frac{\pi k}{2\nu}\epsilon^2\right)\right] \\
&\quad +(-1)^k \frac{1}{\sqrt{k\nu}} \left[\frac{2}{3\pi^2}\sqrt{\frac{\nu^3}{k^3}} \cos\left(\frac{\pi k}{2\nu}\epsilon^2\right) - \frac{2}{3\pi^2}\sqrt{\frac{\nu^3}{k^3}}\right] ,
\end{aligned} \tag{5.44}$$

where $\mathrm{S}(x)$ is the *Sine Fresnel integral* [98] and we omit the Heaviside function from now on, knowing that $\rho(E)$ (as we defined it) is zero for negative energy. Both functions, $\mathrm{C}(x)$ and $\mathrm{S}(x)$ oscillate around the mean value of $1/2$ for big arguments [98]. Following [70], it makes sense to decompose them into this mean value and a purely oscillating part. Defining $\tilde{\mathrm{C}}(x) = \mathrm{C}(x) - 1/2$ [70] and $\tilde{\mathrm{S}}(x) = \mathrm{S}(x) - 1/2$ [70], this yields

$$\begin{aligned}
\mathcal{N}_{|k|0}(\epsilon) &= +(-1)^k \frac{1}{\sqrt{k\nu}} \left[\frac{\epsilon^3}{12} + \frac{\nu\epsilon}{4\pi k} - \frac{2}{3\pi^2}\sqrt{\frac{\nu^3}{k^3}} \right] \\
&\quad +(-1)^k \frac{1}{\sqrt{k\nu}} \left[\frac{\epsilon^3}{6} \tilde{\mathrm{C}}\left(\sqrt{\frac{k}{\nu}}\epsilon\right) + \frac{\nu\epsilon}{2\pi k} \tilde{\mathrm{S}}\left(\sqrt{\frac{k}{\nu}}\epsilon\right) \right] \\
&\quad +(-1)^k \frac{1}{\sqrt{k\nu}} \left[-\frac{\epsilon^2}{6\pi}\sqrt{\frac{\nu}{k}} \sin\left(\frac{\pi k}{2\nu}\epsilon^2\right) \right] \\
&\quad +(-1)^k \frac{1}{\sqrt{k\nu}} \left[\frac{2}{3\pi^2}\sqrt{\frac{\nu^3}{k^3}} \cos\left(\frac{\pi k}{2\nu}\epsilon^2\right) \right] \\
&= \bar{\mathcal{N}}_{|k|0}(\epsilon) + \tilde{\mathcal{N}}_{|k|0}(\epsilon)\,,
\end{aligned} \tag{5.45}$$

where we decomposed the quantity into a smooth and an oscillating part, $\bar{\mathcal{N}}_{|k|0}(\epsilon)$ and $\tilde{\mathcal{N}}_{|k|0}(\epsilon)$. Again, the second mentioned contribution is responsible for dHvA but we also evaluate the first one for completeness. We are now in the position to treat the smooth part with the Laplace method. Its transform reads

$$\begin{aligned}
\bar{\mathcal{N}}_{|k|0}(s) &= \int_0^\infty d\epsilon\, \bar{\mathcal{N}}_{|k|0}(\epsilon) \exp(-\epsilon s) \\
&= (-1)^k \frac{1}{\sqrt{k\nu}} \int_0^\infty d\epsilon \left[\frac{\epsilon^3}{12} + \frac{\nu\epsilon}{4\pi k} - \frac{2}{3\pi^2}\sqrt{\frac{\nu^3}{k^3}} \right] \exp(-\epsilon s) \\
&= (-1)^k \left[\frac{1}{2\sqrt{k\nu}} \frac{1}{s^4} + \frac{\sqrt{\nu}}{4\pi k^{\frac{3}{2}}} \frac{1}{s^2} - \frac{2}{3\pi^2}\sqrt{\frac{\nu^3}{k^3}} \frac{1}{s} \right] .
\end{aligned} \tag{5.46}$$

The contribution of it to the grand canonical potential can be written as

$$\begin{aligned}
\bar{\Omega}^T_{|k|0}(T,\nu,\mu) &= -\frac{1}{\pi i}(-1)^k \int_{\sigma-i\infty}^{\sigma+i\infty} ds \left[\frac{1}{2\sqrt{k\nu}} \frac{1}{s^4} + \frac{\sqrt{\nu}}{4\pi k^{\frac{3}{2}}} \frac{1}{s^2} + \frac{2}{3\pi^2}\sqrt{\frac{\nu^3}{k^3}} \frac{1}{s} \right] \\
&\quad \times \frac{\pi T s}{\sin(\pi T s)} \cosh(\mu s)\,,
\end{aligned} \tag{5.47}$$

which can be evaluated with the same technique as in the previous calculation. The result reads [112]

$$\begin{aligned}
\bar{\Omega}^T_{|k|0}(T,\nu,\mu) &= -(-1)^k \left[\frac{\pi^2 T^2 \mu}{12\sqrt{k\nu}} + \frac{\mu\sqrt{\nu}}{4\pi k^{\frac{3}{2}}} + \frac{\mu^3}{12\sqrt{k\nu}} - \frac{2}{3\pi^2}\sqrt{\frac{\nu^3}{k^3}} \right] \\
&\quad +(-1)^k \sum_{j=1}^\infty (-1)^j \left[\frac{T^3}{j^3\sqrt{k\nu}} + \frac{T\sqrt{\nu}}{2\pi j k^{\frac{3}{2}}} \right] \exp\left(-\frac{\mu j}{T}\right) \\
&\overset{[98]}{=} -(-1)^k \left[\frac{\pi^2 T^2 \mu}{12\sqrt{k\nu}} + \frac{\mu\sqrt{\nu}}{4\pi k^{\frac{3}{2}}} + \frac{\mu^3}{12\sqrt{k\nu}} - \frac{2}{3\pi^2}\sqrt{\frac{\nu^3}{k^3}} \right] \\
&\quad -(-1)^k \left[\frac{T^3}{\sqrt{k\nu}} \mathrm{F}_2\left(-\frac{\mu}{T}\right) + \frac{T\sqrt{\nu}}{2\pi k^{\frac{3}{2}}} \mathrm{F}_0\left(-\frac{\mu}{T}\right) \right] ,
\end{aligned} \tag{5.48}$$

where $\mathrm{F}_j(x)$ are *Fermi-Dirac integrals* [98]. This gives rise to the susceptibility

$$\begin{aligned}\bar{\chi}^T_{|k|0}(T,\nu,\mu) &= +(-1)^k\left[\frac{\pi^2T^2\mu}{16k^{\frac{1}{2}}\nu^{\frac{5}{2}}}-\frac{\mu}{16\pi k^{\frac{3}{2}}\nu^{\frac{3}{2}}}+\frac{\mu^3}{16k^{\frac{1}{2}}\nu^{\frac{5}{2}}}-\frac{1}{2\pi^2k^{\frac{3}{2}}\nu^{\frac{1}{2}}}\right] \\ &\quad +(-1)^k\left[\frac{3T^3}{4k^{\frac{1}{2}}\nu^{\frac{5}{2}}}\mathrm{F}_2\left(-\frac{\mu}{T}\right)-\frac{T\sqrt{\nu}}{8\pi k^{\frac{3}{2}}\nu^{\frac{3}{2}}}\mathrm{F}_0\left(-\frac{\mu}{T}\right)\right].\end{aligned} \tag{5.49}$$

The oscillating contribution to the grand canonical potential can be approximated as shown in Appendix A.7. This yields

$$\begin{aligned}\tilde{\Omega}^T_{|k|0}(T,\nu,\mu) &= -(-1)^k\frac{\pi^2T}{\sinh\left(\frac{\pi^2Tk\mu}{\nu}\right)}\left[\frac{k^{\frac{1}{2}}\mu^4}{6\nu^{\frac{3}{2}}}\tilde{\mathrm{C}}\left(\sqrt{\frac{k}{\nu}}\mu\right)+\frac{\mu^2}{2\pi k^{\frac{1}{2}}\nu^{\frac{1}{2}}}\tilde{\mathrm{S}}\left(\sqrt{\frac{k}{\nu}}\mu\right)\right] \\ &\quad +(-1)^k\frac{\pi T}{\sinh\left(\frac{\pi^2Tk\mu}{\nu}\right)}\left[\frac{\mu^3}{6\nu}\sin\left(\frac{\pi k}{2\nu}\mu^2\right)-\frac{2\mu}{3\pi k}\cos\left(\frac{\pi k}{2\nu}\mu^2\right)\right].\end{aligned} \tag{5.50}$$

We can approximate the second derivative of this by assuming that the sinh term remains almost constant in the region of interest and therefore its derivative can be neglected [70]. This yields [112]

$$\begin{aligned}\tilde{\chi}^T_{|k|0}(T,\nu,\mu) &\approx +(-1)^k\frac{\pi T}{\sinh\left(\frac{\pi^2Tk\mu}{\nu}\right)}\left[\frac{5\pi k^{\frac{1}{2}}\mu^4}{8\nu^{\frac{7}{2}}}\tilde{\mathrm{C}}\left(\sqrt{\frac{k}{\nu}}\mu\right)\right] \\ &\quad +(-1)^k\frac{\pi T}{\sinh\left(\frac{\pi^2Tk\mu}{\nu}\right)}\left[\frac{3\mu^2}{8k^{\frac{1}{2}}\nu^{\frac{5}{2}}}\tilde{\mathrm{S}}\left(\sqrt{\frac{k}{\nu}}\mu\right)\right] \\ &\quad -(-1)^k\frac{\pi T}{\sinh\left(\frac{\pi^2Tk\mu}{\nu}\right)}\left[\frac{3\mu^3}{8\nu^3}\sin\left(\frac{\pi}{2}\frac{k\mu^2}{\nu}\right)\right] \\ &\approx +(-1)^k\frac{\pi T}{\sinh\left(\frac{\pi^2Tk\mu}{\nu}\right)}\left[\frac{5\pi k^{\frac{1}{2}}\mu^4}{8\nu^{\frac{7}{2}}}\tilde{\mathrm{C}}\left(\sqrt{\frac{k}{\nu}}\mu\right)\right] \\ &\quad -(-1)^k\frac{\pi T}{\sinh\left(\frac{\pi^2Tk\mu}{\nu}\right)}\left[\frac{3\mu^3}{8\nu^3}\sin\left(\frac{\pi}{2}\frac{k\mu^2}{\nu}\right)\right] \\ &\approx +(-1)^k\frac{\pi T}{\sinh\left(\frac{\pi^2Tk\mu}{\nu}\right)}\left[\frac{5\mu^3}{8\nu^3}\sin\left(\frac{\pi}{2}\frac{k\mu^2}{\nu}\right)\right] \\ &\quad -(-1)^k\frac{\pi T}{\sinh\left(\frac{\pi^2Tk\mu}{\nu}\right)}\left[\frac{3\mu^3}{8\nu^3}\sin\left(\frac{\pi}{2}\frac{k\mu^2}{\nu}\right)\right] \\ &= +(-1)^k\frac{\pi T}{\sinh\left(\frac{\pi^2Tk\mu}{\nu}\right)}\left[\frac{\mu^3}{4\nu^3}\sin\left(\frac{\pi}{2}\frac{k\mu^2}{\nu}\right)\right].\end{aligned} \tag{5.51}$$

5.5.3. Final results

For completeness, we also collect the non-oscillatory parts of the susceptibility obtained in the previous paragraphs. As we have seen, not only ρ_{00} but also ρ_{k0} give smooth contributions. Since we have not evaluated ρ_{0l} and ρ_{kl}, we cannot be sure that we have captured all the relevant contributions. Therefore, this result has to be treated with caution and should only be seen as an intermediate step. We sum up the smooth parts, yielding

$$
\begin{aligned}
\bar{\chi}^T \quad &\approx \quad \chi_{00}^T + \sum_{k=1}^{\infty} \bar{\chi}_{|k|0}^T \\
&= \quad + \frac{1}{\nu^3}\left(\frac{7\pi^4}{180}T^4 + \frac{\pi^2}{6}T^2\mu^2 + \frac{1}{12}\mu^4\right) \\
&\quad\quad + \sum_{k=1}^{\infty}(-1)^k\left[\frac{\pi^2T^2\mu}{16k^{\frac{1}{2}}\nu^{\frac{5}{2}}} - \frac{\mu}{16\pi k^{\frac{3}{2}}\nu^{\frac{3}{2}}} + \frac{\mu^3}{16k^{\frac{1}{2}}\nu^{\frac{5}{2}}} - \frac{1}{2\pi^2k^{\frac{3}{2}}\nu^{\frac{1}{2}}}\right] \\
&\quad\quad + \sum_{k=1}^{\infty}(-1)^k\left[\frac{3T^3}{4k^{\frac{1}{2}}\nu^{\frac{5}{2}}}\mathrm{F}_2\left(-\frac{\mu}{T}\right) - \frac{T\sqrt{\nu}}{8\pi k^{\frac{3}{2}}\nu^{\frac{3}{2}}}\mathrm{F}_0\left(-\frac{\mu}{T}\right)\right] \\
&\overset{\mu>>T}{\approx} \quad + \frac{1}{\nu^3}\left(\frac{7\pi^4}{180}T^4 + \frac{\pi^2}{6}T^2\mu^2 + \frac{1}{12}\mu^4\right) \\
&\quad\quad + \sum_{k=1}^{\infty}(-1)^k\left[\frac{\pi^2T^2\mu}{16k^{\frac{1}{2}}\nu^{\frac{5}{2}}} - \frac{\mu}{16\pi k^{\frac{3}{2}}\nu^{\frac{3}{2}}} + \frac{\mu^3}{16k^{\frac{1}{2}}\nu^{\frac{5}{2}}} - \frac{1}{2\pi^2k^{\frac{3}{2}}\nu^{\frac{1}{2}}}\right] \\
&\overset{[113]}{=} \quad + \frac{1}{\nu^3}\left(\frac{7\pi^4}{180}T^4 + \frac{\pi^2}{6}T^2\mu^2 + \frac{1}{12}\mu^4\right) \\
&\quad\quad - \eta\left(\frac{1}{2}\right)\left(\frac{\pi^2T^2\mu}{16\nu^{\frac{5}{2}}} + \frac{\mu^3}{16\nu^{\frac{5}{2}}}\right) + \eta\left(\frac{3}{2}\right)\left(\frac{\mu}{16\pi\nu^{\frac{3}{2}}} + \frac{1}{2\pi^2\nu^{\frac{1}{2}}}\right),
\end{aligned}
\tag{5.52}
$$

where we evaluated the sums using the *Dirichlet eta function* $\eta(x)$ [113].

Let us now turn to the more important oscillatory part which reads

$$
\begin{aligned}
\tilde{\chi}^T \quad &\approx \quad \frac{\mu^3}{4\nu^3}\sum_{k=1}^{\infty}(-1)^k\frac{\pi T}{\sinh\left(\frac{\pi^2 kT\mu}{\nu}\right)}\sin\left(\frac{\pi}{2}\frac{k\mu^2}{\nu}\right) \\
&= \quad \frac{\mu^2}{4\pi\nu^2}\sum_{k=1}^{\infty}(-1)^k\frac{1}{k}R_T\left(\frac{\pi k\mu}{\nu}\right)\sin\left(\frac{\pi}{2}\frac{k\mu^2}{\nu}\right),
\end{aligned}
\tag{5.53}
$$

where we conveniently used the temperature damping factor $R_T(x) = \pi Tx/\sinh(\pi Tx)$ [70, 104].

Fig. 5.13 shows a comparison between the numerical result of χ^T and our calculated $\tilde{\chi}^T$, which was appropriately shifted manually, as we have not computed the offset explicitly. A very good match in the region between $\mu = 15$ and $\mu = 30$ can be observed. As we found out before, the oscillations around $\mu = 10$ are mostly caused by the levels

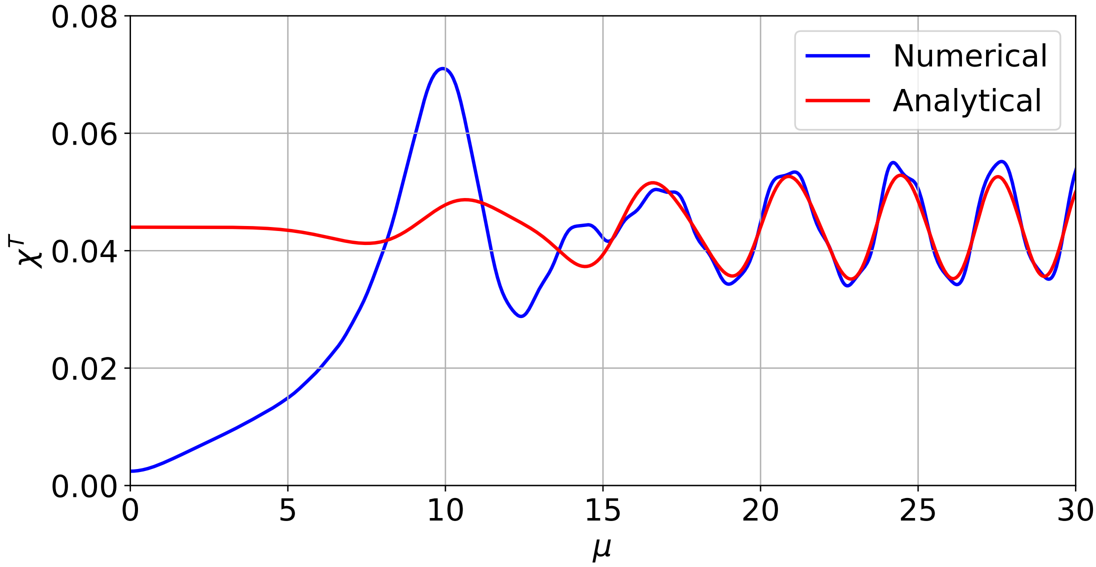

Figure 5.13: Numerically gained temperature-dependent magnetic susceptibility χ^T as a function of chemical potential μ at magnetic field $\nu = 40$ and $T = 0.5$ for the pseudosphere (blue line). Energy eigenvalues were calculated using the parameters given in Fig. 5.4. Analytically gained $\tilde{\chi}^T$ (Eq. (5.53)) which was properly shifted to the numerical result (red line). The same parameters as for the numerical solution were used.

with negative angular quantum number. The deviation between the numerical results and our calculation was therefore expected.

We want to compare this result to the dHvA oscillations of massless Dirac electrons on a flat plane. Let us rewrite the relevant susceptibilities (Eq. (5.29) for the plane and Eq. (5.53) for the pseudosphere) for the sake of clarity,

$$\chi_{plane}^{dHvA} = \frac{1}{2\sqrt{\pi}} \frac{\mu^3}{\nu^2} \sum_{k=1}^{\infty} R_T \left(\frac{\pi k \mu}{\nu} \right) \cos \left(\frac{\pi}{2} \frac{k\mu^2}{\nu} \right) , \tag{5.54}$$

$$\chi_{pseudo}^{dHvA} = \frac{\mu^2}{4\pi\nu^2} \sum_{k=1}^{\infty} (-1)^k \frac{1}{k} R_T \left(\frac{\pi k \mu}{\nu} \right) \sin \left(\frac{\pi}{2} \frac{k\mu^2}{\nu} \right) . \tag{5.55}$$

When looking at the two equations, we note that they share the same structure. Both have the form of a Fourier series with oscillations which are periodic (with modulated amplitude) in μ^2 and $1/\nu$. The temperature damping enters the equations identically. The chemical potential appears in the numerator of the amplitude terms, while the magnetic field appears in the denominator. Despite these similarities, we can also note import differences in three important details.

First of all, the amplitude in case of the plane has a larger prefactor ($1/(2\sqrt{\pi})$ compared to $1/(4\pi)$) and furthermore scales with μ^3 compared to μ^2 in case of the pseudosphere. Let us recall that dHvA oscillations appear in a regime of large μ, so that this leads to a drastically higher amplitude in case of the flat plane compared to the pseudosphere. This can be explained very well when looking at the Landau spectrum. While the levels are highly degenerate in case of the flat system, none of them is degenerate at all in case of the pseudosphere. We even found in this section that the relevant part of the DOS can be obtained by integrating out the main quantum number n. When comparing the remaining DOS to the one for the plane, we find a continuous, oscillating function in the first case compared to a series of sharp peaks in the second one. Therefore, intrinsically, equal temperature smoothes the grand canonical potential in case of the pseudosphere much more, yielding dHvA oscillations with smaller amplitude.

Second, the shape of the oscillations is different. While the temperature damping term $R_T(x)$ with the Fourier index k in its argument appears in both expressions, ensuring convergence of the respective series, the pseudosphere shows an additional $1/k$ damping term. This extra term attenuates higher harmonics and leads to a more sinusoidal form of the oscillation.

Finally, both terms show different phases. When assuming that the $k = 1$ term is the dominant one in both expressions, we can see that the phase shift between them is $\pi/2$. Peaks in susceptibility occur at $\mu = \sqrt{4q\nu}, q \in \mathbb{N}$ in case of the plane (which exactly coincides with the position of its Landau levels in energy) and at $\mu = \sqrt{4(q+1)\nu}, q \in \mathbb{N}$ in case of the pseudosphere. The latter does not coincide with any Landau level at all which makes it a highly non-trivial result.

We can conclude that the dHvA oscillations of the pseudosphere and the conventional, flat plane differ in all three important, characteristic properties, the amplitude, the shape and the phase.

6. Conclusion and outlook

To conclude this thesis, we want to summarize what was achieved, which knowledge gaps have been closed and which further directions could be interesting in future research efforts.

Overall, we focused on Dirac Landau levels for curved surfaces of revolution. Contrary to the overall perpendicular field, which is assumed in most research works covering this field, our main scope was the experimentally much more relevant case of a coaxial field.

We established the massless Dirac and Schrödinger Hamiltonians for curved surfaces of revolution which are subject to a magnetic field. We found that the 3D vector potential in the symmetric gauge describing the magnetic field in ambient space can directly be used in the 2D model.

Using the *Schrödinger-Lichnerowicz theorem*, we verified that for an overall perpendicular magnetic field and a surface with constant Gaussian curvature, the spectra of the Dirac and Schrödinger Hamiltonians are directly linked to each other by an algebraic relation. If one finds the Schrödinger Landau spectrum for a particular geometry, the Dirac Landau spectrum follows immediately and vice versa. There is no need to solve another differential equation.

We described the supersymmetric structure of the problem and could make predictions of the structure of the eigenstates of the Dirac Hamiltonian without assuming a particular geometry. The number of nodes of each spinor component is determined by the main quantum number n, as well as the existence of a zero energy mode.

As a first example, we applied our developed machinery on the problem of finding Dirac Landau levels for the pseudosphere. Energies in case of the overall perpendicular magnetic field have already been known from a more general, mathematical theory and also been confirmed by the author of this thesis in his Master project [76] using a power series ansatz. This was complemented in this thesis using two different methods, an analytical one by noticing that the differential equation to solve leads to *Laguerre polynomials* and an algebraic one exploiting SUSY and shape invariance of the effective potential. All methods leads to the same spectrum. We also found closed expressions of the corresponding eigenstates. Analytical findings have been verified by numerical calculations which can be found in [27].

The experimentally more important case of the coaxial magnetic field has also been treated. We succeeded in finding the Dirac Landau level spectrum using two different, asymptotic methods based on the assumption of a large magnetic field. First of all, we used asymptotic solutions for the underlying differential equation (*DCHE*) and second the SWKB approximation. They only differ in subleading terms, with the first mentioned going one order further. Most notably, the higher Landau levels are not only non-degenerate in the angular quantum number m anymore but also show a different energy scaling as a function of magnetic field B depending on the signs of m and B. For equal signs, the scaling is the same as one would expect for Dirac Landau levels on a flat plane ($\propto B^{1/2}$), while for opposite signs, we find a very unconventional scaling of $\propto B^{1/4}$. The lifted degeneracy can be attributed to the non-constant magnitude of the projection of the magnetic field onto the surface normal, yielding different, arclength dependent, effective field strengths on the surface. The zeroth Landau level remains highly degenerate which can be attributed to the topological protection of this mode in the context of the index theorem [94]. Numerical calculations confirmed our analytical findings and confirmed our prediction of the eigenstate structure based on SUSY.

We extended our SWKB calculations to a general class of surfaces which contains the pseudosphere and the cone, subject to a coaxial field. Using this, we proofed a scaling law of the Landau level energies as a function of magnetic field which depends on a geometrical parameter. This was first formulated as a conjecture in [77]. This result can be seen as a generalization of the calculation for the pseudosphere. Again, degeneracy of higher Landau levels is lifted and the energy of one angular branch scales with $\propto B^{1/2}$, while the other one shows a scaling exponent which depends on the geometrical parameter. Numerical calculations again confirmed our approach, as well as the eigenstate structure predicted by SUSY.

Complementary to the integral quantity of energy, we also found a general formula for the local quantity of current density in the azimuthal direction and the magnetic dipole moment caused by it. For the case of the reciprocal cone, we found counterpropagating persistent currents for a state which explains its zero magnetic dipole moment, as well as its energy being independent of the magnetic field.

In the second part of the thesis, we focused on the magnetic susceptibility caused by the response of the charge carriers to the external, coaxial magnetic field. We computed the Dirac spectrum of the pseudosphere in the total absence of a magnetic field using SWKB. We further recovered the Zeeman effect for the spectrum in case of weak magnetic fields which holds for general surfaces. More interestingly, a correction term appears, which originates from the coupling of the gauge field to the curved geometry.

We numerically studied the susceptibility for three surfaces with constant Gaussian curvature, the pseudosphere, the cone and the (half) sphere. All of them show very similar features with the exception of the dHvA effect which differs in amplitude, phase and shape, depending on the particular geometry. For the case of the pseudosphere, we explicitly calculated this effect and found a very good matching with numerical results within the region of interest. We quantitatively compared our final result for the dHvA susceptibility of the pseudosphere to that of a flat plane and could confirm our numerical findings.

Overall, we strengthened the research field by focusing on the experimentally relevant coaxial field, thereby providing approximate Landau level spectra for a large class of surfaces in the strong field regime, clarifying the general structure of Landau states on curved surfaces, finding a geometric correction to the Zeeman splitting in the weak field regime, as well as discovering highly geometry-distinctive de Haas-van Alphen signatures in the magnetic susceptibilities.

Despite the progress made in this thesis, a few questions remain open:

- A major limitation of the model in this thesis is that we neglected Zeeman coupling. Are there substantial changes when taking it into account?
- What is the reason of the multiple level crossings in the overall spectrum of the cone?
- The dHvA oscillations on the sphere have a very peculiar form, even though Landau levels are degenerate in the high field limit. What is the reason for this and can it be computed analytically?
- We saw "fingers" (regions with reduced intensity) in the heatmaps of the temperature-dependent susceptibilities. What are the reasons for their appearance?
- The temperature-independent susceptibilities, as well as the temperature-dependent susceptibilities in the high temperature regime, of the pseudosphere, cone and (half) sphere are almost identical. This suggests a universal form of the smoothed DOS for all chemical potentials μ and magnetic fields B, independent of the particular geometry. Can one prove this for general surfaces?
- We saw that the smooth contributions of both angular branches to the temperature-dependent susceptibility of the pseudosphere exactly cancel each other in the moderate temperature regime. This is surprising since both branches have a different energy scaling with respect to magnetic field ($\propto B^{1/2}$ vs $\propto B^{1/4}$). What is the reason for the exact cancellation?
- When calculating dHvA oscillations for the pseudosphere analytically and comparing the results to those for the flat plane, we noticed the same structure but found differences in amplitude, phase and shape. In general, magnetooscillations are described by the *Lifshitz-Kosevich formula* [114–116]. Is it possible for general surfaces to extend it by a factor accounting for the geometric influence on the oscillations, e.g. a geometric form and damping factor R_G, as well as a geometric phase shift φ_G?
- Another interesting observable to study is the angular momentum itself. Theoretical works about the QHE of non-relativistic electrons on curved surfaces hint at an intensive excess term which is a fraction of the angular momentum quantum [117]. Does this phenomenon also appear for massless Dirac electrons?

Finally, let us summarize that geometry offers an additional degree of freedom to tune physical properties of massless Dirac systems in condensed matter. It is fascinating to see, how curved geometry can alter fundamental properties of the system, like the Landau level scaling. This has wide ranging implications on the observables of the system, with only a part of them being known at the moment.

A. Appendix

A.1. Christoffel symbols

We need to calculate the Christoffel symbols of the metric tensor. Let us recall that

$$\boldsymbol{g} = dx^l \otimes dx^l + r^2(l)\, dx^\phi \otimes dx^\phi \,. \tag{A.1}$$

Following [28], we define the Lagrange function

$$\mathcal{L}\left(l, \phi, \dot{l}, \dot{\phi}\right) = \frac{1}{2}\dot{l}^2 + \frac{1}{2} r^2(l)\, \dot{\phi}^2 \,, \tag{A.2}$$

where the dot denotes a derivative with respect to some parameter λ. Solving the Euler-Lagrange equations for l and ϕ yields the desired symbols by comparing coefficients [28]. We get

$$0 = \frac{d}{d\lambda}\frac{\partial \mathcal{L}}{\partial \dot{l}} - \frac{\partial \mathcal{L}}{\partial l} = \ddot{l} - r(l)\, r'(l)\, \dot{\phi}^2 \stackrel{!}{=} \ddot{l} + \Gamma^l_{\phi\phi}\, \dot{\phi}^2 \,, \tag{A.3}$$

and

$$0 = \frac{1}{r^2(l)}\left(\frac{d}{d\lambda}\frac{\partial \mathcal{L}}{\partial \dot{\phi}} - \frac{\partial \mathcal{L}}{\partial \phi}\right) = \ddot{\phi} + \frac{2r'(l)}{r(l)}\, \dot{l}\dot{\phi} \stackrel{!}{=} \ddot{\phi} + \Gamma^\phi_{l\phi}\, \dot{l}\dot{\phi} + \Gamma^\phi_{\phi l}\, \dot{\phi}\dot{l} \,. \tag{A.4}$$

The only non-zero Christoffel symbols are therefore given by $\Gamma^l_{\phi\phi} = -r(l)\, r'(l)$ and $\Gamma^\phi_{l\phi} = \Gamma^\phi_{\phi l} = r'(l)/r(l)$.

We obtain the coefficients of the spin connection using [28]

$$\omega^{ab}_\mu = e^a_\nu \Gamma^\nu_{\sigma\mu} e^{\sigma b} + e^a_\nu \partial_\mu e^{\nu b} \,. \tag{A.5}$$

This finally gives $\omega^{12}_\phi = -\omega^{21}_\phi = -r'(l)$ and yields the spin connection 1-form [28]

$$\boldsymbol{\omega^{ab}} = \omega^{ab}_\mu dx^\mu = \omega^{ab}_\phi dx^\phi \,. \tag{A.6}$$

A.2. Confluent hypergeometric differential equation

We want to solve the differential equation to obtain excited states of the pseudosphere in an overall perpendicular magnetic field (see Eq. (4.11) transformed to the radius coordinate). The equation to solve is of the form

$$x^2 \frac{d^2 y(x)}{dx^2} + (\alpha x + \beta)\frac{dy(x)}{dx} + \gamma y(x) = 0 \,, \tag{A.7}$$

with parameters α, β and γ. This is a *degenerate doubly-confluent Heun equation* [118]. Following [118], we make the transformation

$$\tilde{x} = \frac{\beta}{x},\ y(\tilde{x}) = \tilde{x}^{\Delta_\pm}\tilde{y}(\tilde{x}),\ \Delta_\pm = \frac{\alpha - 1 \pm \sqrt{(\alpha-1)^2 - 4\gamma}}{2}\,. \tag{A.8}$$

This yields a *confluent hypergeometric equation* [98],

$$\tilde{x}\frac{d^2\tilde{y}(\tilde{x})}{d\tilde{x}^2} + \left[(2\Delta_\pm + 2 - \alpha) - \tilde{x}\right]\frac{d\tilde{y}(\tilde{x})}{d\tilde{x}} - \Delta_\pm \tilde{y}(\tilde{x}) = 0\,. \tag{A.9}$$

A basis of solutions for this differential equation is given by *Kummer's function* $M(a,b,z)$ [27]

$$y_-(x) = x^{-\Delta_-} M\left(\Delta_-, 2\Delta_- + 2 - \alpha, \frac{\beta}{x}\right)\,, \tag{A.10}$$

$$y_+(x) = x^{-\Delta_+} M\left(\Delta_+, 2\Delta_+ + 2 - \alpha, \frac{\beta}{x}\right)\,. \tag{A.11}$$

The author of this thesis argued in [27] that only polynomial solutions are normalizable and therefore yield physical states. The condition for $M(a,b,z)$ to condensate into a polynomial is [98]

$$\Delta_\pm \overset{!}{=} -n,\ n \in \{0,1,2,\dots\}\,, \tag{A.12}$$

This equation can only be solved for Δ_- and reads

$$\gamma = -n^2 - n\,(\alpha - 1)\ . \tag{A.13}$$

The corresponding solution $y(x)$ can easily be found by placing this back into our basis of solutions, yielding

$$y(x) = x^n M\left(-n, -2n + 2 - \alpha, \frac{\beta}{x}\right)\,. \tag{A.14}$$

It turns out that *Kummer's function* for these special parameters gives *associated Laguerre polynomials* $L_n^{(a)}(x)$ and henceforth [98]

$$y(x) = x^n L_n^{(-2n+1-\alpha)}\left(\frac{\beta}{x}\right)\,, \tag{A.15}$$

where some constants were absorbed.

A.3. Shape invariance of the effective potential

We want to show that the effective potential of the pseudosphere in a perpendicular magnetic field,

$$V(l) = \frac{m}{a}\exp\left(\frac{l}{a}\right) + akB\,, \tag{A.16}$$

with $k = e/\hbar$ is shape invariant in the sense of SUSY (Eq. 2.4). We need the expressions

$$V^2(l) = \frac{m^2}{a^2}\exp\left(\frac{2l}{a}\right) + a^2k^2B^2 + 2mkB\exp\left(\frac{l}{a}\right)\,,\; V'(l) = \frac{m}{a^2}\exp\left(\frac{l}{a}\right)\,, \tag{A.17}$$

to write down the SUSY potentials [78]

$$V_{S\pm}(l) = \frac{m^2}{a^2}\exp\left(\frac{2l}{a}\right) + m\left(2kB \pm \frac{1}{a^2}\right)\exp\left(\frac{l}{a}\right) + a^2k^2B^2\,. \tag{A.18}$$

Shape invariance requires the difference

$$\begin{aligned} V_{S-}(m_1, B_1, l) - V_{S+}(m_2, B_2, l) \;=\; & +\frac{m_1^2 - m_2^2}{a^2}\exp\left(\frac{2l}{a}\right) \\ & +2k(B_1m_1 - B_2m_2)\exp\left(\frac{l}{a}\right) \\ & -\frac{m_1 + m_2}{a^2}\exp\left(\frac{l}{a}\right) \\ & +a^2k^2(B_1^2 - B_2^2) \end{aligned} \tag{A.19}$$

to be of the form $R(m_1, B_1)$. Therefore, all non-constant terms have to vanish. The first term implies $|m_1| = |m_2|$ which only leaves the two possibilites $m_2 = \pm m_1$. Choosing the angular quantum numbers to have opposite sign leads to $B_1 = -B_2$ and $R(m_1, B_1) = 0$. This is the almost trivial shape invariance which always holds but does not yield the full spectrum. The equal sign solution leads to the constraint $B_2 = B_1 - 1/(ka^2)$ and therefore to $B_2 = f(B_1) = B_1 - 1/(ka^2)$ and $R(B_1) = 2kB_1 - 1/a^2$ which is a translational shape invariance.

A.4. Action integral for the pseudosphere

We want to solve an integral of the form

$$I = \int_0^{s_>} ds\,\sqrt{A - B\cosh(Cx)}\,, \tag{A.20}$$

where $s_>$ and $s_<$ are the zeros of the radicand with $s_< < s_>$ for $A, B, C > 0$. It makes sense to perform the substitution $\cosh(Cs) = 1 + \frac{A-B}{B}t$ which yields

$$\begin{aligned} I &= \frac{A-B}{C\sqrt{2B}} \int_0^1 dt\, t^{-\frac{1}{2}}(1-t)^{\frac{1}{2}} \left(1 + \frac{A-B}{B}t\right)^{-\frac{1}{2}} \\ &= \frac{A-B}{C\sqrt{2B}} \frac{\Gamma\left(\frac{1}{2}\right)\Gamma\left(\frac{3}{2}\right)}{\Gamma(2)} {}_2F_1\left(\frac{1}{2}, \frac{1}{2}; 2; -\frac{A-B}{B}\right) \\ &= \frac{\pi}{2} \frac{A-B}{C\sqrt{2B}} {}_2F_1\left(\frac{1}{2}, \frac{1}{2}; 2; -\frac{A-B}{B}\right) \\ &= \frac{\pi}{2} \frac{A-B}{C\sqrt{2A}} {}_2F_1\left(\frac{3}{2}, \frac{1}{2}; 2; \frac{A-B}{A}\right) \end{aligned} \tag{A.21}$$

where we used the integral representation of the *Gaussian hypergeometric function* ${}_2F_1(a, b; c; z)$ [98] and a *Pfaff transformation* in the last step [98].

A.5. Action integral for the general class of surfaces

We want to solve an integral of the form

$$I = \int_{s_<}^{s_>} ds\, \sqrt{A - Bs^{\kappa} - Cs^{-\kappa}}\,, \tag{A.22}$$

where $s_<$ and $s_>$ are the zeros of the radicand with $s_< < s_>$ for $\kappa > 0$ and $s_> < s_<$ for $\kappa < 0$ and $A, B, C > 0$. It makes sense to perform the substitution $u = s^{\kappa}$ which yields

$$\begin{aligned} I &= \frac{1}{\kappa} \int_{u_<}^{u_>} du\, u^{-\frac{\kappa-1}{\kappa}} \sqrt{A - Bu - Cu^{-1}} \\ &= \frac{1}{\kappa} \int_{u_<}^{u_>} du\, u^{-\frac{3\kappa-2}{2\kappa}} \sqrt{-Bu^2 + Au - C} \\ &= \frac{\sqrt{B}}{\kappa} \int_{u_<}^{u_>} du\, u^{-\frac{3\kappa-2}{2\kappa}} \sqrt{(u-u_<)(u_> - u)}\,, \end{aligned} \tag{A.23}$$

note that here it always holds that $u_< < u_>$. Now we can perform the substitution $u = u_< + (u_> - u_<)t$ which gives

$$\begin{aligned} I &= \frac{\sqrt{B}}{\kappa} (u_> - u_<)^2 \int_0^1 dt\, (u_< + (u_> - u_<)t)^{-\frac{3\kappa-2}{2\kappa}} \sqrt{t(1-t)} \\ &= \frac{\sqrt{B}}{\kappa} (u_> - u_<)^2\, u_<^{-\frac{3\kappa-2}{2\kappa}} \int_0^1 dt\, \left(1 + \left(\frac{u_>}{u_<} - 1\right)t\right)^{-\frac{3\kappa-2}{2\kappa}} \sqrt{t(1-t)} \\ &= \frac{\sqrt{B}}{\kappa} (u_> - u_<)^2\, u_<^{-\frac{3\kappa-2}{2\kappa}} \frac{\Gamma\left(\frac{3}{2}\right)\Gamma\left(\frac{3}{2}\right)}{\Gamma(3)} {}_2F_1\left(\frac{3}{2} - \frac{1}{\kappa}, \frac{3}{2}; 3; 1 - \frac{u_>}{u_<}\right) \\ &= \frac{\pi\sqrt{B}}{8\kappa} (u_> - u_<)^2\, u_<^{-\frac{3}{2}+\frac{1}{\kappa}} {}_2F_1\left(\frac{3}{2} - \frac{1}{\kappa}, \frac{3}{2}; 3; 1 - \frac{u_>}{u_<}\right)\,, \end{aligned} \tag{A.24}$$

where we used the integral representation of the *Gaussian hypergeometric function* ${}_2F_1(a, b; c; z)$ [98].

A.6. Laplace transform of the antiderivate of the Fermi-Dirac distribution

The second derivative of $F(E)$ reads

$$F''(E) = -\frac{1}{2T}\frac{1}{1+\cosh\left(\frac{E}{T}\right)} \,. \tag{A.25}$$

The bilateral Laplace transform is given by

$$\begin{aligned} F''(s) &= -\frac{1}{2T}\int_{-\infty}^{\infty} dE\,\frac{\exp(-Es)}{1+\cosh\left(\frac{E}{T}\right)} \\ &= -\frac{1}{2}\int_{-\infty}^{\infty} dz\,\frac{\exp(-Tzs)}{1+\cosh(z)} \\ &= i\pi\sum_{n=0}^{\infty}\operatorname*{Res}_{z=-i\pi(2n+1)}\left\{\frac{\exp(-Tzs)}{1+\cosh(z)}\right\} \\ &= i2\pi Ts\sum_{n=0}^{\infty}\exp\left(i\pi T(2n+1)s\right) \\ &= i2\pi Ts\exp\left(i\pi Ts\right)\sum_{n=0}^{\infty}\exp\left(i2\pi nTs\right) \\ &= i2\pi Ts\frac{\exp\left(i\pi Ts\right)}{1-\exp\left(i2\pi Ts\right)} \\ &= -\frac{i2\pi Ts}{\exp\left(i\pi Ts\right)-\exp\left(-i\pi Ts\right)} \\ &= -\frac{\pi Ts}{\sin\left(\pi Ts\right)} \,, \end{aligned} \tag{A.26}$$

where we used the residue theorem and the integration contour shown in Fig. A.1. The region of convergence is obviously $-1/T < \sigma < 1/T$.

A.7. Fermi-Dirac integral for oscillating density of states

We can solve the integrals involving $F''(E)$ and a quickly oscillating function with amplitude $A(E)$ and phase $S(E)$ using the approximation [104]

$$\int_0^{\infty} dE\,A(E)\exp(iS(E))F''(E-\mu) \approx -A(\mu)\exp(iS(\mu))\frac{\pi TS'(\mu)}{\sinh(\pi TS'(\mu))} \,, \tag{A.27}$$

where $S' = dS/dE$ and $A(E)$ varies slowly compared to the oscillating term. With this, we easily find

$$\int_0^{\infty} dE\,\cos\left(\frac{\pi k}{2\nu}E^2\right)F''(E-\mu) \approx -\frac{\pi^2 Tk\mu}{\nu}\frac{\cos\left(\frac{\pi k\mu^2}{2\nu}\right)}{\sinh\left(\frac{\pi^2 Tk\mu}{\nu}\right)} \,, \tag{A.28}$$

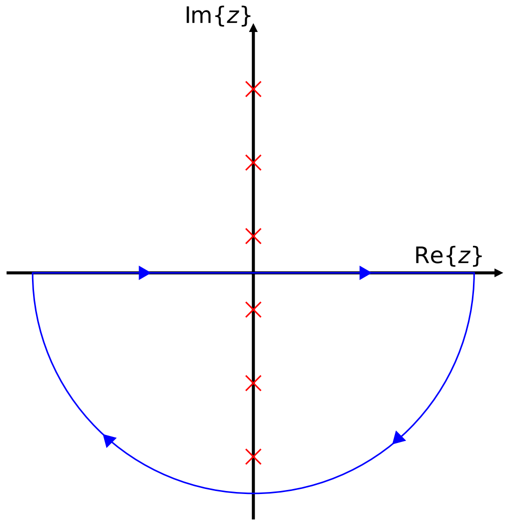

Figure A.1: Contour (blue) for evaluation of the integral, as well as poles of the integrand (red). The radius of the half circle goes to infinity in the real calculation. A finite radius was only chosen for the sake of illustration.

$$\int_0^\infty dE\, E^2 \sin\left(\frac{\pi k}{2\nu}E^2\right) F''(E-\mu) \approx -\frac{\pi^2 T k \mu^3}{\nu} \frac{\sin\left(\frac{\pi k \mu^2}{2\nu}\right)}{\sinh\left(\frac{\pi^2 T k \mu}{\nu}\right)} . \tag{A.29}$$

For the integral of the oscillating part of the Fresnel functions, we use an integral representation derived in [70], which we adapted to our definition of the Fresnel integrals,

$$\tilde{C}(x) = -\frac{1}{\sqrt{2}\pi}\mathrm{Re}\left\{\int_0^\infty du\, \frac{1}{\sqrt{u}} \frac{\exp\left(-\frac{\pi}{2}(u-i)x^2\right)}{u-i}\right\} , \tag{A.30}$$

$$\tilde{S}(x) = -\frac{1}{\sqrt{2}\pi}\mathrm{Im}\left\{\int_0^\infty du\, \frac{1}{\sqrt{u}} \frac{\exp\left(-\frac{\pi}{2}(u-i)x^2\right)}{u-i}\right\} . \tag{A.31}$$

Applying the approximation yields

$$\begin{aligned}
& \int_0^\infty dE\, E^3 \tilde{\mathrm{C}}\left(\sqrt{\frac{k}{\nu}}E\right) F''(E-\mu) \qquad \text{(A.32)}\\
= & -\frac{1}{\sqrt{2}\pi}\mathrm{Re}\left\{\int_0^\infty du\,\frac{1}{\sqrt{u}}\frac{1}{u-i}\int_0^\infty dE\, E^3\exp\left(-\frac{\pi k}{2\nu}(u-i)E^2\right)F''(E-\mu)\right\}\\
\approx & \ \frac{1}{\sqrt{2}\pi}\mathrm{Re}\left\{\int_0^\infty du\,\frac{1}{\sqrt{u}}\frac{1}{u-i}\mu^3\exp\left(-\frac{\pi k}{2\nu}(u-i)\mu^2\right)\frac{\pi^2 Tk\mu}{\nu}\frac{1}{\sinh\left(\frac{\pi^2 Tk\mu}{\nu}\right)}\right\}\\
= & \ \frac{\pi Tk\mu^4}{\sqrt{2}\nu}\frac{1}{\sinh\left(\frac{\pi^2 Tk\mu}{\nu}\right)}\mathrm{Re}\left\{\int_0^\infty du\,\frac{1}{\sqrt{u}}\frac{1}{u-i}\exp\left(-\frac{\pi k}{2\nu}(u-i)\mu^2\right)\right\}\\
= & -\frac{\pi^2 Tk\mu^4}{\nu}\frac{\tilde{\mathrm{C}}\left(\sqrt{\frac{k}{\nu}}\mu\right)}{\sinh\left(\frac{\pi^2 Tk\mu}{\nu}\right)},
\end{aligned}$$

and

$$\begin{aligned}
& \int_0^\infty dE\, E\tilde{\mathrm{S}}\left(\sqrt{\frac{k}{\nu}}E\right) F''(E-\mu) \qquad \text{(A.33)}\\
= & -\frac{1}{\sqrt{2}\pi}\mathrm{Im}\left\{\int_0^\infty du\,\frac{1}{\sqrt{u}}\frac{1}{u-i}\int_0^\infty dE\, E\exp\left(-\frac{\pi k}{2\nu}(u-i)E^2\right)F''(E-\mu)\right\}\\
\approx & \ \frac{1}{\sqrt{2}\pi}\mathrm{Im}\left\{\int_0^\infty du\,\frac{1}{\sqrt{u}}\frac{1}{u-i}\mu\exp\left(-\frac{\pi k}{2\nu}(u-i)\mu^2\right)\frac{\pi^2 Tk\mu}{\nu}\frac{1}{\sinh\left(\frac{\pi^2 Tk\mu}{\nu}\right)}\right\}\\
= & \ \frac{\pi Tk\mu^2}{\sqrt{2}\nu}\frac{1}{\sinh\left(\frac{\pi^2 Tk\mu}{\nu}\right)}\mathrm{Im}\left\{\int_0^\infty du\,\frac{1}{\sqrt{u}}\frac{1}{u-i}\exp\left(-\frac{\pi k}{2\nu}(u-i)\mu^2\right)\right\}\\
= & -\frac{\pi^2 Tk\mu^2}{\nu}\frac{\tilde{\mathrm{S}}\left(\sqrt{\frac{k}{\nu}}\mu\right)}{\sinh\left(\frac{\pi^2 Tk\mu}{\nu}\right)}.
\end{aligned}$$

List of publications:

- **M. Fürst**, D. Kochan, I.-G. Dusa, C. Gorini, and K. Richter, "Dirac Landau levels for surfaces with constant negative curvature", Phys. Rev. B **109**, 195433 (2024)
- I.-G. Dusa, D. Kochan, **M. Fürst**, C. Gorini, and K. Richter, "Hearing the shape of a Dirac drum: Dual quantum Hall states on curved surfaces", Phys. Rev. B **113**, L241405 (2026)
- **M. Fürst**, and K. Richter, "Landau levels of Dirac states on curved topological insulator surfaces", in: *The effects of Curvature in Condensed Matter Physics*, edited by C. Ortix, D. Makarov, and P. Gentile [under review] (2026)
- **M. Fürst**, K. Richter, and D. Kochan, "Orbital magnetism of Dirac electrons on surfaces with constant curvature", [in preparation] (2026)

Bibliography

[1] P. R. Wallace, “The Band Theory of Graphite”, Phys. Rev. **71**, 622–634 (1947).

[2] K. S. Novoselov, A. K. Geim, S. V. Morozov, D. Jiang, M. I. Katsnelson, I. V. Grigorieva, S. V. Dubonos, and A. A. Firsov, “Two-dimensional gas of massless Dirac fermions in graphene”, Nature **438**, 197–200 (2005).

[3] B. A. Volkov and O. A. Pankratov, “Two-dimensional massless electrons in an inverted contact”, JETP Lett. **42**, 145 (1985).

[4] L. Fu, C. L. Kane, and E. J. Mele, “Topological Insulators in Three Dimensions”, Phys. Rev. Lett. **98**, 106803 (2007).

[5] J. E. Moore and L. Balents, “Topological invariants of time-reversal-invariant band structures”, Phys. Rev. B **75**, 121306(R) (2007).

[6] D. Hsieh, D. Qian, L. Wray, Y. Xia, Y. S. Hor, R. J. Cava, and M. Z. Hasan, “A topological Dirac insulator in a quantum spin Hall phase”, Nature **452**, 970–974 (2008).

[7] L. Landau, “Diamagnetismus der Metalle”, Zeitschrift für Physik **64**, 629–637 (1930).

[8] I. I. Rabi, “Das freie Elektron im homogenen Magnetfeld nach der Diracschen Theorie”, Zeitschrift für Physik **49**, 507–511 (1928).

[9] T. Ando, “Theory of Electronic States and Transport in Carbon Nanotubes”, Journal of the Physical Society of Japan **74**, 777–817 (2005).

[10] U. D. Jentschura, “Algebraic approach to relativistic Landau levels in the symmetric gauge”, Phys. Rev. D **108**, 016016 (2023).

[11] S. G. Sharapov, V. P. Gusynin, and H. Beck, “Magnetic oscillations in planar systems with the Dirac-like spectrum of quasiparticle excitations”, Phys. Rev. B **69**, 075104 (2004).

[12] I. A. Luk’yanchuk and Y. Kopelevich, “Phase Analysis of Quantum Oscillations in Graphite”, Phys. Rev. Lett. **93**, 166402 (2004).

[13] C. Berger, Z. Song, T. Li, X. Li, A. Y. Ogbazghi, R. Feng, Z. Dai, A. N. Marchenkov, E. H. Conrad, P. N. First, and W. A. de Heer, “Ultrathin Epitaxial Graphite: 2D

Electron Gas Properties and a Route toward Graphene-based Nanoelectronics", The Journal of Physical Chemistry B **108**, 19912–19916 (2004).

[14] M. Kessel, J. Hajer, G. Karczewski, C. Schumacher, C. Brüne, H. Buhmann, and L. W. Molenkamp, "CdTe-HgTe core-shell nanowire growth controlled by RHEED", Phys. Rev. Mater. **1**, 023401 (2017).

[15] J. Ziegler, R. Kozlovsky, C. Gorini, M.-H. Liu, S. Weishäupl, H. Maier, R. Fischer, D. A. Kozlov, Z. D. Kvon, N. Mikhailov, S. A. Dvoretsky, K. Richter, and D. Weiss, "Probing spin helical surface states in topological HgTe nanowires", Phys. Rev. B **97**, 035157 (2018).

[16] B. S. DeWitt, "Dynamical Theory in Curved Spaces. I. A Review of the Classical and Quantum Action Principles", Rev. Mod. Phys. **29**, 377–397 (1957).

[17] L. Parker, "Quantized Fields and Particle Creation in Expanding Universes. I", Phys. Rev. **183**, 1057–1068 (1969).

[18] S. W. Hawking, "Particle creation by black holes", Communications in Mathematical Physics **43**, 199–220 (1975).

[19] W. G. Unruh, "Notes on black-hole evaporation", Phys. Rev. D **14**, 870–892 (1976).

[20] R. C. T. da Costa, "Quantum mechanics of a constrained particle", Phys. Rev. A **23**, 1982–1987 (1981).

[21] H Jensen and H Koppe, "Quantum mechanics with constraints", Annals of Physics **63**, 586–591 (1971).

[22] G. Ferrari and G. Cuoghi, "Schrödinger Equation for a Particle on a Curved Surface in an Electric and Magnetic Field", Phys. Rev. Lett. **100**, 230403 (2008).

[23] C.-X. Liu, X.-L. Qi, H. Zhang, X. Dai, Z. Fang, and S.-C. Zhang, "Model Hamiltonian for topological insulators", Phys. Rev. B **82**, 045122 (2010).

[24] Y. Takane and K.-I. Imura, "Unified Description of Dirac Electrons on a Curved Surface of Topological Insulators", Journal of the Physical Society of Japan **82**, 074712 (2013).

[25] H. Zhang, C.-X. Liu, X.-L. Qi, X. Dai, Z. Fang, and S.-C. Zhang, "Topological insulators in Bi2Se3, Bi2Te3 and Sb2Te3 with a single Dirac cone on the surface", Nature Physics **5**, 438–442 (2009).

[26] D.-H. Lin and D.-W. Chiou, "On the path of spin-1/2 Berry phase", Results in Physics **64**, 107907 (2024).

[27] M. Fürst, D. Kochan, I.-G. Dusa, C. Gorini, and K. Richter, "Dirac Landau levels for surfaces with constant negative curvature", Phys. Rev. B **109**, 195433 (2024).

[28] M. Fecko, *Differential Geometry and Lie Groups for Physicists* (Cambridge University Press, Cambridge, 2006), pp. 1–697.

[29] I. Dusa, D. Kochan, M. Fürst, C. Gorini, and K. Richter, “Hearing the shape of a Dirac drum: Dual quantum Hall states on curved surfaces”, Phys. Rev. B **113**, L241405 (2026).

[30] A Pnueli, “Spinors and scalars on Riemann surfaces”, Journal of Physics A: Mathematical and General **27**, 1345 (1994).

[31] H. Aoki and H. Suezawa, “Landau quantization of electrons on a sphere”, Phys. Rev. A **46**, R1163(R)–R1166(R) (1992).

[32] A Ralko and T. T. Truong, “Heun functions and the energy spectrum of a charged particle on a sphere under a magnetic field and Coulomb force”, Journal of Physics A: Mathematical and General **35**, 9573 (2002).

[33] A. Çetin, “Exact energy levels and eigenfunctions of an electron on a nanosphere under the influence of a radial magnetic field”, Physica B: Condensed Matter **523**, 92–95 (2017).

[34] M. D. Oliveira and A. G. M. Schmidt, “Exact solutions of Schrödinger and Pauli equations for a charged particle on a sphere and interacting with non-central potentials”, Journal of Mathematical Physics **60**, 032102 (2019).

[35] J. Elstrodt, “Die Resolvente zum Eigenwertproblem der automorphen Formen in der hyperbolischen Ebene. Teil II”, Mathematische Zeitschrift **132**, 99–134 (1973).

[36] A. Comtet, “On the landau levels on the hyperbolic plane”, Annals of Physics **173**, 185–209 (1987).

[37] C. Grosche, “The path integral on the Poincaré upper half-plane with a magnetic field and for the Morse potential”, Annals of Physics **187**, 110–134 (1988).

[38] C Grosche, “Path integration on hyperbolic spaces”, Journal of Physics A: Mathematical and General **25**, 4211 (1992).

[39] C. Grosche, “On the Path Integral Treatment for an Aharonov-Bohm Field on the Hyperbolic Plane”, International Journal of Theoretical Physics **38**, 955–969 (1999).

[40] N. Ikeda and H. Matsumoto, “Brownian Motion on the Hyperbolic Plane and Selberg Trace Formula”, Journal of Functional Analysis **163**, 63–110 (1999).

[41] E. V. Ferapontov and A. P. Veselov, “Integrable Schroedinger operators with magnetic fields: Factorization method on curved surfaces”, Journal of Mathematical Physics **42**, 590 (2001).

[42] S. Ganeshan and A. P. Polychronakos, “Lyapunov exponents and entanglement entropy transition on the noncommutative hyperbolic plane”, SciPost Phys. Core **3**, 003 (2020).

[43] O. Lisovyy, “Aharonov-Bohm effect on the Poincaré disk”, Journal of Mathematical Physics **48**, 052112 (2007).

[44] J. Schliemann, “Graphene in a strong magnetic field: Massless Dirac particles versus skyrmions”, Phys. Rev. B **78**, 195426 (2008).

[45] D.-H. Lee, “Surface States of Topological Insulators: The Dirac Fermion in Curved Two-Dimensional Spaces”, Phys. Rev. Lett. **103**, 196804 (2009).

[46] M. Greiter and R. Thomale, “Landau level quantization of Dirac electrons on the sphere”, Annals of Physics **394**, 33–39 (2018).

[47] A. Comtet and P. J. Houston, “Effective action on the hyperbolic plane in a constant external field”, J. Math. Phys. **26**, 185 (1985).

[48] E. Gorbar and V. Gusynin, “Gap generation for Dirac fermions on Lobachevsky plane in a magnetic field”, Annals of Physics **323**, 2132–2146 (2008).

[49] D. Demir Kızılırmak, Ş. Kuru, and J. Negro, “Dirac-Weyl equation on a hyperbolic graphene surface under magnetic fields”, Physica E: Low-dimensional Systems and Nanostructures **118**, 113926 (2020).

[50] D. D. Kızılırmak and Ş. Kuru, “The solutions of Dirac equation on the hyperboloid under perpendicular magnetic fields”, Physica Scripta **96**, 025806 (2020).

[51] D.-N. Le, V.-H. Le, and P. Roy, “Electric field and curvature effects on relativistic Landau levels on a pseudosphere”, Journal of Physics: Condensed Matter **31**, 305301 (2019).

[52] I. I. Kouachi and Ö. Yeşiltaş, “Dirac fermions in graphene under curved spacetime: a study of Beltrami geometry and $\mathcal{CPT}$ symmetry”, The European Physical Journal C **85**, 102 (2025).

[53] R. Kozlovsky, A. Graf, D. Kochan, K. Richter, and C. Gorini, “Magnetoconductance, Quantum Hall Effect, and Coulomb Blockade in Topological Insulator Nanocones”, Phys. Rev. Lett. **124**, 126804 (2020).

[54] A. Graf, R. Kozlovsky, K. Richter, and C. Gorini, “Theory of magnetotransport in shaped topological insulator nanowires”, Phys. Rev. B **102**, 165105 (2020).

[55] R. Kozlovsky, “Magnetotransport in 3D Topological Insulator Nanowires”, PhD thesis (2020).

[56] M. Barth, “Spectral properties and quantum transport in hybrid Dirac systems”, PhD thesis (2024).

[57] E. Xypakis, J.-W. Rhim, J. H. Bardarson, and R. Ilan, “Perfect transmission and Aharanov-Bohm oscillations in topological insulator nanowires with nonuniform cross section”, Phys. Rev. B **101**, 045401 (2020).

[58] R. Saxena, E. Grosfeld, S. E de Graaf, T. Lindstrom, F. Lombardi, O. Deb, and E. Ginossar, “Electronic confinement of surface states in a topological insulator nanowire”, Phys. Rev. B **106**, 035407 (2022).

[59] J. W. McClure, “Diamagnetism of Graphite”, Phys. Rev. **104**, 666–671 (1956).

[60] S. A. Safran and F. J. DiSalvo, “Theory of magnetic susceptibility of graphite intercalation compounds”, Phys. Rev. B **20**, 4889–4895 (1979).

[61] H. Fukuyama, “Anomalous Orbital Magnetism and Hall Effect of Massless Fermions in Two Dimension”, Journal of the Physical Society of Japan **76**, 043711 (2007).

[62] M. Koshino and T. Ando, “Diamagnetism in disordered graphene”, Phys. Rev. B **75**, 235333 (2007).

[63] M. Nakamura, “Orbital magnetism and transport phenomena in two-dimensional Dirac fermions in a weak magnetic field”, Phys. Rev. B **76**, 113301 (2007).

[64] M. Koshino, Y. Arimura, and T. Ando, “Magnetic Field Screening and Mirroring in Graphene”, Phys. Rev. Lett. **102**, 177203 (2009).

[65] S. Zhang, N. Ma, and E. Zhang, “The modulation of the de Haas–van Alphen effect in graphene by electric field”, Journal of Physics: Condensed Matter **22**, 115302 (2010).

[66] Y. Arimura, M. Koshino, and T. Ando, “Diamagnetic Response of Disordered Graphene to Nonuniform Magnetic Field”, Journal of the Physical Society of Japan **80**, 114705 (2011).

[67] A. Jellal, M. Bellati, and M. Schreiber, “Diamagnetism of confined Dirac fermions in disordered graphene”, Journal of Physics A: Mathematical and Theoretical **44**, 275001 (2011).

[68] M. Koshino and T. Ando, “Singular orbital magnetism of graphene”, Solid State Communications **151**, Graphene, 1054–1060 (2011).

[69] Y. Ominato and M. Koshino, “Orbital magnetism of graphene flakes”, Phys. Rev. B **87**, 115433 (2013).

[70] L. Heße and K. Richter, “Orbital magnetism of graphene nanostructures: Bulk and confinement effects”, Phys. Rev. B **90**, 205424 (2014).

[71] X.-Z. Yan and C. S. Ting, “Orbital magnetization of interacting Dirac fermions in graphene”, Phys. Rev. B **96**, 104403 (2017).

[72] F Escudero, J. S. Ardenghi, and P Jasen, “Temperature effect on the magnetic oscillations in 2D materials”, Journal of Physics: Condensed Matter **31**, 285804 (2019).

[73] X.-D. Tan, J.-Q. Han, and L. Zhang, “Pauli susceptibility of zigzag graphene nanoribbons”, Micro and Nanostructures **184**, 207687 (2023).

[74] E. Schrödinger, “Diracsches Elektron im Schwerefeld I”, Sitzungsber. Preuss. Akad. Wiss., Phys.-Math. Kl., 105–128 (1932).

[75] A. Lichnerowicz, “Spineurs harmoniques”, C. R. Acad. Sci. Paris **257**, 7–9 (1963).

[76] M. Fürst, *Dirac Landau levels on a Pseudosphere, Master thesis*, 2022.

[77] I. Dusa, *Transport and Spectral Properties of Electrons on Curved Three-Dimensional Topological Insulators, Master thesis*, 2024.

[78] F. Cooper, A. Khare, and U. Sukhatme, “Supersymmetry and quantum mechanics”, Physics Reports **251**, 267–385 (1995).

[79] Y. A. Golfand and E. P. Likhtman, “Extension of the Algebra of Poincare Group Generators and Violation of p Invariance”, JETP Lett. **13**, edited by A. Salam and E. Sezgin, 323–326 (1971).

[80] J.-L. Gervais and B. Sakita, “Field theory interpretation of supergauges in dual models”, Nuclear Physics B **34**, 632–639 (1971).

[81] E. Witten, “Dynamical breaking of supersymmetry”, Nuclear Physics B **188**, 513–554 (1981).

[82] E. Witten, “Constraints on supersymmetry breaking”, Nuclear Physics B **202**, 253–316 (1982).

[83] G. Teschl, *Ordinary Differential Equations and Dynamical Systems*, Graduate studies in mathematics (American Mathematical Society, 2012).

[84] D. Tong, *Lectures on the Quantum Hall Effect*, 2016.

[85] C. W. J. Beenakker, A. Donís Vela, G. Lemut, M. J. Pacholski, and J. Tworzydło, “Tangent Fermions: Dirac or Majorana Fermions on a Lattice Without Fermion Doubling”, Annalen der Physik **535**, 2300081 (2023).

[86] K. G. Wilson, “Confinement of quarks”, Phys. Rev. D **10**, 2445–2459 (1974).

[87] L. Susskind, “Lattice fermions”, Phys. Rev. D **16**, 3031–3039 (1977).

[88] H. Nielsen and M. Ninomiya, “A no-go theorem for regularizing chiral fermions”, Physics Letters B **105**, 219–223 (1981).

[89] R. Stacey, “Eliminating lattice fermion doubling”, Phys. Rev. D **26**, 468–472 (1982).

[90] T. Friedrich, *Dirac Operators in Riemannian Geometry*, Graduate studies in mathematics (American Mathematical Society, 2000).

[91] E. Noether, “Invariante Variationsprobleme”, ger, Nachrichten von der Gesellschaft der Wissenschaften zu Göttingen, Mathematisch-Physikalische Klasse **1918**, 235–257 (1918).

[92] C.-K. Chiu, J. C. Y. Teo, A. P. Schnyder, and S. Ryu, “Classification of topological quantum matter with symmetries”, Rev. Mod. Phys. **88**, 035005 (2016).

[93] M. E. Peskin and D. V. Schroeder, *An Introduction to quantum field theory* (Addison-Wesley, Reading, USA, 1995).

[94] M. F. Atiyah and I. M. Singer, “The index of elliptic operators on compact manifolds”, Bull. Am. Math. Soc. **69**, 422–433 (1969).

[95] Y. Aharonov and A. Casher, “Ground state of a spin-$\frac{1}{2}$ charged particle in a two-dimensional magnetic field”, Phys. Rev. A **19**, 2461–2462 (1979).

[96] M. Fialová, “Aharonov–Casher Theorems for Dirac Operators on Manifolds with Boundary and APS Boundary Condition”, Annales Henri Poincaré **26**, 2859–2900 (2025).

[97] E. W. Weisstein, *Pseudosphere*, From MathWorld–A Wolfram Resource.

[98] *NIST Digital Library of Mathematical Functions*, `https://dlmf.nist.gov/`, Release 1.2.7 of 2026-06-15, F. W. J. Olver, A. B. Olde Daalhuis, D. W. Lozier, B. I. Schneider, R. F. Boisvert, C. W. Clark, B. R. Miller, B. V. Saunders, H. S. Cohl, and M. A. McClain, eds.

[99] P. M. Morse, “Diatomic Molecules According to the Wave Mechanics. II. Vibrational Levels”, Phys. Rev. **34**, 57–64 (1929).

[100] W Lay, K Bay, and S. Y. Slavyanov, “Asymptotic and numeric study of eigenvalues of the double confluent Heun equation”, Journal of Physics A: Mathematical and General **31**, 8521 (1998).

[101] A. Bittner, *Landau levels on a sphere in a coaxial magnetic field, Bachelor thesis*, 2023.

[102] S. Schümann, *Numerical calculations of Dirac-Landau-Levels of a sphere in a coaxial magnetic field, Bachelor thesis*, 2024.

[103] L. D. Landau and E. M. Lifshitz, *Statistical Physics, Part 1*, Vol. 5, Course of Theoretical Physics (Butterworth-Heinemann, Oxford, 1980).

[104] K. Richter, D. Ullmo, and R. A. Jalabert, "Orbital magnetism in the ballistic regime: geometrical effects", Physics Reports **276**, 1–83 (1996).

[105] A. Oppenheim, A. Willsky, and S. Nawab, *Signals & Systems*, Prentice-Hall signal processing series (Prentice-Hall International, 1997).

[106] A. Ghosal, P. Goswami, and S. Chakravarty, "Diamagnetism of nodal fermions", Phys. Rev. B **75**, 115123 (2007).

[107] V. Chandrasekhar, R. A. Webb, M. J. Brady, M. B. Ketchen, W. J. Gallagher, and A. Kleinsasser, "Magnetic response of a single, isolated gold loop", Phys. Rev. Lett. **67**, 3578–3581 (1991).

[108] D. Mailly, C. Chapelier, and A. Benoit, "Experimental observation of persistent currents in GaAs-AlGaAs single loop", Phys. Rev. Lett. **70**, 2020–2023 (1993).

[109] U. Eckern and P. Schwab, "Normal persistent currents", Advances in Physics **44**, 387–404 (1995).

[110] D. Loss and P. M. Goldbart, "Persistent currents from Berry's phase in mesoscopic systems", Phys. Rev. B **45**, 13544–13561 (1992).

[111] J. J. Benedetto and G. Zimmermann, "Sampling multipliers and the Poisson Summation Formula", Journal of Fourier Analysis and Applications **3**, 505–523 (1997).

[112] A. Meurer, C. P. Smith, M. Paprocki, O. Čertík, S. B. Kirpichev, M. Rocklin, A. Kumar, S. Ivanov, J. K. Moore, S. Singh, T. Rathnayake, S. Vig, B. E. Granger, R. P. Muller, F. Bonazzi, H. Gupta, S. Vats, F. Johansson, F. Pedregosa, M. J. Curry, A. R. Terrel, v. Roučka, A. Saboo, I. Fernando, S. Kulal, R. Cimrman, and A. Scopatz, "SymPy: symbolic computing in Python", PeerJ Computer Science **3**, e103 (2017).

[113] E. W. Weisstein, *Dirichlet Eta Function*, From MathWorld–A Wolfram Resource.

[114] I. M. Lifshitz and A. M. Kosevich, "Theory of Magnetic Susceptibility in Metals at Low Temperature", Soviet Physics JETP **2**, 636 (1956).

[115] C. Küppersbusch and L. Fritz, "Modifications of the Lifshitz-Kosevich formula in two-dimensional Dirac systems", Phys. Rev. B **96**, 205410 (2017).

[116] F. Escudero, J. S. Ardenghi, and P. Jasen, "A general formulation for the magnetic oscillations in two dimensional systems", The European Physical Journal B **93**, 93 (2020).

[117] T. Can, Y. H. Chiu, M. Laskin, and P. Wiegmann, "Emergent Conformal Symmetry and Geometric Transport Properties of Quantum Hall States on Singular Surfaces", Phys. Rev. Lett. **117**, 266803 (2016).

[118] B. D. B. Figueiredo, "Ince's limits for confluent and double-confluent Heun equations", Journal of Mathematical Physics **46**, 113503 (2005).

Acknowledgments

Foremost, I want to thank Prof. Dr. K. Richter for offering me a position in his research group. He supported me in any possible way, scientifically and also personally, even when times were no that easy. He further allowed me to have a research stay abroad.

In this regard, I especially also want to thank Prof. Dr. P. Wiegmann for the invitation to his research group at University of Chicago. I really enjoyed our discussions about physics and the political, cultural and social development of post-Soviet states.

Further, I want to thank apl. Prof. Dr. J.-D. Urbina, PD Dr. D. Kochan, PD Dr. C. Gorini and Dr. A. Knothe-Schulz for extensive and intensive discussions of physical and mathematical problems and giving me valuable ideas, especially at the very beginning of my work.

I want to thank Dr. A. Costa, Dr. W. Hogger and A. Riedel for proofreading.

Special thanks also go to my office mates Dr. M. Barth, A. Riedel, I. Dusa and A. Bittner who made the time very funny.

Finally, I want to thank my family and friends who supported me my whole life and in particular during my PhD candidate time.

I acknowledge funding from Sonderforschungsbereich 1277.